EXTENDING THE FEASIBILITY BOUNDARY OF THE ISOCHRONOUS CYCLOTRON

By

Jeffrey R. Schubert

A DISSERTATION

submitted to
Michigan State University
in partial fulfillment of the requirements
for the Degree of

DOCTOR OF PHILOSOPHY

Department of Physics and Astronomy

1997

ABSTRACT

EXTENDING THE FEASIBILITY BOUNDARY OF THE ISOCHRONOUS CYCLOTRON

By

Jeffrey R. Schubert

A number of recent design innovations have made the isochronous cyclotron a design option for applications that were previously considered best served by other types of accelerators. Several such proposed and existing applications of cyclotron technology are described. To provide a basis for these reviews the general characteristics of the isochronous cyclotron are summarized, including investigations of improved methods of computer simulations of cyclotron features. The possibility of reducing cyclotron size and cost by raising the maximum magnetic field from 5 to 8 tesla has been studied; the magnetic and electric fields for such an ultra compact cyclotron have been simulated and beam quality satisfactory for applications in nuclear physics is indicated. The feasibility of a cyclotron based accelerator mass spectrometry (AMS) program at the National Superconducting Cyclotron Laboratory (NSCL) has also been studied; a feasibility example of an inexpensive high resolution AMS cyclotron is developed based on the use of an existing magnet and scaling from the handful of existing designs. A review of the central region of the first commercial 235 MeV proton cyclotron for cancer therapy is presented; orbit studies are summarized and an improved central region is discussed.

To my parents, who kept telling me to get an education.

ACKNOWLEDGEMENTS

More people have contributed to this work than can be named in this short space. First and foremost, however, I must thank my advisor, Dr. Henry Blosser, for his advice and guidance; for reading and offering suggestions on a large number of drafts of this document in a short period of time; and for teaching me, possibly more than he realized, about the social and political aspects of working in science. I also want to thank the NSCL computer group for always finding a way to run the correct type of cable into my office so that all of the graphs presented in this document could not only be created but also printed. I thank Drs. Aaron Galonsky, Richard York, Gerald Pollack, Julius Kovacs, Al Zeller, and Felix Marti for serving on my guidance committee. I especially owe thanks to Dr. Marti, Dr. Morton Gordon, Dave Johnson, and Dr. Steve Snyder for writing most of the computer codes used in this work, and then helping me to understand them. I must thank nearly everyone associated with cyclotron-mass-spectrometry for helping me to track down their publications and for personally explaining a few concepts. And I want to thank the keepers of the Harper Hospital and the IBA/MGH medical cyclotrons for giving me the opportunity to study their machines. Guenter Stork provided invaluable assistance with the mechanical design for the Harper experiment, and I must also thank all of the safety personnel, especially Dr. Reg Ronningen, who were greatly inconvenienced as a result of that experiment.

Most importantly, I want to thank Freya for making it all worthwhile.

Contents

List of Tables

List of Figures

Chapter 1

INTRODUCTION

The National Superconducting Cyclotron Laboratory (NSCL) has, from its founding, maintained a program of research and development on improved cyclotrons. At present, the accelerator group has the dual mission of building and maintaining a heavy ion beam facility to support a world class nuclear physics program and studying the underlying physics of cyclotron operation. The group also devotes considerable effort to study of designs of possible future accelerators for use within the lab or elsewhere. In addition to building the K500 and K1200 [1] cyclotrons which are currently in use at the NSCL, this laboratory has designed and built a K100 cyclotron for neutron beam cancer therapy at Harper Hospital in Detroit [2]. Copies of the K500 and of the NSCL's original K50 cyclotron are in operation at Texas A&M University [3] and at Princeton University respectively, and the accelerator group has collaborated on the designs of cyclotrons for many laboratories around the world.

The three primary goals of the NSCL cyclotron research program are 1) to extend the working regime of cyclotrons, both to extend the capabilities of existing cyclotrons and to introduce the cyclotron as an option that may be cheaper or more suitable than other types of accelerators in a new beam application; 2) to improve cyclotron beam characteristics (energy spread, intensity, emittance, etc.) which are important

to users; and 3) to improve the cost effectiveness of the cyclotron in either construction or operation. Significant improvement in any of these areas constitutes a useful and important technological advance.

This thesis describes work on four cyclotron concepts. The first subject investigated concerns a basic underpinning of a large part of the NSCL cyclotron development program, namely how the initial conditions for orbit calculations are determined. Thereafter, three novel cyclotron designs are investigated. One design is of a research cyclotron that operates at a higher magnetic field than any previous cyclotron, with considerable economic advantages. Another involves adapting a low-energy cyclotron concept into a mass spectrometer for carbon-14 abundance measurements, which is expected to reduce costs relative to traditional tandem Van de Graff based accelerator mass spectrometry (AMS) facilities. Finally, design features and possible improvements in the commercial CYCLONE 235 cyclotron [4] for proton cancer therapy are reviewed; this cyclotron, which is now installed at Massachusetts General Hospital, employs a number of significant design innovations to reduce cost and simplify operations.

Chapter Overview

Chapter 2 reviews the basic concepts underlying isochronous cyclotron design. Characteristics of magnetic and electric focusing are described. The effects of imperfect timing, or 'phase' of each particle are described as are methods of using phase shifts to improve overall cyclotron performance.

Chapter 3 discusses recent work on the question of how best to choose initial conditions for orbit computations which will lead to results consistent with experimental beam observations (in the case of an internal ion source). The technique introduces a

new method of modeling the electric field near the plasma boundary of the ion source. Using the new modeling technique, the relationships between strongly coupled starting parameters such as time, energy, and the geometry of the plasma boundary are investigated.

Chapter 4 describes a conceptual design study of an 8 tesla superconducting cyclotron. The implications of using an ultra-high magnetic field are discussed. Detailed calculations of the magnetic and electric fields are presented, as are a series of orbit tracking studies in the case of an internal source and internal target. The feasibility of injecting a beam from an external source and of extracting the beam for external experiments is also investigated.

Chapter 5 presents a feasibility study for a high resolution minicyclotron for accelerator mass spectrometry. Unique goals and features of an AMS cyclotron are outlined, and the handful of existing AMS cyclotrons are described. The possibility of adapting known designs to work in the available magnet is explored.

Chapter 6 presents results of a design study of the central region of the CYCLONE 235 cyclotron for proton beam cancer therapy. As of this writing (December 1997), the cyclotron has been installed and is being tested at Massachusetts General Hospital. This design study was conducted during the commissioning of the cyclotron as a collaboration between the NSCL and Ion Beam Applications S.A., the cyclotron's manufacturer.

Chapter 2

THE ISOCHRONOUS CYCLOTRON

The purpose of this chapter is to describe the basic concepts behind the isochronous cyclotron to those readers who may be unfamiliar with accelerator physics in general or cyclotrons in particular. The descriptions in this chapter are primarily phenomenological in nature and equations are presented without derivation. More quantitative treatment of these topics is presented where appropriate in later chapters.

2.1 Origin of the Isochronous Cyclotron

The first circular particle accelerator was the 4 inch cyclotron conceived and built by Ernest O. Lawrence in 1929 [5]. The circular accelerator was a technological breakthrough since it was the first accelerator that was able to use a single pair of electrodes to provide multiple accelerating impulses to an ion beam. In this way charged particles could be accelerated to high energies with neither the use of high voltages nor the use of long strings of electrodes, as in a linear accelerator.

The compact circular accelerator's operation depends on the principle of 'cyclotron resonance.' An ion with charge q and mass m moving perpendicular to a magnetic field B will follow a circular path with a frequency f and angular frequency ω given

by the 'cyclotron equation,'

$$\omega = 2\pi f = qB/m, \tag{2.1}$$

where ω is known as the 'cyclotron frequency.'

Although the radius of the orbit grows with increasing energy, if q, B and m are constant, then the frequency is constant for all energies, velocities and radii. If one arranges two electrodes ('dees') around an ion source, as in Figure 2.1 and excite the electrodes with a voltage oscillating at the cyclotron frequency, then the ions may gain energy twice on every turn, returning to the same azimuth for another kick at the same time in each cycle. An accelerator in which the orbital frequency is constant is said to be 'isochronous.'

Positive ions are pulled from the ion source whenever the voltage on the first dee is negative. The beam then increases the radius of its orbit with each accelerating kick, so its path approximates a spiral. When the beam nears the edge of the magnet pole it is extracted by the use of an electrostatic deflector. If the beam is positive the outer electrode would have a negative charge in order to pull the beam out of its orbit while the thin grounded inner electrode, known as the septum, separates the exiting beam from the inner orbits.

A cyclotron with a radially constant magnetic field is only isochronous in the nonrelativistic approximation. Ions at relativistic velocities experience a mass increase $m = \gamma m_o$, where m_o is the particle's rest mass and γ is the Lorentz factor. The ion's angular frequency is then given by

$$\omega = qB/m = qB/\gamma m_o \tag{2.2}$$

which falls (for constant B) as the energy increases, whereas the RF frequency in a traditional continuous wave (CW) cyclotron remains constant. The ions then arrive at each gap later in the RF cycle than at the previous gap. If one tried to build a

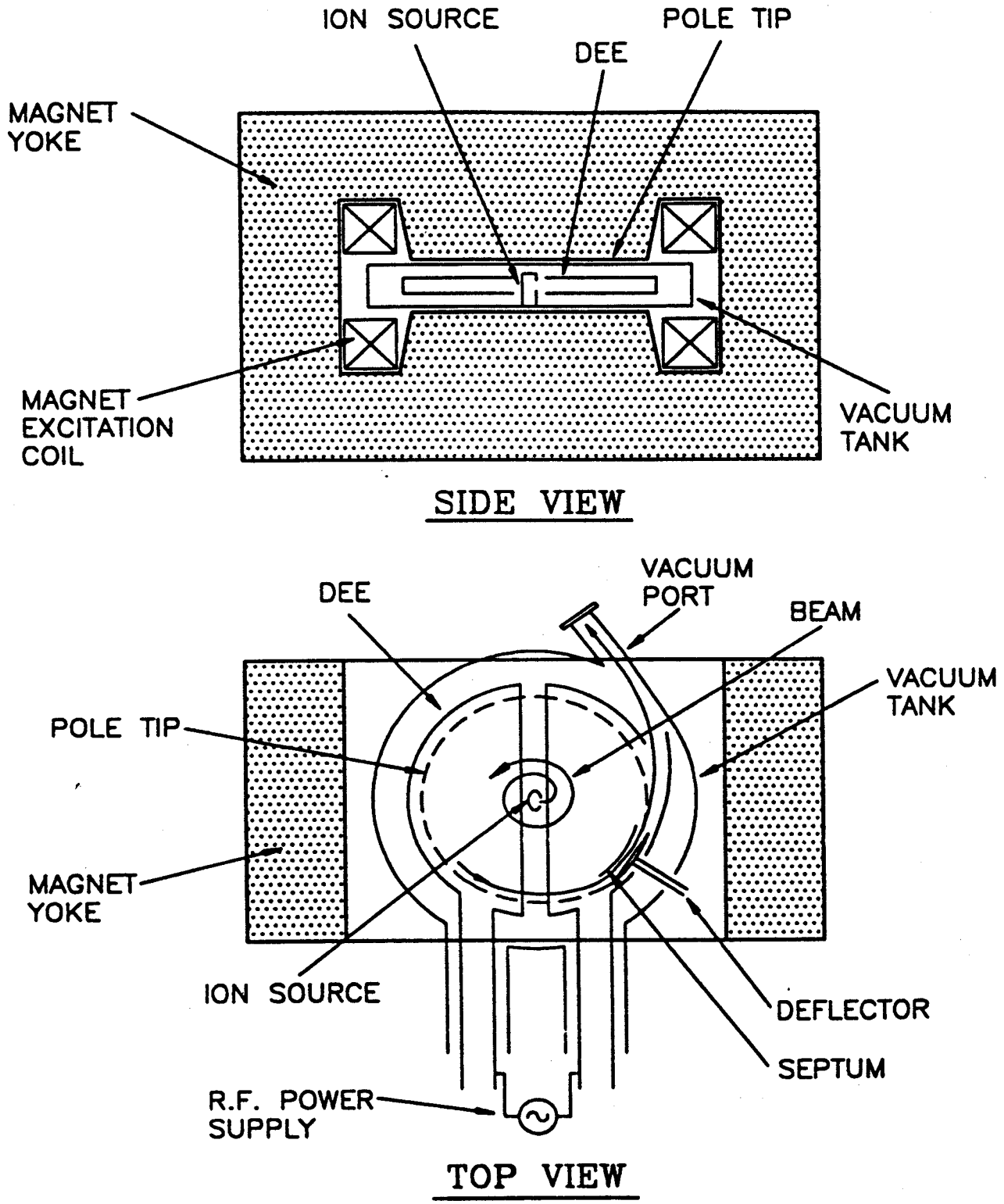

Figure 2.1: Schematic of a classical cyclotron. (From G.H. Mackenzie, P.W. Schmor and H.R. Schneider (1992) in: G.L.Trigg (Ed.), "Encyclopedia of Applied Physics", Vol.4, Weinheim, New York: VCH Publishers.)

constant-B high energy cyclotron this would continue until the beam is so late that it comes to an accelerating gap after the voltage has reversed and the beam is thereafter decelerated.

The cyclotrons of the 1930's (the 'classical' cyclotrons) were actually built with magnetic fields that fall as a function of radius in order to provide axial focusing (see section 2.4) which exacerbated the problem of non-isochronism. In 1937 Bethe and Rose predicted that the conflict between axial focusing requirements and the relativistic mass increase meant that no cyclotron proton beam could ever reach an energy greater than 12 MeV [6].

The next year theorist L.H. Thomas published the first proposal for 'sector focusing,' whereby the axial magnetic field strength varied with azimuth [7]. The motion of charged particles interacted with the azimuthally varying field to provide a force that was always pointed toward the median plane. Although it was more than a decade before experimentalists learned to shim their poletips to create this focusing field, once they began, they discovered a collection of magnetic focusing techniques described in section 2.4.

Now that the radially falling magnetic field was no longer needed, it was possible to build cyclotron magnets whose azimuthal average magnetic field $\langle B \rangle$ (this is the field averaged along a closed coasting orbit for a given ion energy) increases in proportion to the relativistic mass increase of ion beam. The function $\frac{\langle B \rangle}{\gamma m_o}$ then remains constant for all radii within the machine so the cyclotron frequency is constant for the entire acceleration process. Machines of this sort proliferated after the completion of the 50 MeV proton cyclotron at UCLA in 1960. They are variously known as 'sector-focused,' 'isochronous,' 'spiral-ridge,' 'azimuthally-varying-field' (AVF), 'fixed-field alternating-gradient' (FFAG) or 'Thomas' cyclotrons [8].

2.2 The Modern Cyclotron

Schematics of two typical modern cyclotron designs are shown in Figures 4.1 and 6.1

Once the cyclotron magnet had regions of wide and narrow magnet gaps (known as valleys and hills) designers gained the mechanical option of moving the live dees into the valley gaps, while using the grounded magnet hills themselves as the dummy dees. This saves valuable space within the magnet, and causes the dees to take on the wedge shape of the space available in the valley. A three sector cyclotron (three hills and three valleys) in this configuration can have three live 60° dees, three dummy dees, and six accelerating gaps in place of the classical cyclotron's one or two live dees and two gaps.

Builders of high energy cyclotrons found it necessary to bend the wedge shaped hills into spiral wedges to enhance vertical focusing (section 2.4). The UCLA cyclotron and many of it's successors form their dees to fit into the spiral shaped magnet valleys. The three latest cyclotrons built at the NSCL use this configuration. Studies at the NSCL [9] have determined that spiral shaped accelerating gaps have little deleterious effect on beam quality.

In addition to the topological differences in the dees and poletips, several other subsystems have grown in complexity since the earliest cyclotrons. The room temperature magnet is often replaced by a helium cooled superconducting magnet to maximize the magnetic field strength, and the central region has gained many features. In a classical cyclotron the central region is nothing more than the ion source, and in some cases a pair of posts between the top and bottom of the first dee to help guide and focus the beam as it is extracted from the ion source. This set of posts, called the 'puller' is elongated into a tunnel to control the timing of the beam in more complicated cyclotrons [10]. The central regions for the high field cyclotrons at the

NSCL have one or two posts at the inner radius of each of the six dees and dummy dees, similar to the design in Figure 4.8. The innermost posts serve to electrically isolate the three dees from one another, a task which grows more important and more difficult as designers use higher magnetic fields which shrink the radius of the first beam orbit. The sets of slits formed by the inner and outer posts help to shape the electric field to guide the beam into a centered orbit. In high energy, high field cyclotrons the design of the central region has gained in importance. It's importance is now comparable to that of the design of the magnetic focusing system.

2.3 Cyclotron Parameters

Cyclotrons are usually characterized by the maximum bending limit of their magnet, denoted K_b. In the non-relativistic approximation this is the maximum energy in MeV of a proton beam that could be bent into a closed orbit within the magnet. For beams of any other ion, with charge Q elementary charges and mass A amu, the maximum closed orbit energy is given by

$$E/A = K_b(Q/A)^2. \tag{2.3}$$

The bending limit itself is defined by $K_b = \frac{1}{2}\frac{(eB\langle r\rangle)^2}{m_o}$ where e,m_o,B, and $\langle r\rangle$ are one elementary charge, one atomic mass unit, the magnetic field, and the average radius of the largest orbit. The bending strength of a magnet is sometimes also given as the magnet's maximum 'rigidity,' which is the quantity $B\rho$ where ρ is the instantaneous radius of curvature of the beam at maximum energy. (Although ρ changes as the beam moves from hills to valleys, in the cyclotrons described in this thesis ρ is approximately equal to $\langle r\rangle$ and the two are often exchanged in first order calculations of general cyclotron parameters. The difference between ρ and $\langle r\rangle$ is not always negligible and is fully accounted for by the computer simulations used in later

chapters.)

The K100 Harper cyclotron, then, accelerates deuterons ($Q/A = 1/2$) to an energy of 25 MeV/nucleon and a final radius of roughly 0.31 m in an average field of 4.6 T. It's nominal rigidity is 1.44 Tm.

The accelerating system of a cyclotron is categorized by its 'harmonic number' h. A cyclotron operates in 'first harmonic mode,' $h = 1$, if the RF voltage makes one cycle in the same time period that a particle makes one revolution. In principle the RF frequency f_{RF} may be any multiple of the orbital frequency f_o, so $h = \frac{f_{RF}}{f_o}$. The 8 Tesla Cyclotron described in Chapter 4 will employ three dees and three dummy dees and will operate in third harmonic mode. Fourth harmonic mode cyclotrons may be built with either four dees (to make maximum use of the accelerating voltage) or with two dees, leaving space free for other mechanical structures. The C235 described in Chapter 6 is an example of the latter configuration.

2.4 Phase

The 'phase' of the beam ϕ is a measure of its promptness relative to the RF wave. In order to obtain the maximum possible energy gain from the alternating dee voltage, a given particle must pass each dee center as the voltage wave passes through $V = 0$. Choosing $V(t) = V_o \sin \omega_{rf} \tau$ as the voltage convention, this occurs when the RF time τ is either 0° or 180°. Such a particle is said to be 'on time' relative to the RF wave, and its phase is defined as $\phi = 0°$ measured in RF degrees (where $1° = h°RF$). In an idealized system with dees that are $180°RF$ wide (corresponding to 60° dees if $h = 3$ or 45° dees if $h = 4$) the $\phi = 0°$ particle passes through each gap when the dee voltage is at its peak.

An 'early' or 'late' particle passes through the dee center before or after the voltage

wave passes through $V = 0$. The phase is then defined according to

$$\phi = \tau - h\theta_{particle}$$

where $\theta_{particle}$ is the angular location of the particle at a given τ. An early particle has a negative phase (measured in RF degrees) and a late particle has a positive phase.

2.5 Axial Magnetic Focusing

2.5.1 Axial Field Index Focusing

The earliest form of magnetic focusing employed in cyclotrons is illustrated in Figure 2.2. Three particle orbits are drawn: one each on, above, and below the median plane. In a region of space free of currents and time varying electric fields, Maxwell's equations tell us that $\nabla \times \mathbf{B} = 0$. The azimuthal component of $\nabla \times \mathbf{B}$ must therefore be zero, giving

$$\frac{\partial B_r}{\partial z} - \frac{\partial B_z}{\partial r} = 0.$$

This means that if the axial magnetic field decreases with increasing radius, $\frac{\partial B_z}{\partial r} < 0$, then the magnetic field lines must bend so that they are concave toward the center of the cyclotron to satisfy $\frac{\partial B_r}{\partial z} < 0$. The radial component of the magnetic field will then interact with the azimuthal component of the ion's velocity to give rise to an axial component of the Lorentz force, $\mathbf{F} = q\mathbf{v} \times \mathbf{B}$. So long as the magnetic field is falling with increasing radius, this force will be pointed toward the median plane.

The axial force vanishes at the median plane and increases in magnitude as the particle moves further away from the median plane. To a first order approximation the particle may be treated as if it is in a simple-harmonic-oscillator potential. An ion that starts with a displacement in axial position or velocity will oscillate about

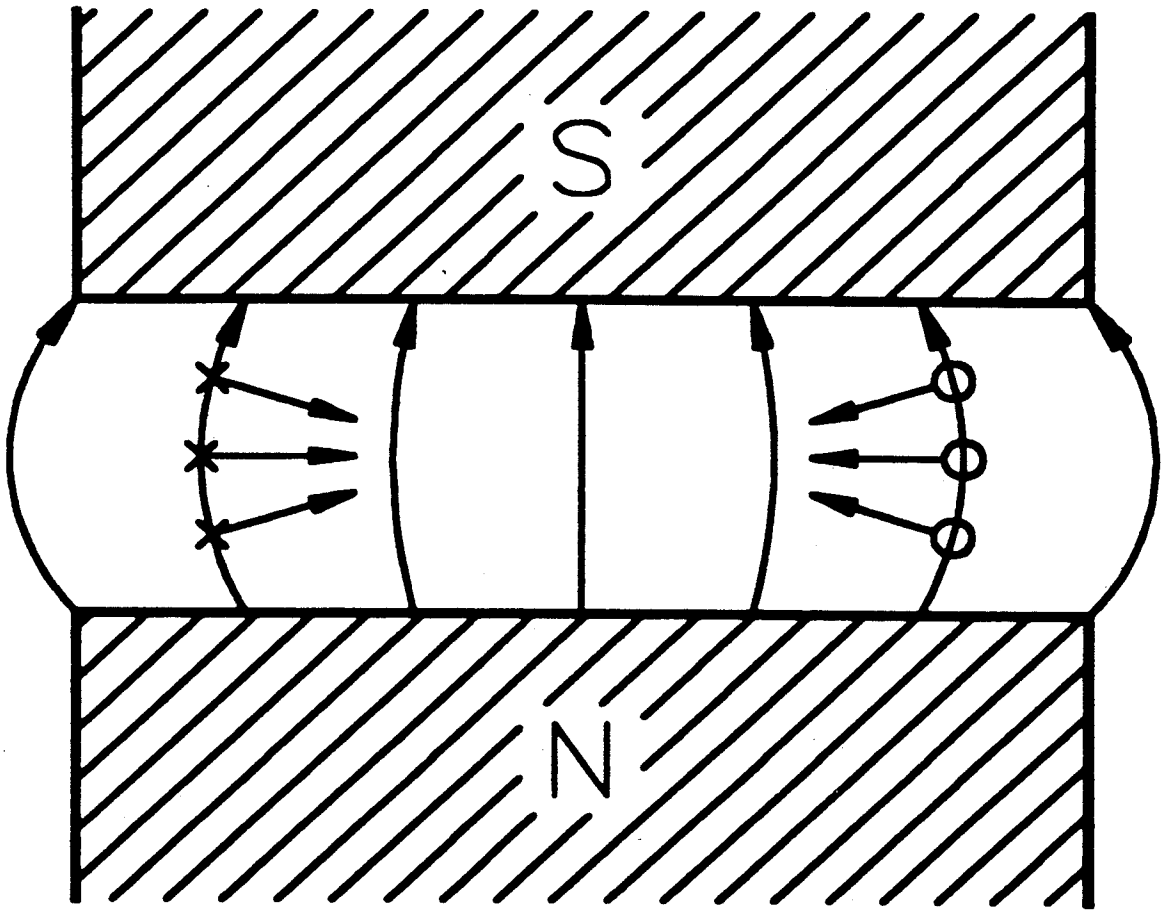

Figure 2.2: Side view of a classical cyclotron illustrating the vertical focusing effect of a radially decreasing magnetic field. A beam of positive charge is directed into the page on the left side and out of the page on the right. Lines of magnetic induction point from the north to the south pole of the magnet. The total Lorentz force on each ion is shown. The force has a component directed toward the median plane which provides axial focusing of the beam. (From G.H. Mackenzie, P.W. Schmor and H.R. Schneider (1992) in: G.L.Trigg (Ed.), "Encyclopedia of Applied Physics", Vol.4, Weinheim, New York: VCH Publishers.)

the median plane with a characteristic frequency

$$\omega_z = \sqrt{-\omega_{ion}^2 k}.$$

where ω_{ion} is the ion's rotation frequency defined in equation 2.2 and k is a function known as the 'field index' which characterizes the radial profile of the midplane magnetic field. The field index is defined as

$$k = \frac{r}{B_z}\frac{dB_z}{dr}. \tag{2.4}$$

The frequency of oscillation is typically expressed in terms of the ion's orbital frequency,

$$\nu_z = \omega_z/\omega_{ion} = \sqrt{-k} \tag{2.5}$$

where ν_z is the number of axial oscillations per 360° orbit [11]. ν_z is usually referred to as the 'axial (or vertical) focusing frequency,' but it is also known as the 'vertical betatron frequency' or 'vertical tune.'

2.5.2 Thomas Focusing

As in the previous section, Thomas focusing uses the interaction of an ion's velocity with magnetic fringe fields to provide axial focusing. In Figure 2.3a we see that introducing hills and valleys to the cyclotron's poletips distorts the classical circular orbit into a 'scalloped' shape. This is because the radius of curvature of the ion path is greater in the high field hill regions than in the low field valley regions. Each ion's tangential velocity may then be broken into an azimuthal component and a radial component. In Figure 2.3b we see that the radial component of the ion's velocity interacts with the azimuthal component of the hills' fringe fields to produce a force that is always pointed towards the median plane. In a three sector machine, with six hill-valley and valley-hill transitions, the beam will experience six axial focusing kicks during each orbit.

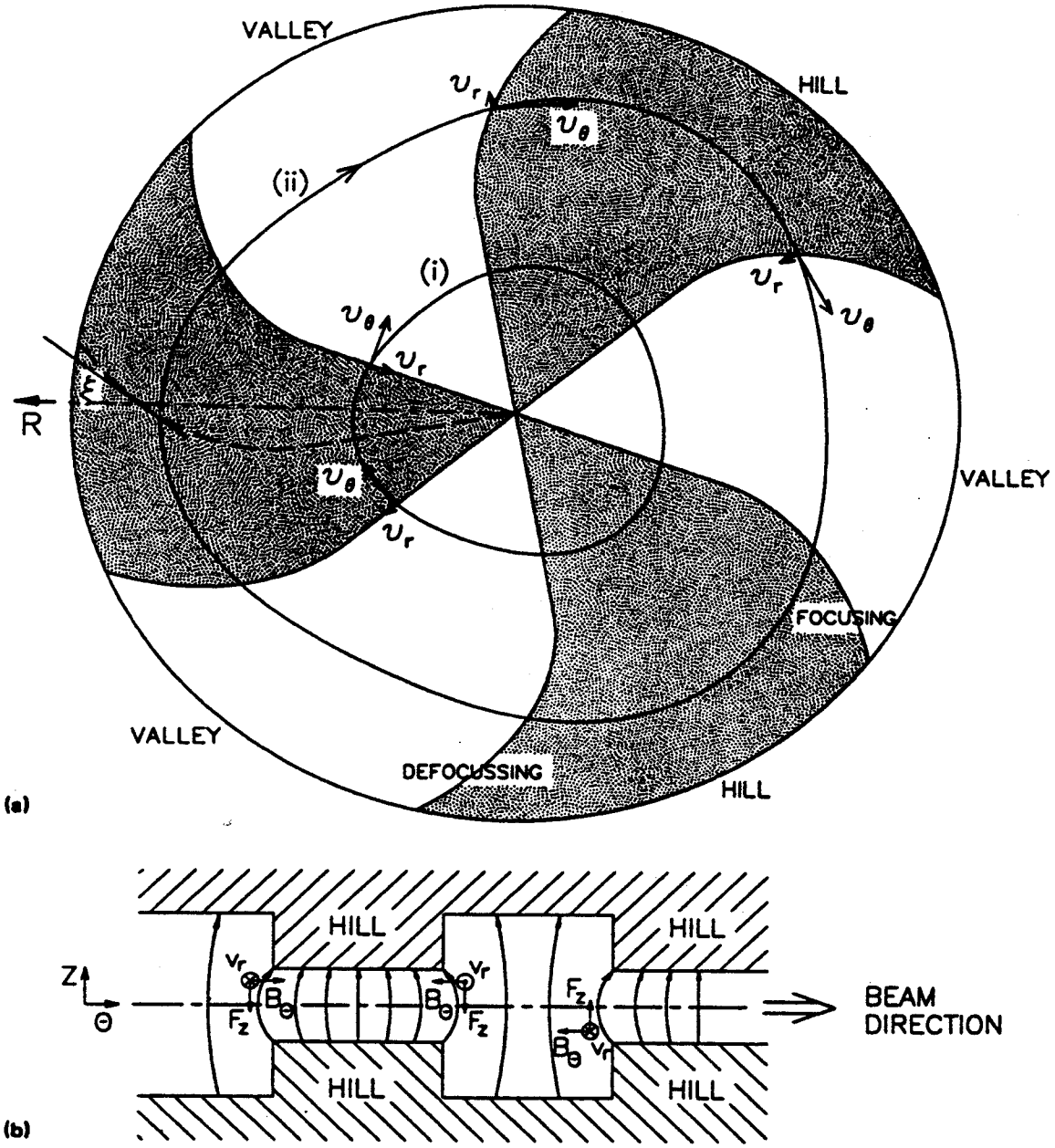

Figure 2.3: (a) Top view of a sector-focused cyclotron showing two equilibrium orbits. The scalloping of the orbits is caused by the difference in orbit curvature in the hill fields and valley fields. Both orbits (i) and (ii) experience Thomas focusing from the sectors; the outer orbit (ii) experiences additional focusing because the sectors have spiral edges. (b) Side view of the same cyclotron that has been 'unrolled' so that we may see more than one sector at a time. The observer is looking outward from the center. Axial forces are drawn for orbit (i) at each hill-valley and valley-hill transition. (From G.H. Mackenzie, P.W. Schmor and H.R. Schneider (1992) in: G.L.Trigg (Ed.), "Encyclopedia of Applied Physics", Vol.4, Weinheim, New York: VCH Publishers.)

The strength of Thomas focusing depends on the magnitude of the change in field strength between the hills and valleys. This change is known as 'flutter.' Many different definitions exist for flutter. Here we use the formalism of Livingood, which is defined for a field with a purely sinusoidal azimuthal variation in B_z [12]. If $\langle B \rangle$ is the azimuthal average magnetic field and $\langle B^2 \rangle$ is the mean squared field, then the 'flutter function' F is defined by

$$F \equiv \frac{\langle B^2 \rangle - \langle B \rangle^2}{\langle B \rangle^2}. \tag{2.6}$$

Expressed in terms of the maximum hill field B_h and the minimum valley field B_v equation 2.6 becomes

$$F = \frac{(B_h - B_v)^2}{8\langle B \rangle^2}. \tag{2.7}$$

Since the actual field shape is never a sinusoid in practice we consider the focusing forces that arise from the fourier components of the total field. In a three sector machine, the third harmonic component B_3 of the total field dominates Thomas focusing. B_3 then approximates the amplitude of the sinusoidal variation, and it replaces the quantity $(B_h - B_v)/2$ in equation 2.7 so that the flutter function is approximately

$$F \approx \frac{1}{2}\left(\frac{B_3}{\langle B \rangle}\right)^2$$

for a three sector machine.

Flutter focusing is also weakly dependent on the number of sectors N_{sect} in the magnet. The leading terms of the total axial betatron frequency in a radial sector cyclotron are given by [12]

$$\nu_z^2 \doteq -k + \frac{N_{sect}^2}{N_{sect}^2 - 1} F + \cdots. \tag{2.8}$$

In order to maintain radial stability, the minimum number of sectors allowed in a sector focused cyclotron is three, [12] so the factor of equation 2.8 that depends on N_{sect} is always close to unity.

2.5.3 Spiral Ridge Focusing

If the hills of a Thomas cyclotron are bent so that their edges form a spiral (Figure 2.3a), then the fringe field at each hill-valley transition will have a radial component B_r at locations off of the midplane. This radial magnetic field will interact with the azimuthal velocity of an orbiting particle to create an axial force which is analogous to the edge focusing force described in Section 2.5.1. The force is focuses the beam at the convex edge of each hill and defocuses the beam at the concave edge. The focusing force on a given ion is proportional to the distance of the ion from the median plane. Therefore, as in an array of equally strong optical focusing and defocusing lenses (known as a 'F0D0 channel' in classical optics), the ion is always further from the optic axis in a focusing lens then in a defocusing lens and the focusing always overcompensates the defocusing. Thus, the net effect is one of positive focusing [13]. This axial focusing force is known as the 'Kerst force.' The net focusing effect is strengthened by the fact that the orbit has a longer pathlength in the focusing field than in the defocusing field (because the scalloped orbit is more nearly perpendicular to the defocusing edge of the hill than to the focusing edge.) This component of axial focusing is known as the 'Laslett force' [12]. The strength of Kerst-Laslett focusing depends on the pitch of the spiral ξ, which is defined in Figure 2.3a. The first few terms of the axial betatron frequency for a spiral-sector cyclotron are

$$\nu_z^2 = -k + \frac{N_{sect}^2}{N_{sect}^2 - 1} F(1 + 2\tan^2\xi) + \cdots. \tag{2.9}$$

For a perfectly isochronous machine $k = \gamma^2 - 1$ where γ is the Lorentz factor [12]. If we insert this expression for k into equation 2.9 we see that the total axial focusing force in an isochronous cyclotron has a defocusing component (the $-\gamma^2$ term) which increases with increasing energy. To compensate for this defocusing designers increase the spiral angle with radius. Low energy machines such as the 50 keV/ion

Shanghai Mini-Cyclotron for AMS described in Chapter 5 use purely radial sectors. Higher energy machines such as the 235 MeV proton cyclotron described in Chapter 6 often use radial sectors at small radii and then make a transition to spiral sectors midway through the acceleration process. (The 200 MeV proton cyclotron at Indiana University reaches the highest energy/nucleon of any cyclotron with purely radial sectors [14].) In machines with inherently low flutter such as the Eight Tesla Cyclotron (Chapter 4) the spiral begins in the central region and is an important source of axial focusing for most of the acceleration process.

The flutter of the magnetic field vanishes near the center, and therefore both Thomas and Kerst-Laslett focusing vanish as well. (In this region the distance between the hills is small compared to the vertical hill gap, so at the median plane the field is not dominated by the nearest hill or valley and the nth harmonic component of the magnetic field B_n rises as $(\frac{r}{g})^n$ where g is the hill gap [15].) Many cyclotrons then employ a 'field cone' to focus the first few turns. This is a region of high magnetic field at the center of the machine that falls to the isochronous field value after a few turns. While the field is falling the beam is axially focused by the negative field index (the negative radial field gradient) as described in section 2.5.1. (The phase shift caused by the region of non-isochronous field is tolerated so long as the number of turns in this region is small.) Often a hole is drilled in the iron yoke to insert the ion source (or to inject a beam from an external source) which will cause a depression in the center of the midplane magnetic field. In this case it is difficult, or sometimes impossible, to create a field cone with substantial gradient at radii as small as the injection (or source) radius. Often the first one to two turns will experience negligible or negative magnetic focusing and so they must rely on electrostatic focusing, as described in the following section.

2.6 Axial Electric Focusing

Electrostatic focusing results from the fringe electric fields in the accelerating gaps. We see in Figure 2.4a that during the accelerating half of the RF cycle the electric field in a gap provides the beam with a vertical focusing kick on entering the gap and a defocusing kick on leaving. Both forces are proportional to the distance of the particle from the median plane. Neglecting the acceleration of the beam, for $\phi = 0$ the kicks are of equal strength, so as in a series of equally strong focusing and defocusing cylindrical glass lenses, the net effect is one of positive focusing. If we account for the fact that the particle is accelerating across the gap then the focusing is enhanced by the fact that beam traverses the second half of the gap in less time than the first half, so it spends less time under the influence of the defocusing force.

The focusing force described above is relatively weak compared to other sources of axial focusing in the cyclotron. However, if the particle passes through the gap at a non-zero phase, then the strength of the electric field within the gap will be either rising (for negative phase) or falling (for positive phase) as the particle moves through the gap. If the voltage is falling as the particle traverses the gap (Figure 2.4b) then the focusing force will overpower the defocusing force to produce an additional net positive focusing effect that is proportional to the phase.

It will be shown computationally in Chapter 4 (Figures 4.7 and 4.10) that electrostatic focusing can be made stronger than magnetic sector focusing, though only for the first few turns. Electrostatic focusing looses its effectiveness in proportion to the beam's energy, and, as a rule of thumb, is said to be proportional to $1/N$ where N is the number of turns a given ion has made. Therefore, electric focusing is primarily used to contain the beam until it reaches a radius where magnetic focusing becomes sufficient.

Although a phase curve that remains near zero for the entire path of the beam would result in the most efficient acceleration, the cyclotron designer often arranges the central region so that the beam begins at a positive phase to maximize the effectiveness of electrostatic focusing for the first couple of turns. The magnetic focusing cone then dominates for a few turns while reducing the phase to a value near zero. After that, sector focusing (and possibly spiral sector focusing) takes over and dominates until the beam reaches the edge of the magnet pole.

It should be noted that if the magnetic focusing cone is too large, (in magnitude or in radius) then the beam can be forced into a negative phase such that electrostatic defocusing (Figure 2.4c) partially defeats the benefits of the cone. For this reason the task of extending cone focusing to the point where flutter focusing is available is non-trivial, and a cyclotron may have a region of low ν_z near the transition from cone focusing to flutter focusing. (Such a situation was corrected during construction of the C235. Figures 6.3 and 6.6 show the magnetic field and the magnetic contribution to the axial focusing frequency before and after the optimization of the central focusing cone. Figure 4.8 shows the effect of electrostatic focusing on ν_z for the 8 Tesla Cyclotron design. In both cases a fraction of the first turn would be axially defocused without the contribution of electrostatic focusing.)

2.7 Radial Focusing

In addition to the axial focusing phenomenon there is also a radial focusing phenomenon which arises from the interaction of a charged particle's velocity with the magnetic field. If the magnetic field rises with radius, then a particle with a positive radial displacement from its central ray orbit will acquire a greater curvature than the central ray due to its elevated local magnetic field. This particle is then pushed back

towards the central ray. Conversely, when the same particle has a negative radial displacement, it will be in a region of low magnetic field and it will again change its radius of curvature so that it moves back toward the central ray. In a radially flat field there is also an effective restoring force. In the case of a flat field cyclotron, the displaced equilibrium orbit would simply follow a circle which is displaced from the circular orbit of the 'central ray.' For a displacement small relative to the orbital radius, the displaced ray would spend roughly half of its orbit at a smaller radius and half at a larger radius (relative to the center of the machine) than the centered orbit. In this case the radial betatron frequency ν_r is unity. Even if the magnetic field decreases with radius, ions will experience radial stability if the field does not fall too quickly. To first order the radial betatron frequency is given by

$$\nu_r^2 = 1 + k + \cdots \tag{2.10}$$

so positive radial focusing exists so long as $k > -1$.

Since the radial field profile in an isochronous cyclotron is determined by the need to make the field $B_z(r(E))$ proportional to the Lorentz factor $\gamma(E)$ the cyclotron designer has little control over radial focusing. Since $k = \gamma^2 - 1$ for a perfectly isochronous cyclotron, the radial focusing frequency is approximated by

$$\nu_r \approx \gamma.$$

The radial focusing frequency mainly becomes an issue when it passes through a resonant value such as $\nu_r = 1$, $\nu_r = \frac{1}{2}$, (or reaches a 'stopband' at $\nu_r = \frac{N_{sect}}{2}$,) or when $\nu_r + \nu_z$ come into a coupled relationship such as $\nu_r = 2\nu_z$. In the $\nu_r = 1$ case a small azimuthal imperfection in the field could push the orbits off center, which will have detrimental effects on beam quality. The $\nu_r = 1$ resonance occurs when $\frac{dB_z}{dr} = 0$. In the 8 Tesla and C235 cyclotrons there is a $\nu_r = 1$ resonance at the radius where

the edge of the focusing cone meets the isochronous field and near the edge of the magnet where B_z reaches its peak value. Often a set of 'trim-coils' are incorporated into a cyclotron magnet design to fine-tune the magnetic field in the neighborhood of the $\nu_r = 1$ resonances. At this point an intentional imperfection may be used to control the centering of the orbits when they pass through the $\nu_r = 1$ resonance near the center. When the beam passes through $\nu_r = 2\nu_z$ (the 'Walkinshaw Resonance' which occurs near the edge of the magnetic field) the energy associated with radial oscillations is transferred into the particles' axial oscillations, expanding the axial size of the beam. In all cases the designer attempts to adjust the field profile so that the beam passes through the resonances quickly and their detrimental effects are minimized. In the case of a coupling resonance such as $\nu_r = 2\nu_z$ it is also helpful to null the radial amplitude of the beam prior to the resonance. This is done by carefully centering the beam until it exhibits no coherent radial oscillations.

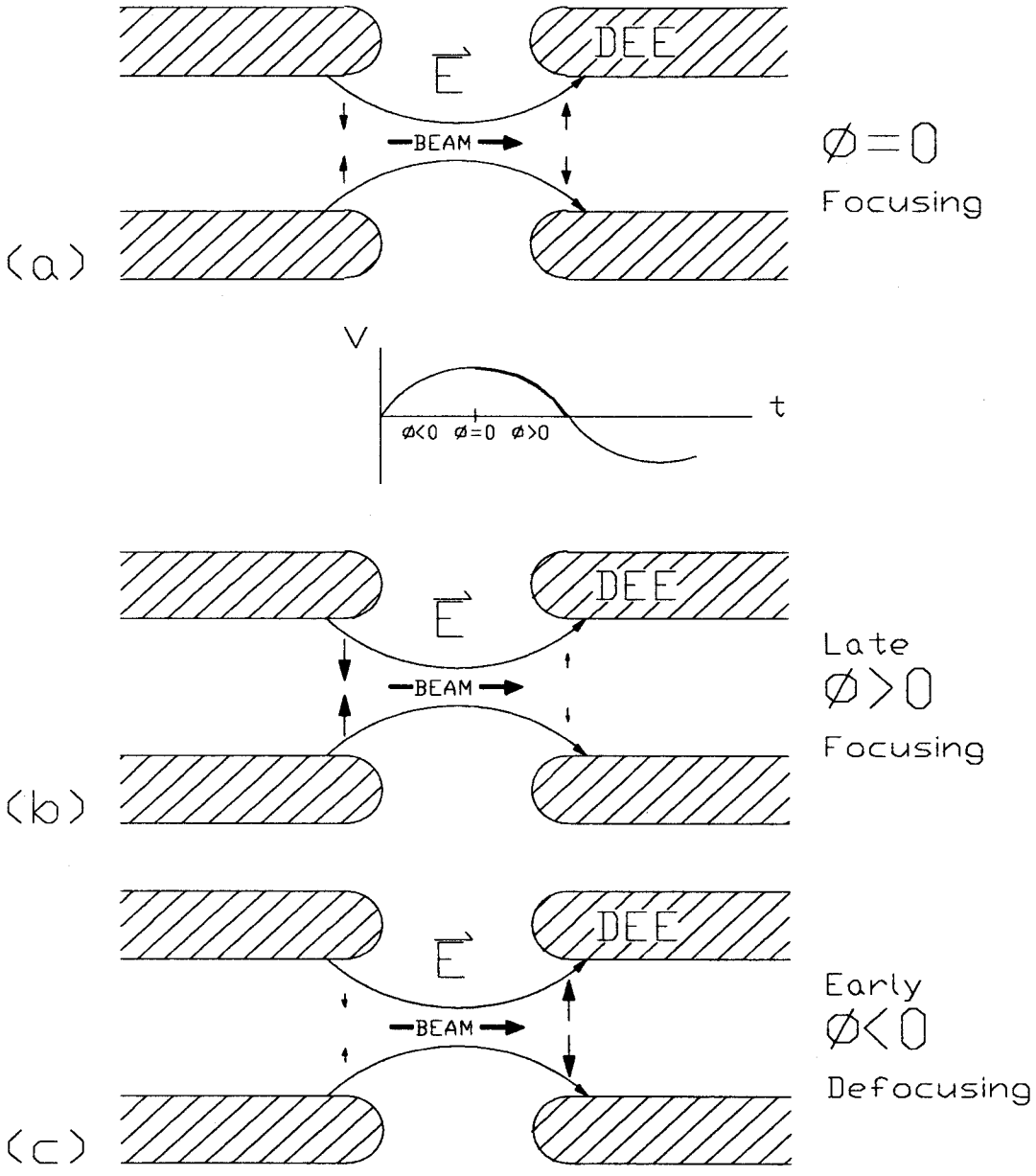

Figure 2.4: Electrostatic field lines and their vertical components in the acceleration gap, which give rise to electrostatic focusing.

Chapter 3

INITIAL CONDITIONS FOR ACCURATE ORBIT TRACKING

3.1 The Problem of Choosing Initial Conditions in the Case of an Internal Ion Source

In any classical orbit problem the choice of initial conditions fully determines the final result. Unfortunately, the cyclotron designer cannot electively fix the exact starting time τ_0 with respect to the RF voltage wave or the exact starting energy E_0 of the ions that will make up the densest part of the beam, or the starting position (except within the limit set by the source aperture) or the starting direction. For computational models the designer must choose parameters for the nominal central ray by guessing at values for (τ_0,E_0,position,direction) that are likely to dominate the beam. With orbit tracking codes such as the NSCL's Z3CYCLONE [16] it is a trivial matter to test a variety of initial phases and energies with a given central region design. The designer then compensates for his imperfect knowledge of the most abundant starting phase or energy by ensuring that the central region will function for a realistic range of possibilities.

If an internal ion source is used, even more uncertainty is involved. The volume inside the chimney of a PIG ion source is filled with a neutral plasma, from which

positive ions are pulled out by the puller. The surface of the plasma is an ill-defined region of near-zero potential. In this study we define the equipotential surface of exactly zero potential (the system ground) as the 'plasma-boundary.' Ions inside the boundary are assumed to be shielded by the plasma charge from the electric field produced by the puller, while ions whose thermal motion carries them outside the plasma boundary are accelerated by the puller field. The presumed shape of the plasma boundary determines the starting position of ions in the simulation of cyclotron orbits. The plasma boundary also forms part of the boundary condition for calculation of the electric field in the region between the chimney and puller. If the plasma boundary is convex (i.e. bulging towards the puller) then the ions will start in a higher electric field than if the plasma boundary were concave (bulging towards the inside of the chimney.) This part of the field map is traversed when the ions are at their slowest and transit-time effects on energy gain are at their greatest. Thus, small variations in geometry can have an important influence on an ion's energy gain.

The study presented in this chapter is limited to motion in the median plane of the cyclotron. Ions start on a line extending from the axis of the chimney (at the median plane) through the center of the chimney aperture. The ions' initial momentum is taken as directed along this same line. Additional starting parameters, such as variations in initial radial or axial phase-space, are left for future studies. (A brief look at the effect of the plasma boundary shape on radial phase space is presented in Chapter 6.)

3.2 The Central Region of the Harper Medical Cyclotron

In this chapter we use the Harper Hospital Medical Cyclotron as our test example. This cyclotron accelerates deuterons that are produced in a Phillips Ionization Gauge

(PIG) ion source at the center of the machine [17]. The design process followed the traditional path of using computer simulations to begin the design followed by experimental modifications to the central region in parallel with further simulations in order to achieve the desired beam current. In the second stage it is not unusual for experimental work to lead the simulations. The final major modification of the Harper central region (reducing the clearance between the ion source and dee from 4 mm to 2.54 mm) resulted in beam currents five times greater than the design current [18]. Since there were many other pressing matters in the commissioning of this cyclotron, computer orbit tracking studies of the final configuration have been deferred until this study.

3.3 The Shape of the Plasma Boundary

The chimney of a PIG ion source is a grounded cylinder that contains a cylindrical electron beam and an ionized gas (Figure 3.1). The section of the plasma boundary behind the exit hole is exposed to the external electric field provided by the cyclotron's puller electrode. A negative voltage on the puller will extract positive ions from the plasma boundary. The plasma in this region is left with a net negative charge and if the puller voltage were constant the negative plasma would be forced to retreat back into the chimney, resulting in a concave plasma boundary (Figure 3.1c).

Although positive ions will be extracted for any negative puller voltage, in order for the plasma boundary to take on a concave (or flat) shape requires a certain negative voltage threshold [19, 20]. This is because there is a small net negative charge on the plasma deep within the chimney. The arc column of electrons is then subject to an outward space charge force. For a certain negative puller voltage, the space charge force should balance the force of the puller and the plasma boundary should be flat.

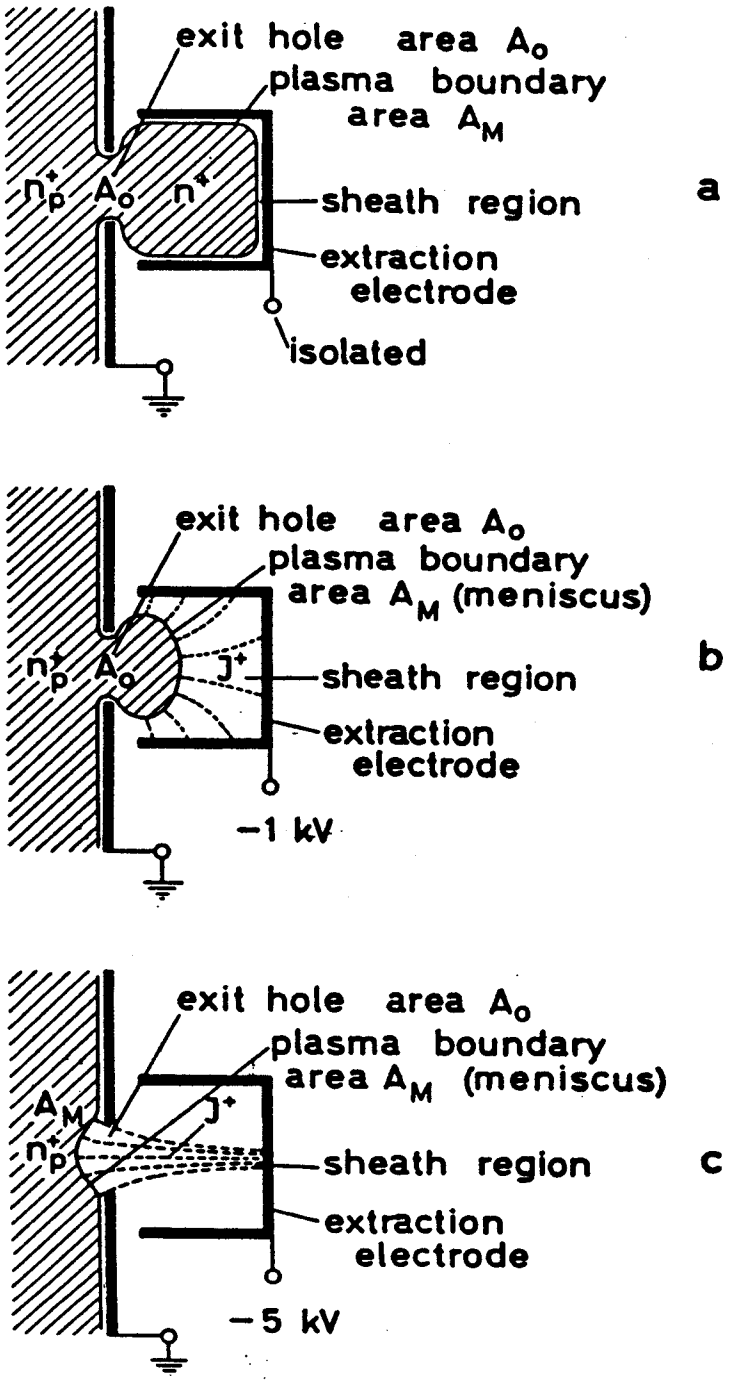

Figure 3.1: Schematic of a PIG ion source with various constant voltages on the extraction electrode. (From J. Koch (Ed.), R.H.V.M. Dawton, M.L.Smith, and W. Walcher (1958) in "Electromagnetic Isotope Separators and Applications of Electromagnetically Enriched Isotopes," Interscience Publishers Inc., New York.)

Below this negative puller voltage, positive ions will still be extracted but the plasma boundary will bulge out of the exit hole (Figure 3.1b). If the puller were neutral or positively charged, the plasma would bulge out even further (Figure 3.1a) [19, 20].

Mallory observed a concave plasma boundary in an experimental test stand with a DC puller [21, 22] and Smith saw possible evidence of a concave plasma boundary in observations of early turn focusing in the Canberra cyclotron [23, 24]. To the best of our knowledge, however, no clear experimental data exist for the case of an ion source in a cyclotron with RF voltage on the puller. The actual shape of the plasma boundary might oscillate with the puller voltage or it might be an average of the DC cases described above. The unknown shape of the plasma boundary introduces a significant uncertainty to orbit calculations.

3.4 Probable Starting Time and Energy for the Central Ray

The energy of ions from the PIG ion source, prior to acceleration by the puller, is determined by two factors. Ions gain some momentum transverse to the magnetic field from collisions with electrons in the arc discharge. The dominating component of initial energy is probably the plasma potential. Although referred to as neutral, the plasma actually has a small negative bias. Values on the order of 10V (relative to the anode) are common for the plasma potential in PIG ion sources [19]. Neither component of initial ion energy may be calculated and experimental measurements are rarely taken for internal ion sources that are built for cyclotrons. Ions will be extracted from the source for the entire 180° of RF time during which the puller has a negative voltage. The current I that is extracted and transported, however, will be

limited by the puller voltage in accordance with the Childs-Langmuir law [19]

$$I \propto V^{3/2}$$

which in our case is equivalent to

$$I \propto (V_{dee} \sin(\tau_0))^{3/2}$$

where V_{dee} is the peak voltage applied to the dee and puller.

Cyclotron designers typically develop central regions around the ray with the starting time that results in the maximum energy gain E_1 in the source-puller gap [25]. At this time $\partial E_1/\partial \tau_0 = 0$ so the widest possible range of starting times will experience a similar energy gain. Usually this means a maximum beam current will experience the same energy gain. If this ray is at too early a starting time (so not enough current is extracted even for a wide range of starting times) then a compromise must be found between including current from a wide range of starting times and using an average starting time that provides high beam current relative to other average starting times. Typical central regions at the NSCL are designed with central rays that start in the range $\tau_0 = 200°$ to $\tau_0 = 240°$ (where $\tau = 270°$ corresponds to peak negative puller voltage.)

3.5 A New Computational Model for the Plasma Boundary

The NSCL's orbit tracking program, Z3CYCLONE, uses electric-field maps that are calculated from a set of boundary conditions by RELAX3D [26], an iterative relaxation code. The volume of interest is described by a matrix of potential values with Neumann [26] boundary conditions on the edges of the volume and Dirichlet [26] boundary conditions on the edges of each electrode within the volume. The chimney

and plasma boundary are normally modeled as a single solid object at ground potential. We would like to start orbit tracking on the edge of the plasma boundary, where $V = 0$.

The Z3CYCLONE orbit code uses a four-point interpolation algorithm to calculate electric fields from the potential map provided by RELAX3D. On the two sides of a conductor surface a discontinuity in the gradient exists (zero in the conductor, and $-\nabla V$ outside) which can result in inaccurate values for the electric field if points on the two sides of the surface are used in the same interpolation interval. For four-point interpolation it is therefore desirable to always keep at least two grid points between the ions and any electrode surface. This is particularly important at the exit of the ion source where the ion energy is at its lowest; we therefore cannot model the plasma boundary as a solid object.

Previous investigators have extrapolated the external potential function in an 'eyeball' manner to obtain points inside the chimney to provide the needed 'smooth' data for Z3CYCLONE to obtain reasonable intermediate values by interpolation [27]. Less laborious methods include reducing the radius of the chimney by a few grid points while raising the voltage of the chimney to a positive value so that the potential is zero at the desired starting point of the ion. An alternative method is to make a small notch in the surface of the electrode [25]. The ion starts in the middle of the notch so that it is at least 2 grid points from a grounded surface but still in a potential that is very near to zero.

The new method developed for this study combines the last two: the chimney is represented as the hollow shell that it is, with the ion starting in the middle of the chimney hole, which is at least two grid points in radius. The potential at the starting point is raised to zero by placing a cylindrical 'image-electrode' with an

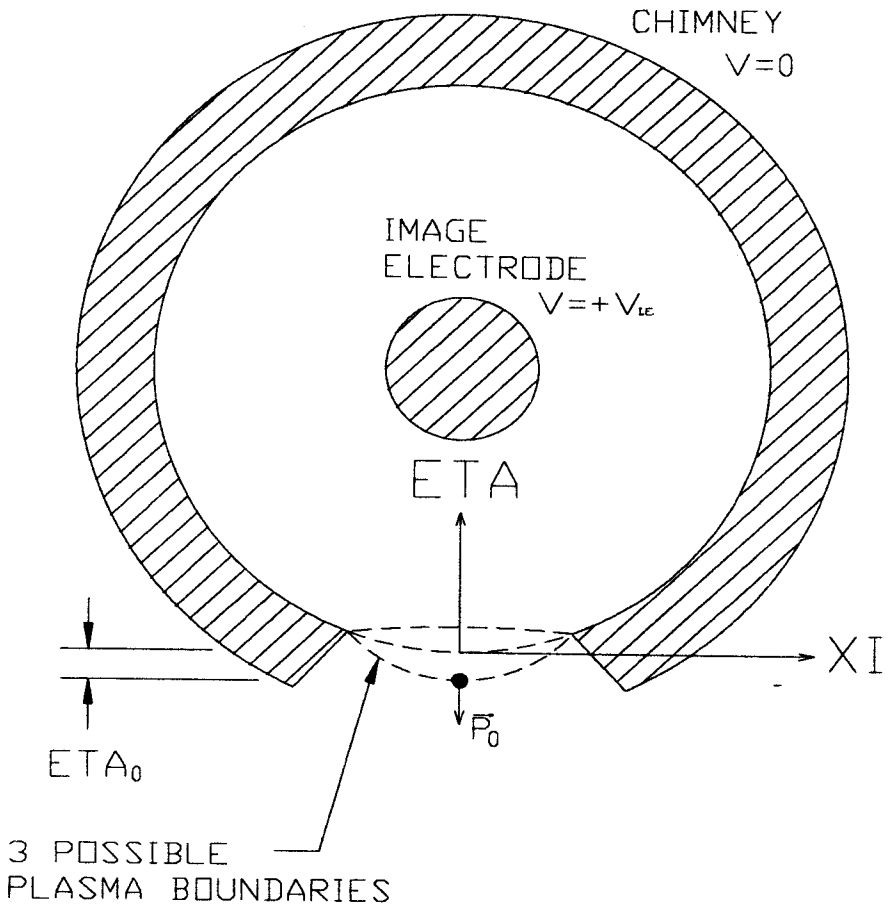

Figure 3.2: Schematic (not calculated) of the electrodes used to shape the plasma boundary, and three possible V=0 contours resulting from different potentials applied to the image-electrode. Ions are started in the Cartesian ξ-η coordinate system whose origin coincides with a point that is concentric with the inner radius of the chimney, and is centered in the chimney hole. Different plasma boundaries are referred to by the η coordinate of their central point.

arbitrary positive voltage on the axis of the chimney (figure 3.2). (This is the only object in the model that is not geometrically similar to the object in the cyclotron that it is modeling.) This arrangement results in a smooth continuous voltage field with a $V = 0$ equipotential surface in the mouth of the chimney which we use as our nominal plasma boundary. Ions may be started on this $V = 0$ plasma boundary and, since derivatives are continuous, the interpolation algorithm used in Z3CYCLONE becomes a correct representation of an actual Maxwellian field.

The position of the zero-voltage equipotential may be manipulated to bulge outward or inward by raising or lowering the voltage of the image-electrode. Since the solutions created automatically obey Laplace's equation, any might be the 'true' plasma boundary geometry.

This method provides a physically reasonable model of the chimney hole structure and provides a novel tool for simulation studies of the effect of various possible plasma boundary geometries.

3.6 Test of Three Plasma Boundary Geometries

To investigate the effect of small changes in the plasma boundary we ran three rays in a model of the central region of the Harper Medical Cyclotron. The electrodes used to produce a field map in the source-puller region are shown in figure 3.3. An image-electrode voltage was found to produce a zero-voltage equipotential that was concentric with the inner radius of the chimney to better than .0002 in. We identify different plasma boundary geometries by where they intersect the η axis (at the median plane) in the η-ξ coordinate system defined in Figure 3.2. The voltage on the image-electrode was then raised and lowered to produce two additional field maps, one

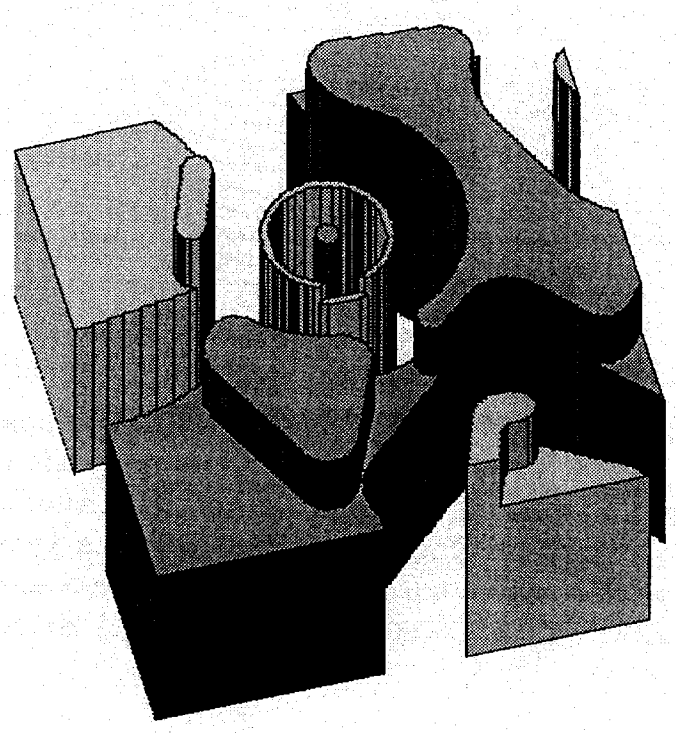

Figure 3.3: Lower half of the central region electrode model used to calculate the electric field for Part I of Z3CYCLONE. The .05 in. diameter image-electrode in the center of the ion source chimney is used to simulate the effect of the neutral plasma that fills the chimney when the cyclotron is in operation. The volume of the figure is 1"×1"×0.75".

with a plasma boundary that bulged .0035" inward ($\eta_o = +0.0035$,) the other with a plasma-boundary bulging .0070" outward ($\eta_o = -0.0070$,) relative to the concentric case. The three field maps are plotted in figure 3.4. The effect of changes in the plasma boundary shape become negligible beyond the middle of the first acceleration gap.

For each of the geometries an orbit starting location was found which was in the center of the hole ($\xi_o = 0, z = 0$) and very close to the $V = 0$ surface, so η_o is also the initial value of η for the ion. A 10 eV/u deuteron was started from that point at an RF time of 210°. All three starting points and momentum vectors fall on a line that originates at the center of the chimney. The first orbits of each case are plotted in figure 3.5. The orbit that starts on the concentric plasma boundary and

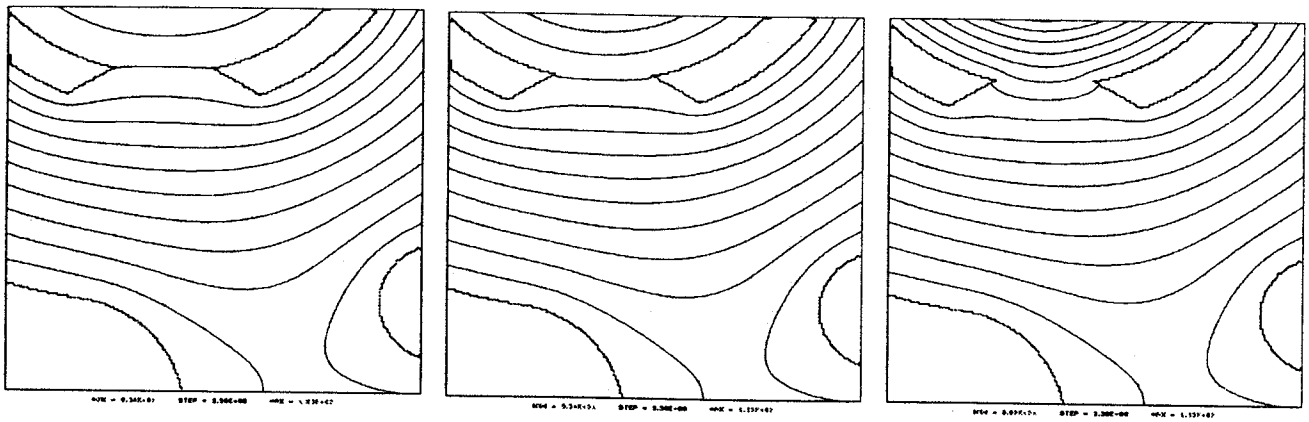

Figure 3.4: Three equipotential contour plots of the three electric fields calculated by RELAX3D from the geometry shown in figure 3.1. Only the region in the first accelerating gap is shown. By manipulating the image-electrode voltage we can generate electric fields with a zero-potential contour (the nominal plasma-boundary) that is concentric with the inner radius of the chimney (middle) concave relative to the chimney (left) or convex (right). The area shown is 0.2" × 0.2" and the mesh size is 0.001".

clears the posts will be referred to hereafter as the 'reference orbit.' We see that the 'forward ion' (*i.e.* the ion starting on the convex plasma-boundary) experiences a greater energy gain than the others, and hence travels a straighter path in the first accelerating gap. The initial energy and phase were chosen so that the ion starting from the concentric plasma boundary would be nearly centered. The effect of the small changes in the plasma geometry are so great that the other two ions are lost by the fourth set of posts.

3.7 Relationship of η_0, τ_0, and E_0

A few properties of each ion's flight through the first acceleration gap are listed in Table 3.1. We see that there is a considerable difference in energy gain with the forward ion being accelerated the most. There is also a difference in arrival times at the puller, with the forward ion arriving first. One possible explanation is that these differences are the result of the time lost by the rear (or reference) ion in 'catching up' with the reference (or forward) ion. Since the starting energy is low, a large

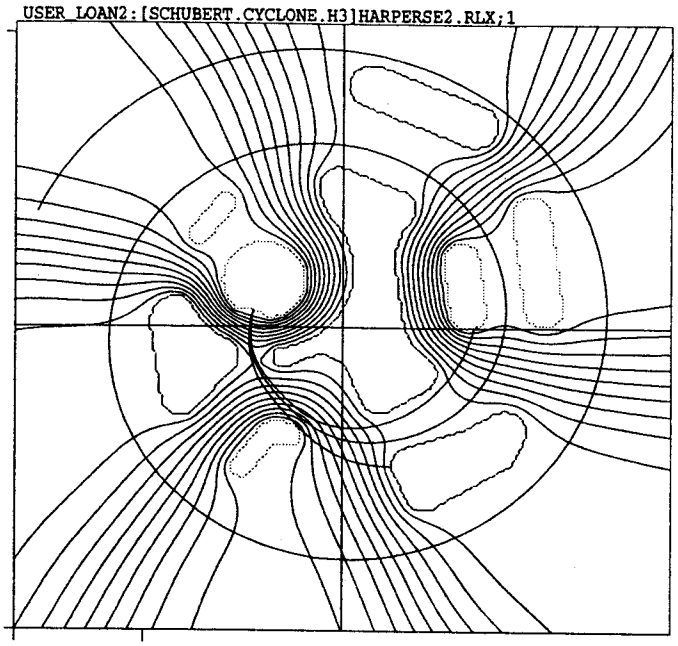

Figure 3.5: The three orbits are superimposed on a field map that is large enough to show the first few turns. The forward ion follows the outside orbit and the rear ion follows the inside orbit. The peak dee voltage was 35 kV. The map is 2"×2".

fraction of the rf cycle is used in covering the first few mils of path length. If this were the only difference between the three cases, then it would be possible to change the forward ray's path to match the reference path by changing its starting time and energy to match those of the reference ion when it passes η=7 mils. (Lateral motion of the reference ion is roughly half of a mil at this point and has little effect on the energy gain in the first gap.) This experiment resulted in a path that looked more like the original forward ray than the reference ray. Adjusting the reference ray to match the rear ray was similarly unsuccessful, suggesting that the difference in path length is only a small factor in determining the energy gain in the source-puller gap.

To better understand the energy gain advantage experienced by the forward ions we plot the potential seen by each ion as a function of path length in Figure 3.6a. Using this data and the time and position data from Part I of Z3CYCLONE, it is possible to reconstruct the electric field amplitude seen by each ion (Figure 3.6b)

Table 3.1: Properties of orbits starting from different plasma boundaries with the same time and energy. η_o, the coordinate measuring the 'straight ahead' distance from the inner circular surface of the ion source chimney, is listed in units of 0.001"; τ is listed in degrees of RF time, where $\tau = 90$ is peak positive voltage.

Ion Location		Plasma Boundary Geometry		
		Concave $\eta_o = +3$	Concentric $\eta_o = 0$	Convex $\eta_o = -7$
Concave geometry starting position	$\eta = +3$	$\tau = 210°$ $E = 10$ eV		
Approximate concentric geometry starting position	$\eta = 0$	$\tau = 235.5°$ $E = 280$ eV	$\tau = 210°$ $E = 10$ eV	
Convex geometry starting position	$\eta = -7$	$\tau = 256°$ $E = 1000$ eV	$\tau = 246°$ $E = 750$ eV	$\tau = 210°$ $E = 10$ eV
Center of puller gap	$\theta = 202°$	$\tau = 34.5°$ $E = 8890$ eV	$\tau = 23.5°$ $E = 10260$ eV	$\tau = 6°$ $E = 12220$ eV

and the effect of the RF time dependence on the electric field (Figures 3.6c,d.) The total energy of each ion, as a function of path length, is plotted in Figure 3.6e. The convex plasma boundary results in a field map with a higher electric field near the chimney, but a lower electric field near the puller relative to the other cases. If the potential field were constant in time then all three ions would gain the same energy, since each would begin and end at the same potential. The RF wave, however, is near its maximum when the ions are near the chimney and near zero as the ions approach the puller. Since the ions start at a time when the field is near its maximum value, the shape of the field near the starting position is more important than the shape of the field near the puller, which the ions do not see until the RF time factor is nearly zero.

The effect of this gradient change is better understood by considering an ion in a

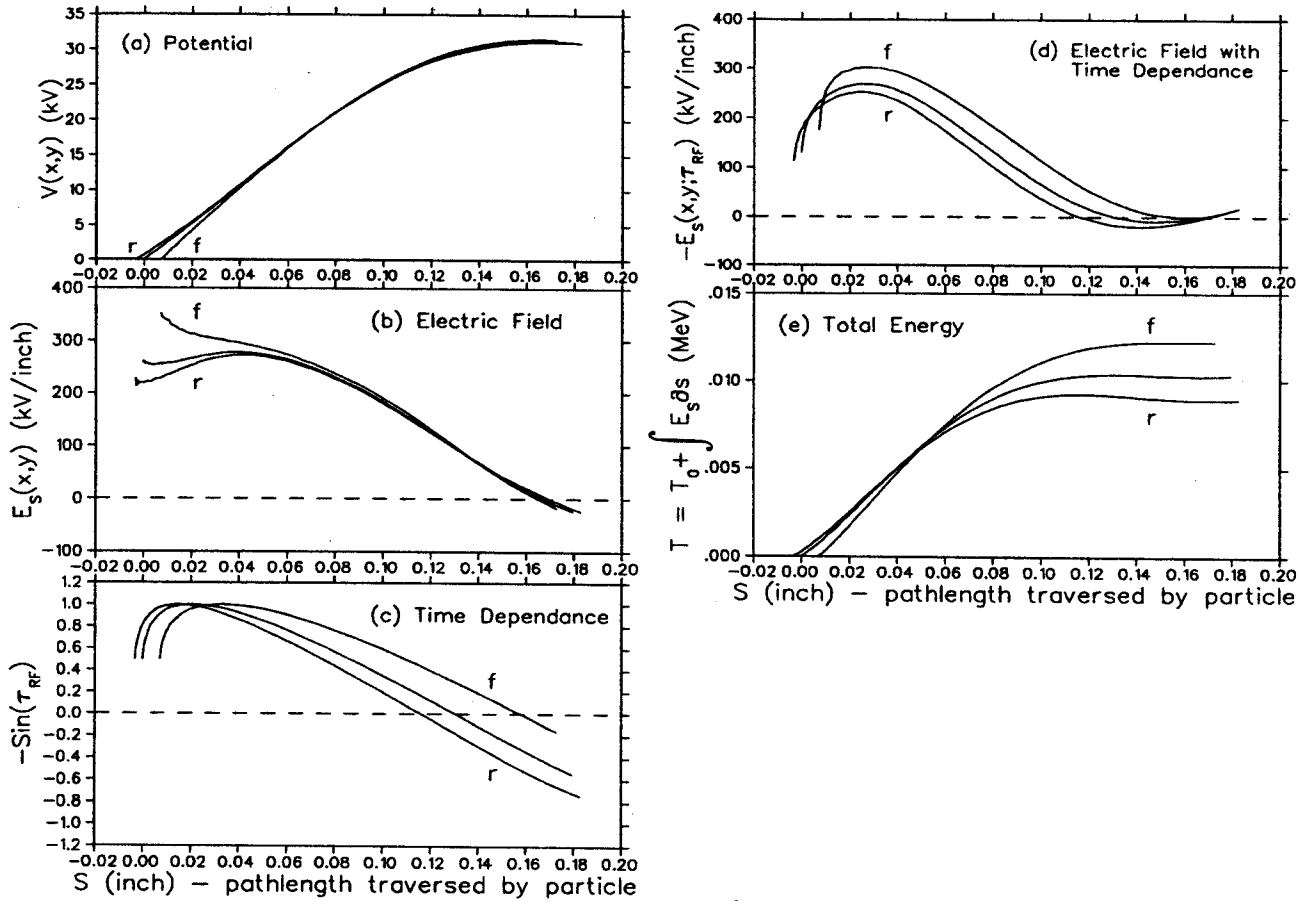

Figure 3.6: Properties of the ions that contribute to energy gain in the source-to-puller gap. Path length s is defined as zero for an ion starting at $\eta_o = 0$. In each graph 'f' refers to the ion with the forward starting position (the convex plasma boundary) and 'r' refers to the ion with the rear starting position. (a) The potential field sliced along each of the ions' paths, not accounting for time dependence. Note that near the source the difference is dominated by the shape of the plasma boundary. Near the puller the difference is dominated by the different paths of the three ions. (b) The electric field parallel to ion motion $E_s = \partial V/\partial s$. (c) The time dependence factor $-\sin(\tau_{RF}(s))$. We see that the potential gradient in the first half of the gap is emphasized over that of the last half of the gap, but also that the forward ion is closer to its optimum starting phase. (d) The time dependent electric field (the field seen by the ion) is simply the product of the previous two functions. This is also the instantaneous energy gain as a function of path length rather than time. (e) The total ion energy is the integral of the time dependent electric field with respect to path length.

simple capacitor (figure 3.7). The shorter capacitor (b) is related to the more convex plasma boundary. Turning off the voltage in a single step is sufficient to reproduce an energy gain graph that is qualitatively similar to figure 3.6e.

A similar analysis may be applied to the effect of timing and path length discussed above (figure 3.8). Although the energy gain for a single step in the time function is clearly different from that of figure 3.7, when we include more than one step (figure 3.9) we see that the data in figure 6e may be a combination of the two effects. In both cases, one ion is allowed to sample more of the electric field than the other before the field is turned off. A change in initial energy (velocity) then, should also yield a change in energy gain similar to figures 3.8 and 3.9.

If geometry, initial time, and initial energy all have similar effects on the energy gain in the first acceleration gap, then we should be able to compensate for changes in any one parameter with one or both of the others. To test this hypothesis we search for sets of starting parameters in each of the three geometries that yield the same energy gain in the first gap as the reference orbit. (The end of the source-puller gap is defined as the $\theta = 202°$ azimuth. At this point the electric field amplitude is near a minimum.) Two such orbits are plotted against the reference orbit in figure 3.10. Both orbits start on the concave plasma boundary. One uses an early starting time to catch up with the reference orbit and the other uses a high starting energy. These orbits are referred to as 'early' and 'fast' respectively.

Figure 3.11 shows starting parameters for these and ten other rays that form similar orbits. We see that within the 3-dimensional 'initial-parameter-space' with the coordinates of E_0, τ_0, and η_0 there exists a 2-dimensional surface of (E_0,τ_0,η_0) sets that yield similar orbits.

The evolution of all twelve points is plotted in E-τ and r-p_r phase space in Fig-

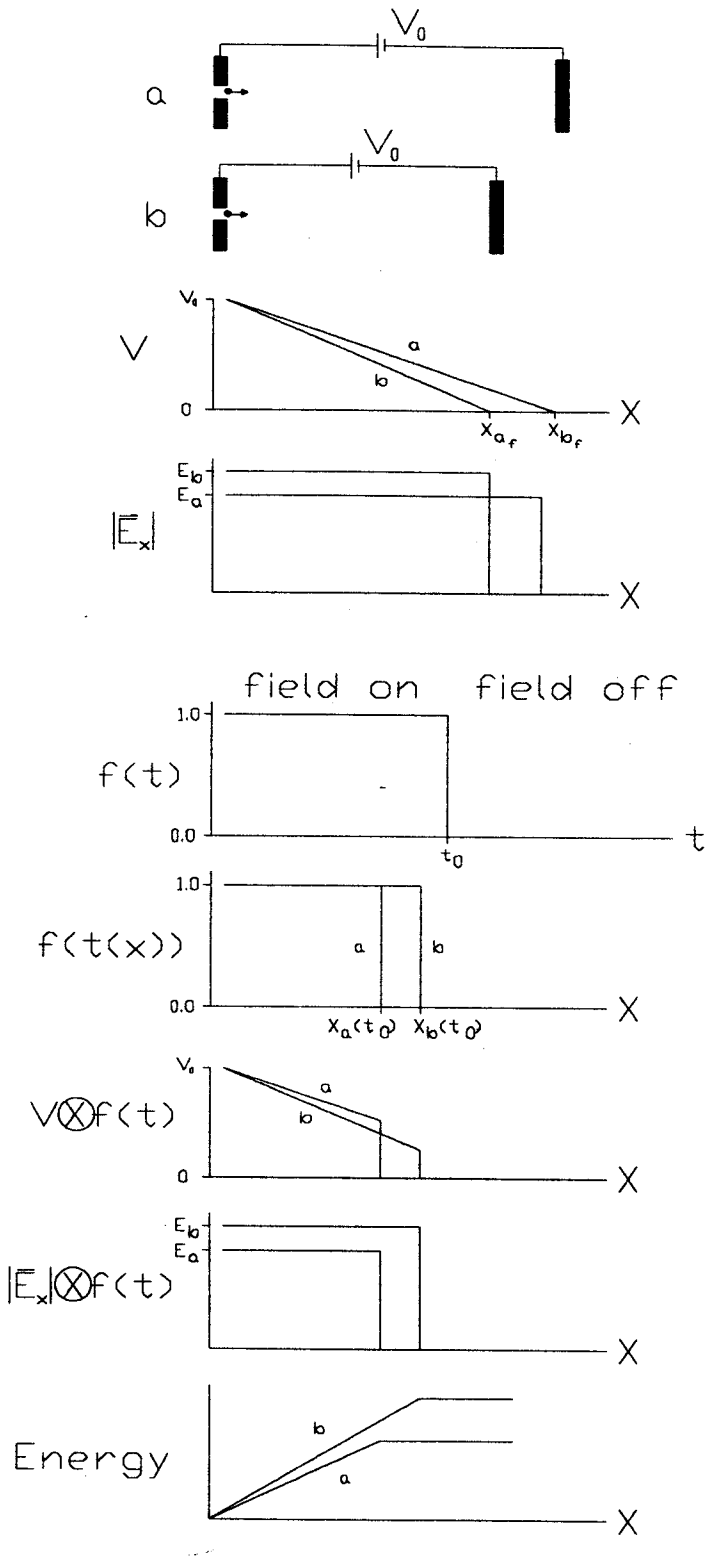

Figure 3.7: The effect of changes in gradient in a 1-dimensional gap with a step-function voltage time dependence. The ion in the higher electric field samples more of the voltage drop before the field is turned off than the ion in the lower electric field.

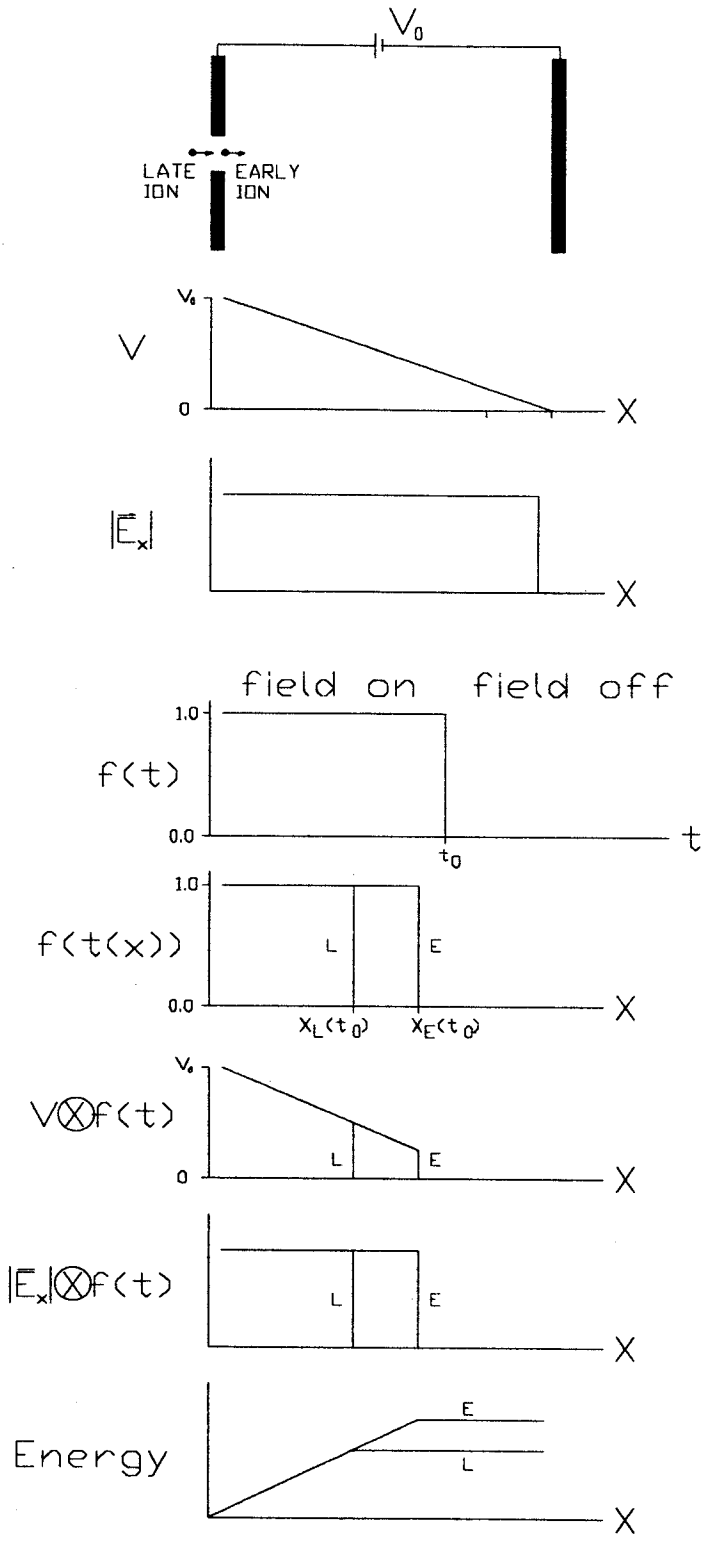

Figure 3.8: The effect of changes in starting time in a 1-dimensional gap with a step-function voltage time dependence. The early ion samples more of the electric field before it is turned off than the late ion. The same would be true for an ion with a high starting energy (and velocity) compared to a slower ion.

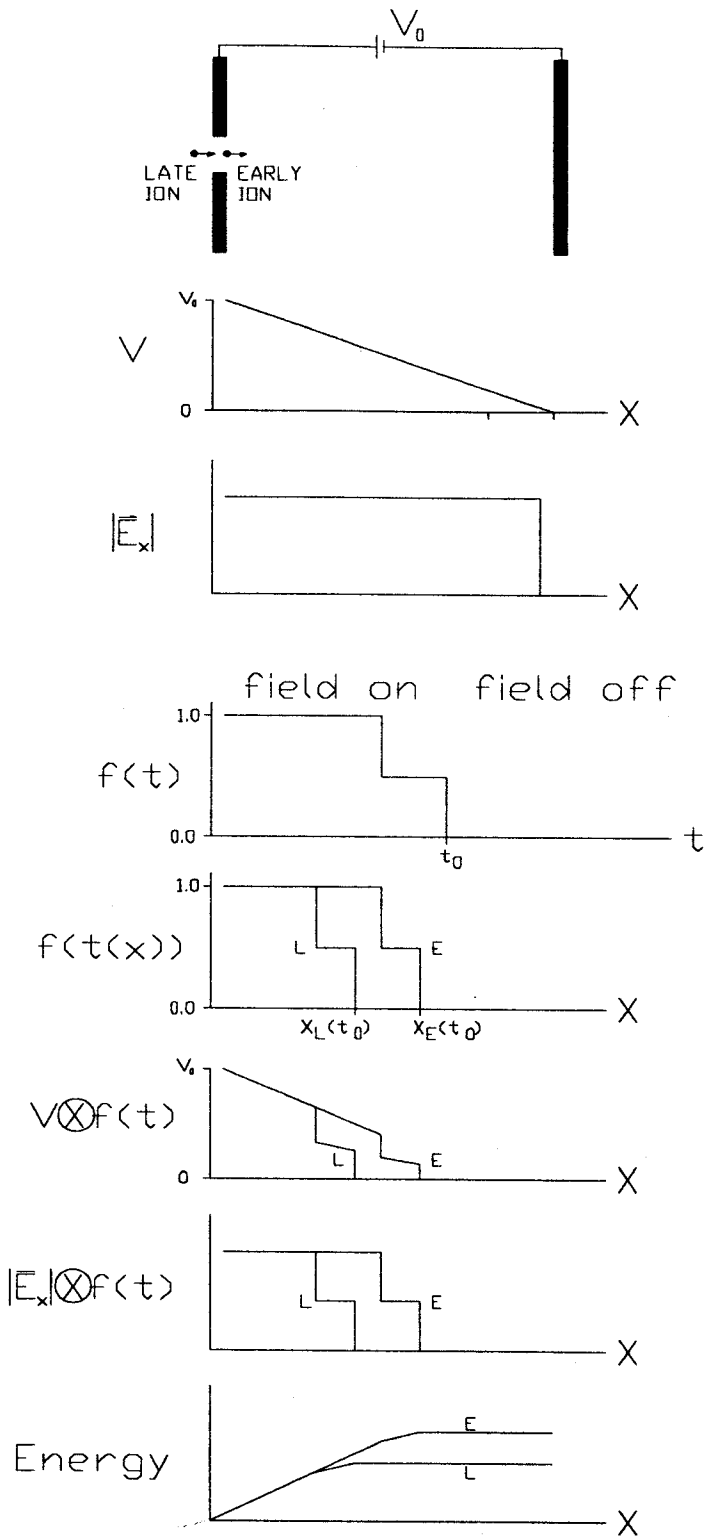

Figure 3.9: The effect of changes in starting time or starting energy in a 1-dimensional gap with a two-step voltage time dependence.

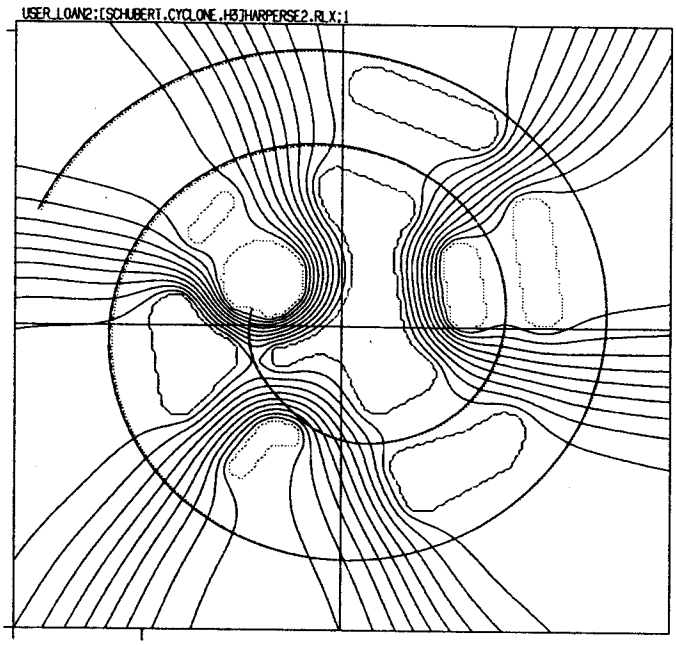

Figure 3.10: The reference orbit (concentric plasma boundary) and two orbits starting on the concave plasma boundary. The dashed orbit uses a higher initial energy than the reference orbit and the dotted orbit uses an earlier starting time to achieve the same energy gain in the first acceleration gap.

ures 3.12 and 3.13 respectively. Notice that for rays on the surface of Figure 3.11, a 60° phase width is bunched to less than 6° in the source puller gap. Afterwards all rays stay within this phase width and within an energy spread of less than 4 keV at least as far as the tenth turn. The radial spread of the orbits never grows larger than 0.025" (0.6 mm). Notice that in the third and fifth frames of Figure 3.12 the phase spread is less than 1° while the energy spread is nearly maximized. This seems to suggest that had our criterion for choosing initial conditions been matching times at a given azimuth rather than matching energies, we would have found an almost identical surface in the starting-parameter space.

To understand how these orbits came to be so alike we return to three starting conditions of Figure 3.10, where the reference ray (E_0=10eV/u, τ_0=210°, concentric plasma boundary) is compared to a fast ray (E_0=84 eV/u) and an early ray (τ_0=186) both started on the concave plasma boundary. Figure 3.14 is the same type of analysis

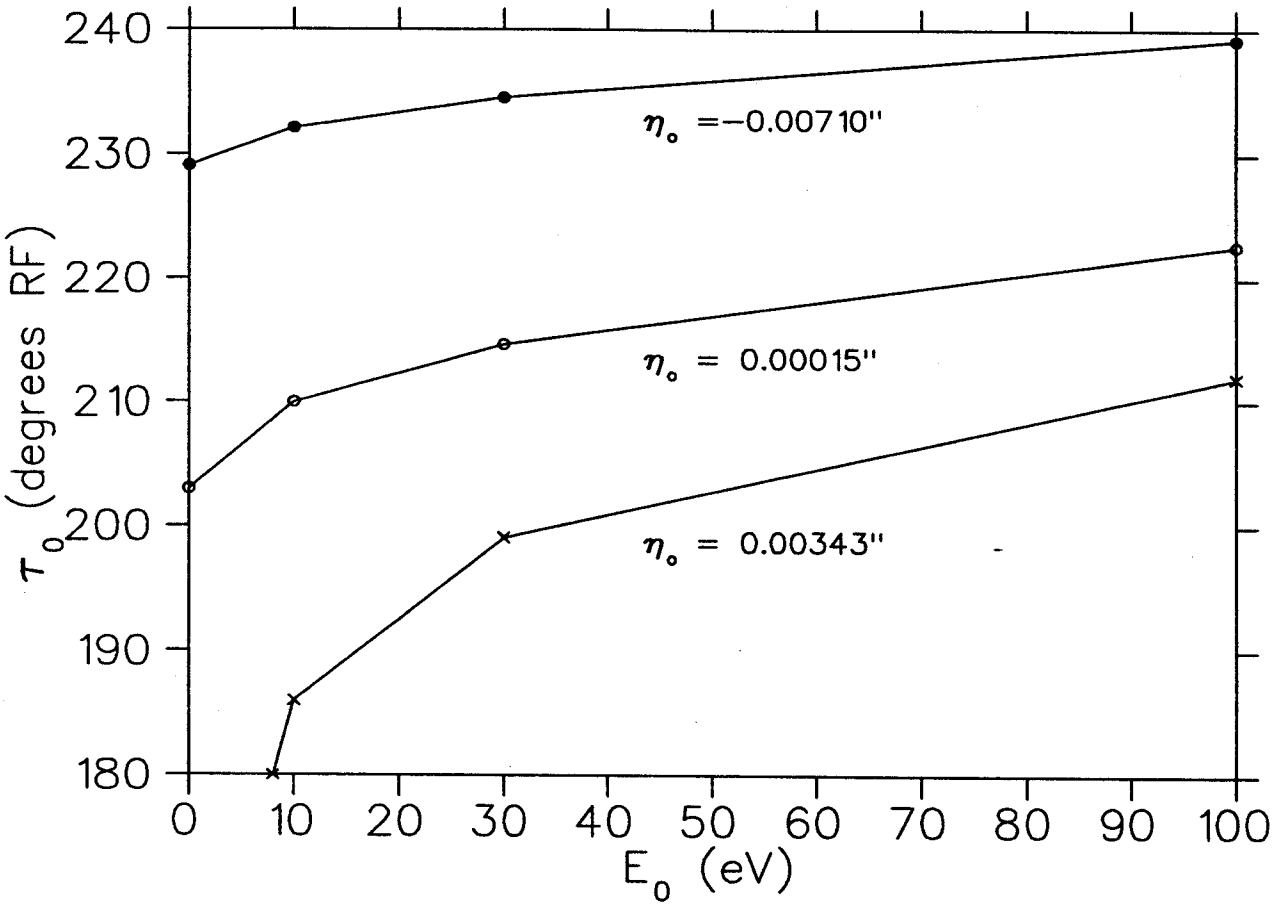

Figure 3.11: Initial conditions in E_0-τ_0-η_0 space that yield the same energy (E=10.26 keV) at the puller (θ=202°) and hence, similar R-θ paths throughout the central region.

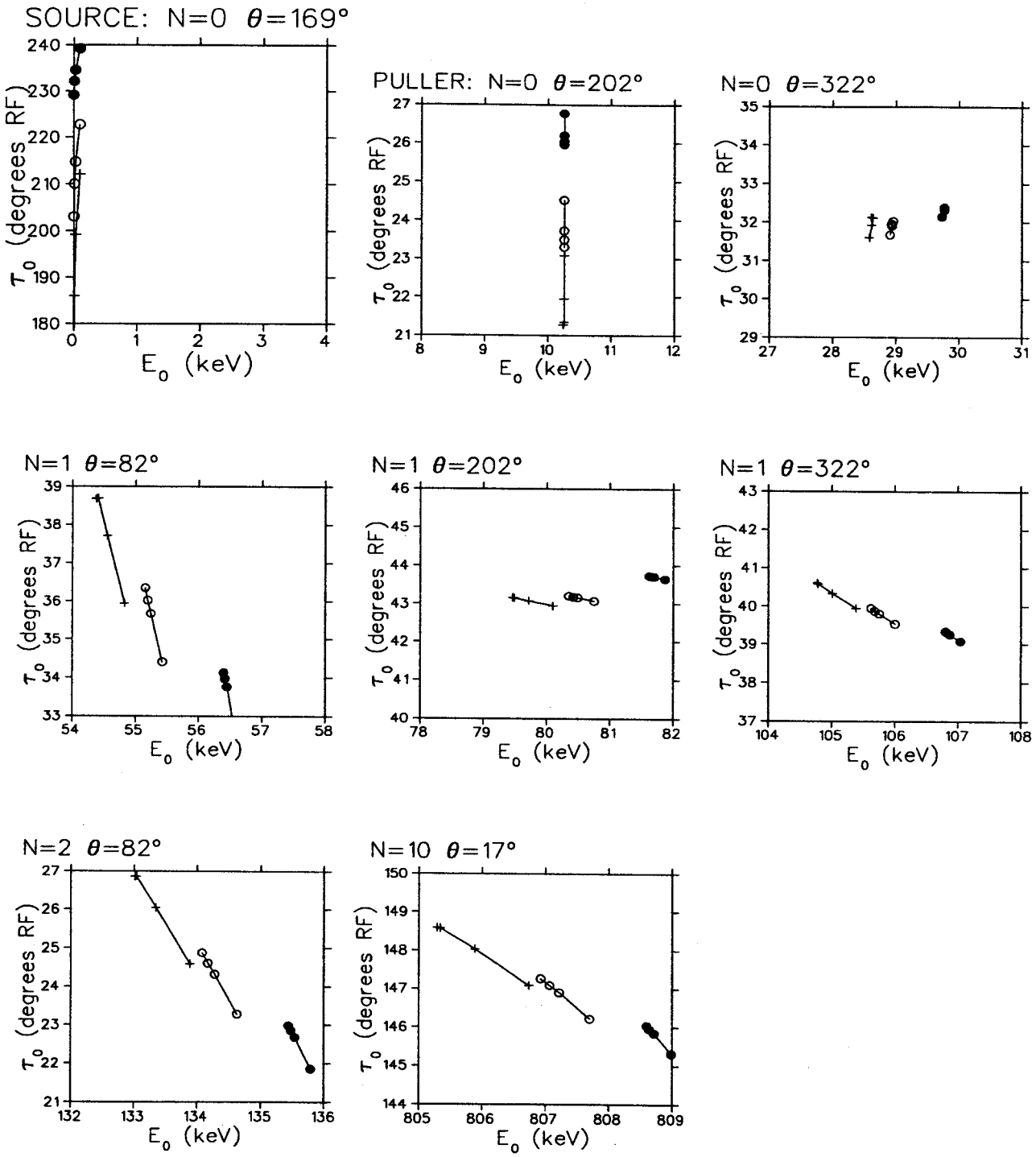

Figure 3.12: Evolution in E-τ space of the twelve rays with the same energy gain in the source puller gap.

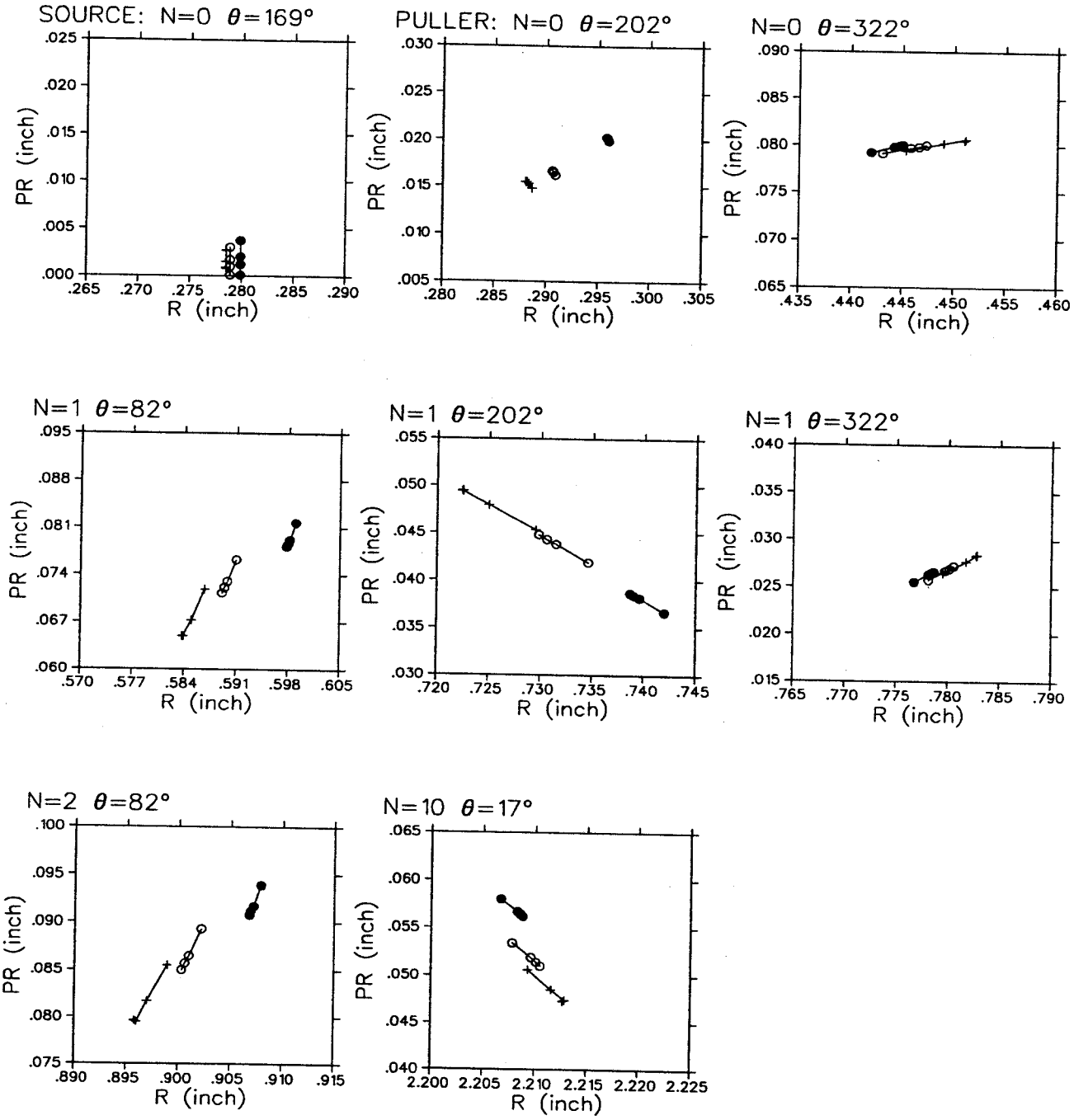

Figure 3.13: Evolution in r-p_r space of the twelve rays with the same energy gain in the source puller gap.

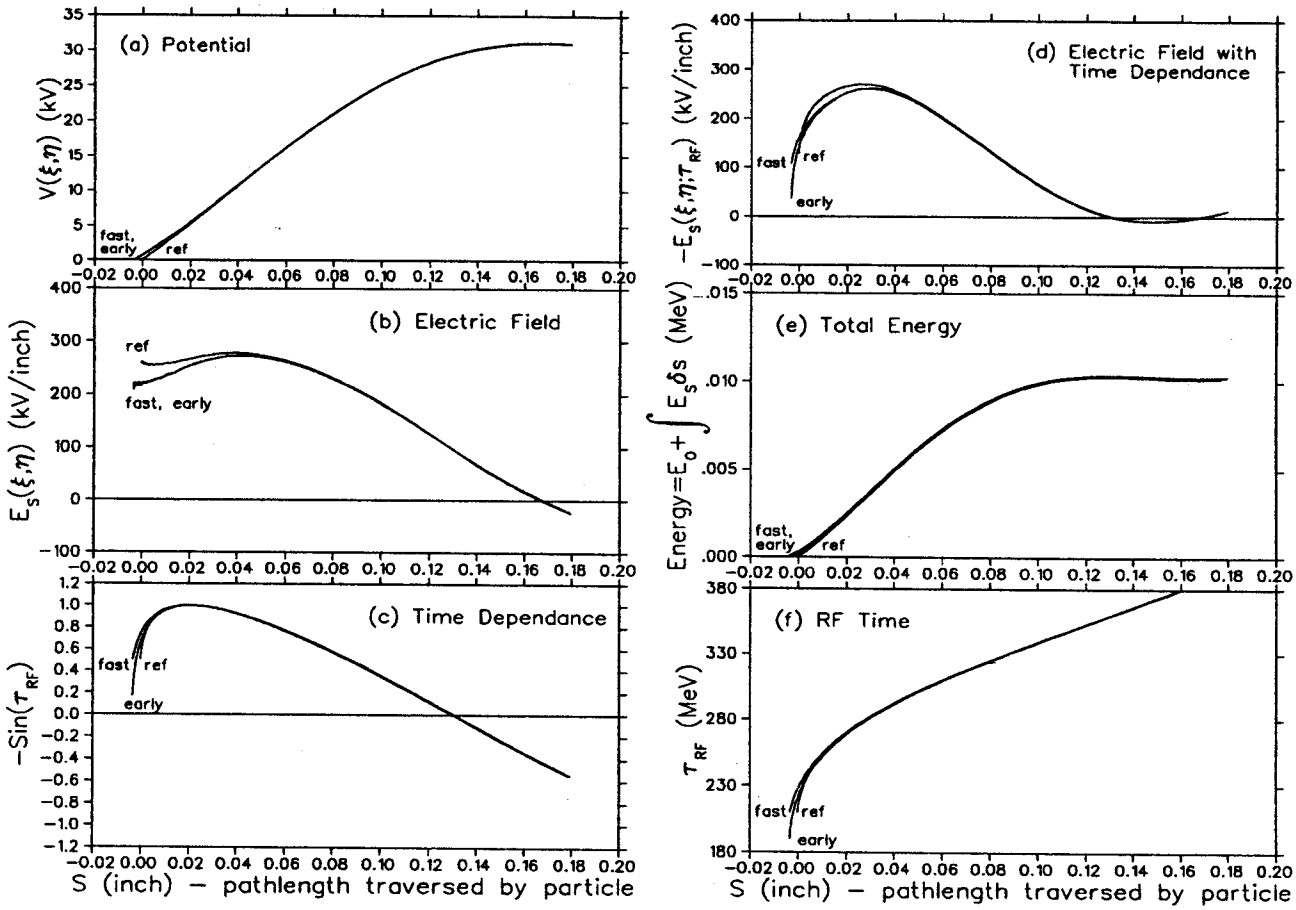

Figure 3.14: Properties of the ions that contribute to energy gain in the source-to-puller gap. In each graph 'ref' refers to the reference ion that starts on the concentric plasma boundary at time τ_o=210° with energy E_o=10eV/u. 'Fast' refers to the ion starting on the concave plasma boundary with a starting energy of E_o=84 eV/u. 'Early' refers to the ion starting on the concave plasma boundary at a starting time τ_o=186° The analysis of Figures 3.14(a)-3.14(e) is identical to that of Figure 3.6(a)-3.6(e). (f) RF time as a function of pathlength. The 'early' ion catches up with the reference ion first. The fast ion catches up a short time later.

as presented in Figure 3.6. Although the three ions experience different electric fields during the first 0.050" of path length (Figure 3.14d) the electric fields integrate to very similar total energy gains after the starting conditions have been manipulated (Figure 3.14e). Figure 3.14f plots RF time as a function of pathlength, to show the 'early' and 'fast' ions 'catching up' to the reference orbit.

Figure 3.15 shows another illustration of the same phenomenon. The first 75% of each ion's path in the source-puller gap is plotted with times and energies marked at 15° intervals. The fast ion overtakes the reference ion in roughly the first 35 mils of path length. At the same time the fast ion gradually loses energy gain (slowing down in the reference frame of the reference ion) due to the reduced effective electric field in its geometry. The early ion has not yet caught up to the reference ion by the time the reference ion begins its orbit at τ=210°. The early ion has, however, acquired an energy of 80 eV/u by this time, essentially becoming another fast ion, but with a longer path length to cover and a lower effective electric field, so that by the end of the gap all three ions may arrive at a similar time with a similar energy.

In summary, we have learned the following about the initial parameters of starting time, starting energy, and shape of the plasma boundary.

- Seemingly small changes in the shape of the plasma boundary (3-7 mils) can result in large changes in the energy and phase of the beam at the end of the first acceleration gap which can have a large enough effect on the beam's trajectory such that orbits fail to clear the posts in the central region.

- The starting time (τ_0) and/or starting energy (E_0) in the Z3CYCLONE model may be adjusted to approximately compensate for small changes in η_0. E_0 may also be adjusted to compensate for changes in τ_0 and visa versa. Therefore within the

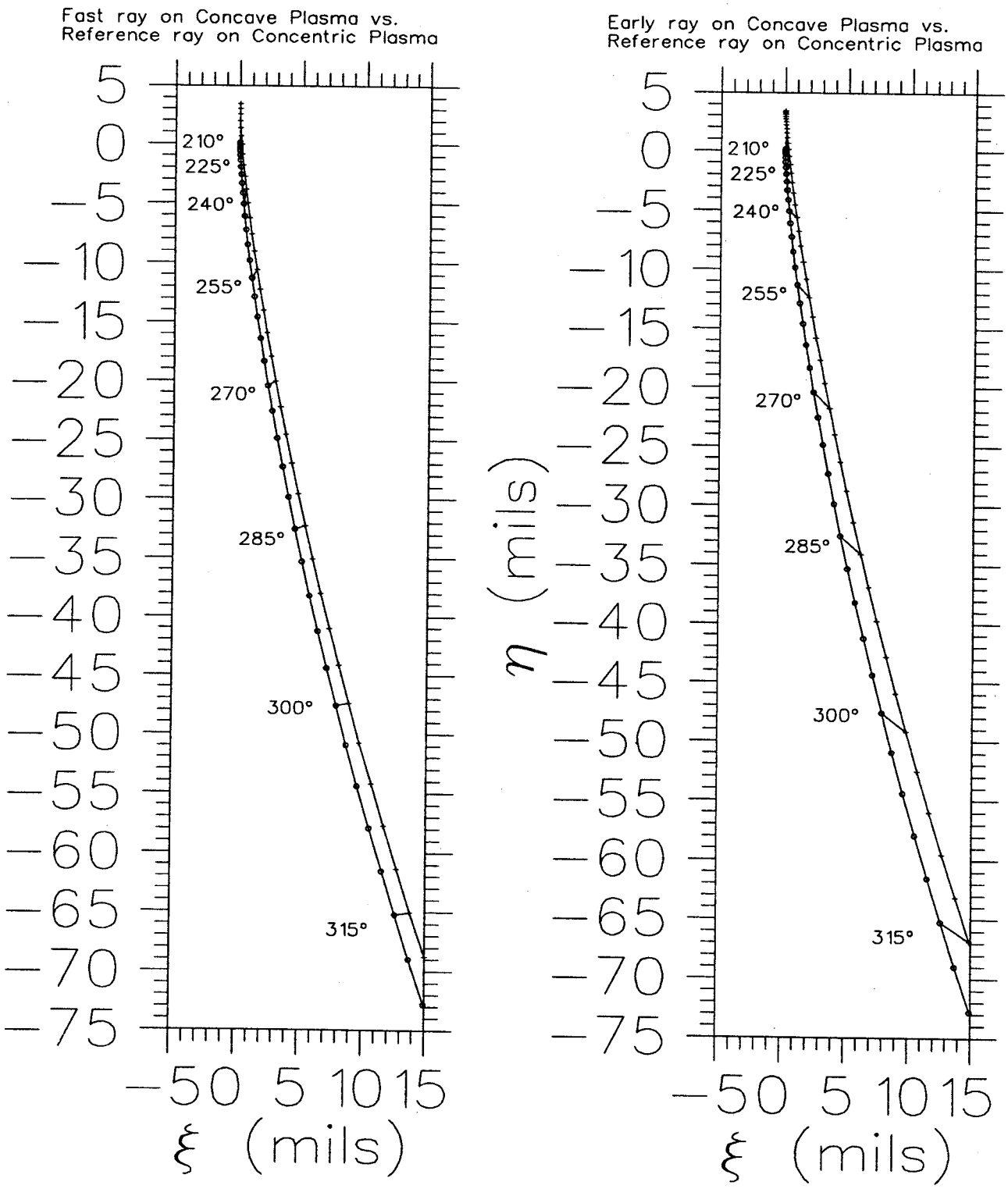

Figure 3.15: Paths of the 'fast' and 'early' orbits (each with a "+" marking intervals $3°RF$) against the reference orbit ("o" plotted every $3°RF$) in the source-to-puller gap. The 'fast' and 'early' ions begin on the concave plasma boundary, 0.0035" behind the reference ion.

3-dimensional 'initial-parameter-space' with the coordinates of E_0, τ_0, and η_0 there exists a 2-dimensional surface of (E_0,τ_0,η_0) sets that yield similar orbits.

3.8 Comparison of Z3CYCLONE simulation with a Foil-Burning Experiment

Our inability to determine the shape of the source side of the first accelerating gap and the starting time for orbits, and our imprecise knowledge of the starting energy would seem to eliminate any hope of identifying a set of starting parameters to match actual beam position data, because the volume of initial-parameter space that must be searched grows exponentially with each additional unknown. The fact that shifts in η_0, τ_0, and E_0 can compensate for one another, however, greatly reduces the searching needed to find a set of initial conditions that yields meaningful predictions of the true orbit path.

In order to test our ability to match actual data with Z3CYCLONE we performed a 'foil-burning' experiment similar to those performed on the K50 and K500 at the NSCL [28, 29]. A set of three stainless steel mesh 'foils' (0.001" diameter wire, 325 wires/inch mesh) were set perpendicular to the beam near the central azimuth of each hill. Holes melted in the foils reveal the position and some information about the shape of the densest part of the beam. The foils extended from an inner radius of 0.7" to 0.8" (depending on the position of the outer post for each hill) to 2.125". At the maximum energy for the experiment (0.7 MeV/u) deuterons only penetrate $8\mu m$ into stainless steel, so the effect of beam being decelerated or redirected by interaction with the foils should be negligible, resulting only from glancing collisions with the edges of the wires in the foils.

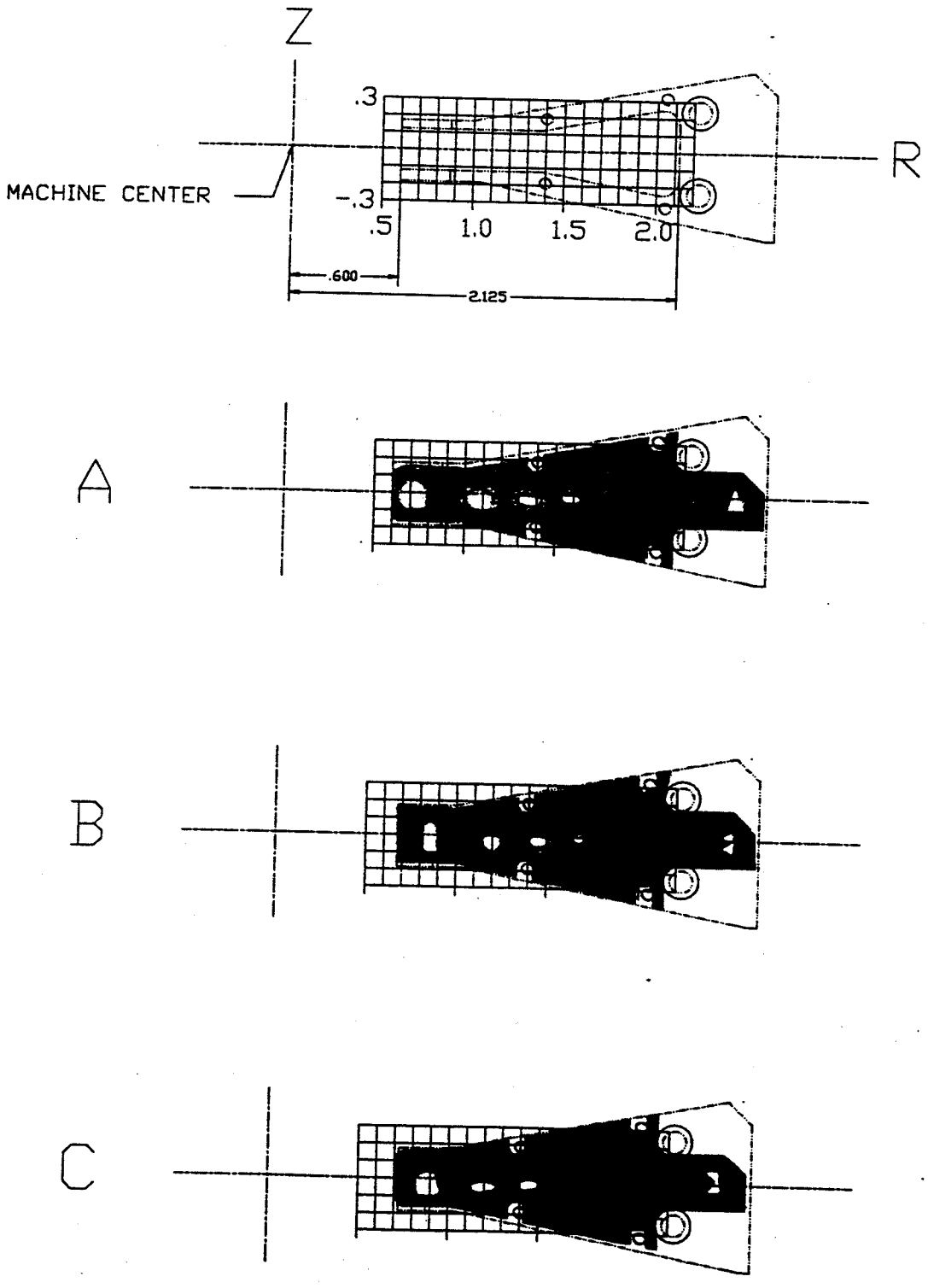

Figure 3.16: Hole patterns burned in stainless steel mesh 'foils.' the three foils are exposed simultaneously at azimuths (A) 138°, (B) 258° and (C) 18°.

The three foils were burned simultaneously for about six minutes. The resulting hole pattern is shown in Figure 3.16. Orbit radii based on the center of each hole are indicated with circles in Figures 3.17, 3.18 and 3.19 with bars to indicate the width of the hole in the foil. The width of the inner holes might indicate a contour of a particular beam intensity. The outer holes (which were beyond the field of view from the windows on the Harper cyclotron) were probably still expanding when the experiment was stopped, and probably do not indicate the true width of the beam.

Immediately prior to the experiment the dee voltage was measured using the X-ray endpoint method [30]. We observe the X-ray spectra caused by electrons being accelerated between ground and the dees. X-rays are produced with energies ranging from 0 eV to the maximum dee voltage, so we are interested in the edge of the peak in the X-ray spectrum. The point where the tail of the X-ray spectrum meets the background spectrum is taken to be the peak dee voltage.

The precision of the measurement was limited by a low X-ray count rate, and the experiment is further complicated by the pulsed RF voltage [18] used in this cyclotron. Scope traces from an RF pickup loop indicated (before and during the experiment) that the peak voltage falls linearly with time during each 2 millisecond 100 Hz pulse. The X-ray measurement should measure the maximum voltage at the beginning of the pulse, but because this voltage held for only a short period of time the 'corner' where the X-ray data meets the background signal is not sharp. The peak dee voltage measured in this way appears to be 45-49 kV. The peak voltage at the end of the pulse is 15.4% lower than at the beginning of the pulse, so beam may be accelerated with a range of dee voltages that is up to 7 kV wide.

Because the voltage was higher than expected, a new set of orbit studies was required to attempt to match the data. A fit to the data was found using the concentric

plasma boundary from the previous sections, and a starting energy of 10 eV/u.

Prior to the experiment it was discovered that the chimney installed in the cyclotron might be rotated 7.6° counter clockwise relative to the one in our electric field maps. Because access to the cyclotron is limited, and radiation levels inside the machine are high, we were not able to measure the position of the chimney hole to this precision. We did, however, search laterally along the plasma boundary in the computer model to see if the lateral starting position had a significant effect on the centering of the orbit. As it turned out, starting the beam 0.015" to the right of the center of the chimney hole improved the fit slightly. (The starting angle of the ions was not changed, but its effect should be negligible due to the low starting energy.) Since the chimney has a radius of 0.125" this lateral change in starting position corresponds closely to the change in position of the chimney hole center if the chimney were rotated 7.6°. Future studies are therefore planned with an updated fieldmap using a rotated chimney.

Measurements of the central region after the experiment also revealed that the current chimney hole is 0.075" wide (rather than the 0.047" used to make the RELAX3D calculations) and that at the time of the experiment the source-to-puller difference was 0.122" rather than the 0.100" used here. The error in effective gap length caused by the change in source-to-puller difference is twice as great as what was investigated in section 3.7, however an experiment presented in section 6.6.2 suggests that differences greater than this still fail to change the structure of the beam orbits. When a new field map is available with these modifications we expect all of the starting times in our computations to shift to earlier values to compensate for the extra time needed to cross the first gap.

The best fit found for a single dee voltage appears to be at 44 kV with starting

times from $\tau_0 = 241°$-$245°$ clearing the central region posts. (See Figure 3.17.) In this cyclotron, the range of available dee voltages could cause more beam spreading than the range of starting times. Figure 3.18 shows the effect of 1 kV increments of dee voltage on the central ray starting at $\tau_0 = 243°$. In this case, only a range of 2 kV clears the posts. However, for each dee voltage we should consider a different range of starting times. Figure 3.19 shows a range of dee voltages from V_{dee} = 41-47 kV where for each dee voltage the range of starting times has been chosen to be that which clears the central region posts. Although it is no longer possible to compare the outer turns by a visual inspection, we can see that the first two to three turns now match not only the position, but the approximate width of each experimental turn as well.

At this time only one set of foil-data is available from the Harper Cyclotron, and more analysis of this data is in order. However, despite our imperfect knowledge of a variety initial conditions, we already are very close to a set of effective starting conditions capable of yielding orbit patterns in close agreement with the experimental result.

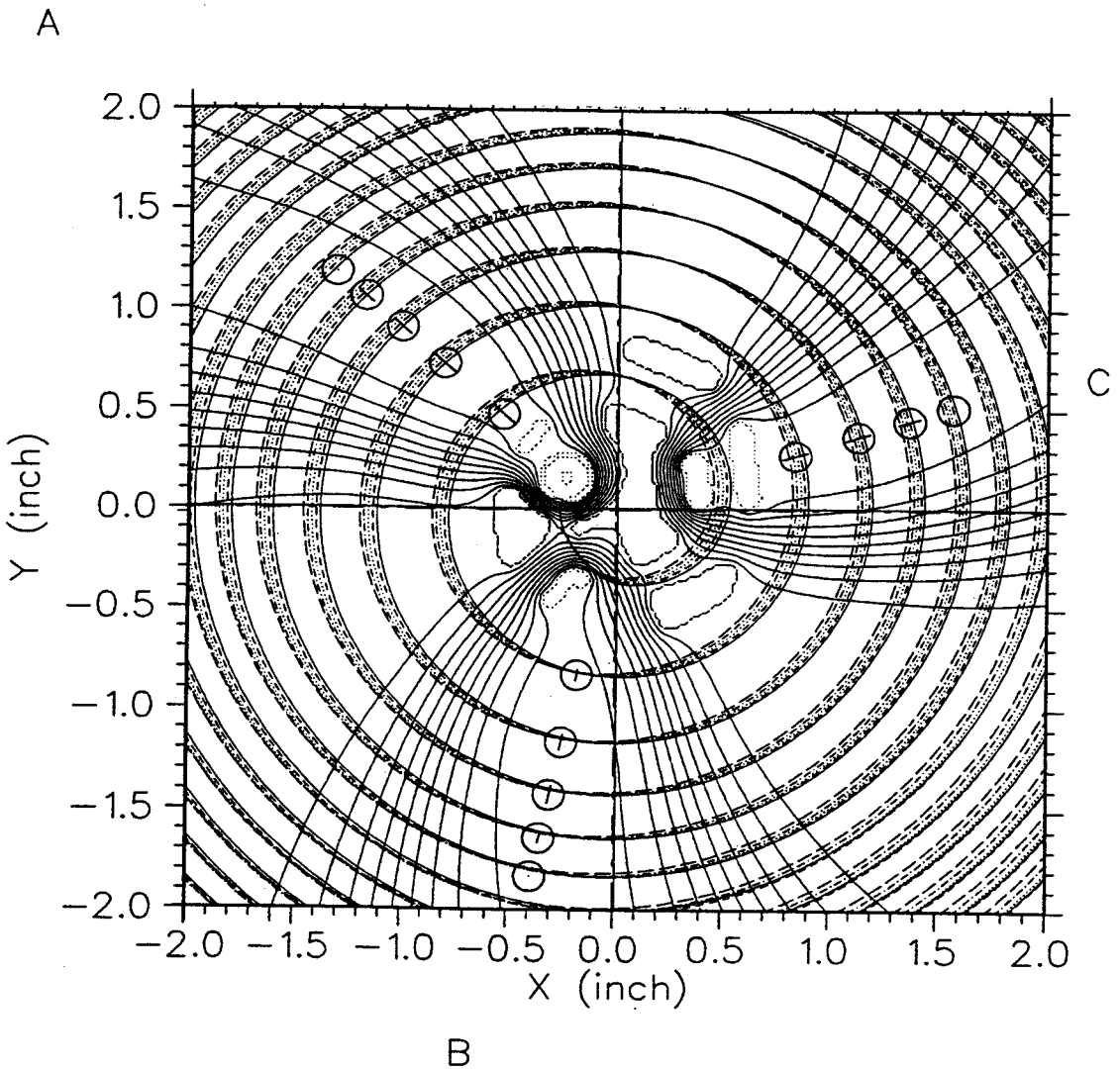

Figure 3.17: Calculated orbits for a dee voltage of $V_{dee} = 44$ kV with starting times from $\tau_o = 241°$ to $\tau_o = 245°$. Locations of the experimentally measured turns are marked with circles. Bars within the circles indicate the width of the holes burned in the foils.

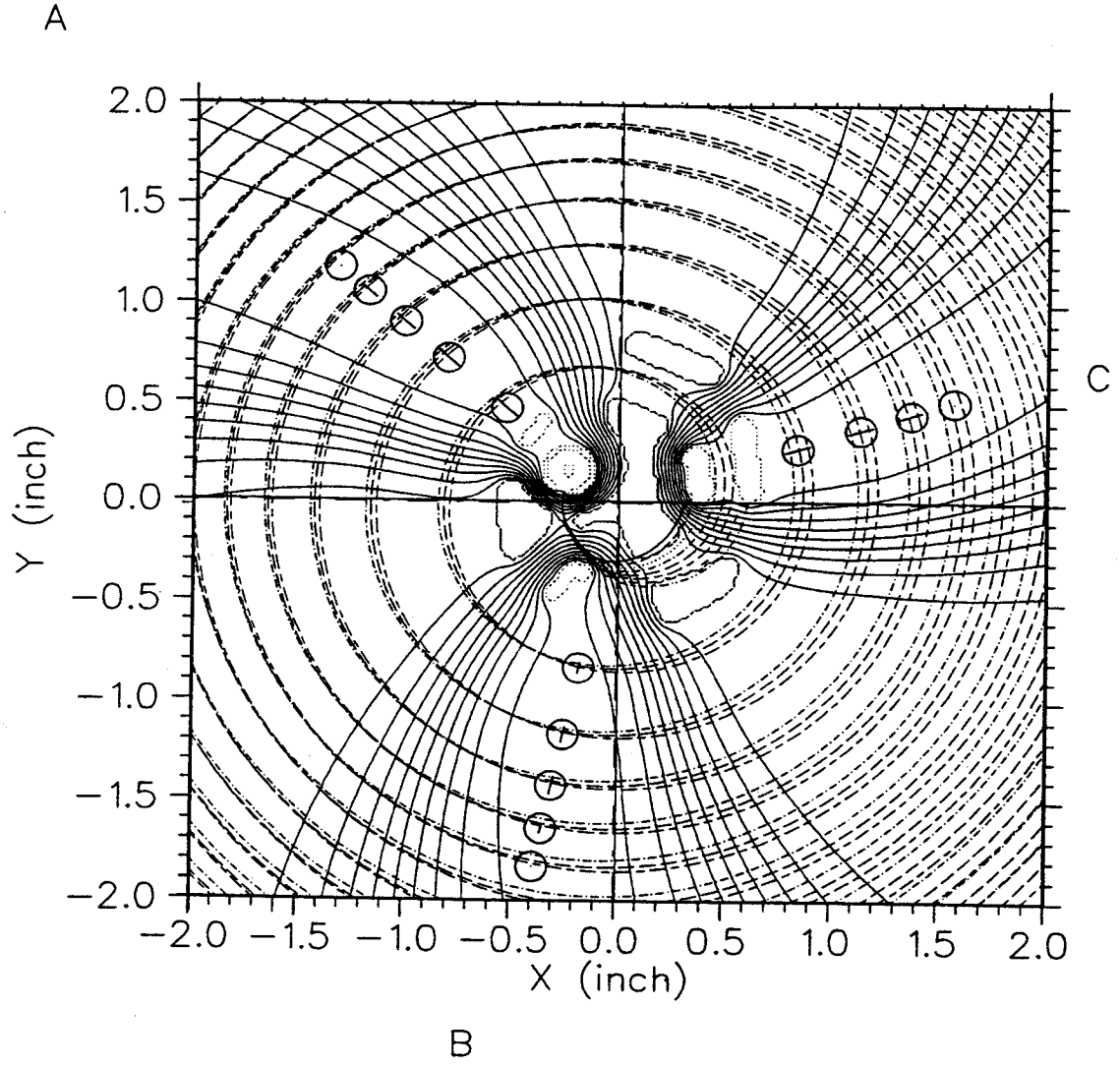

Figure 3.18: Calculated orbits for a starting time of $\tau_o = 243°$ for dee voltages from $V_{dee} = 40$ to 47 kV. Only voltages from $V_{dee} = 43$ to 45 kV clear the posts for this starting time.

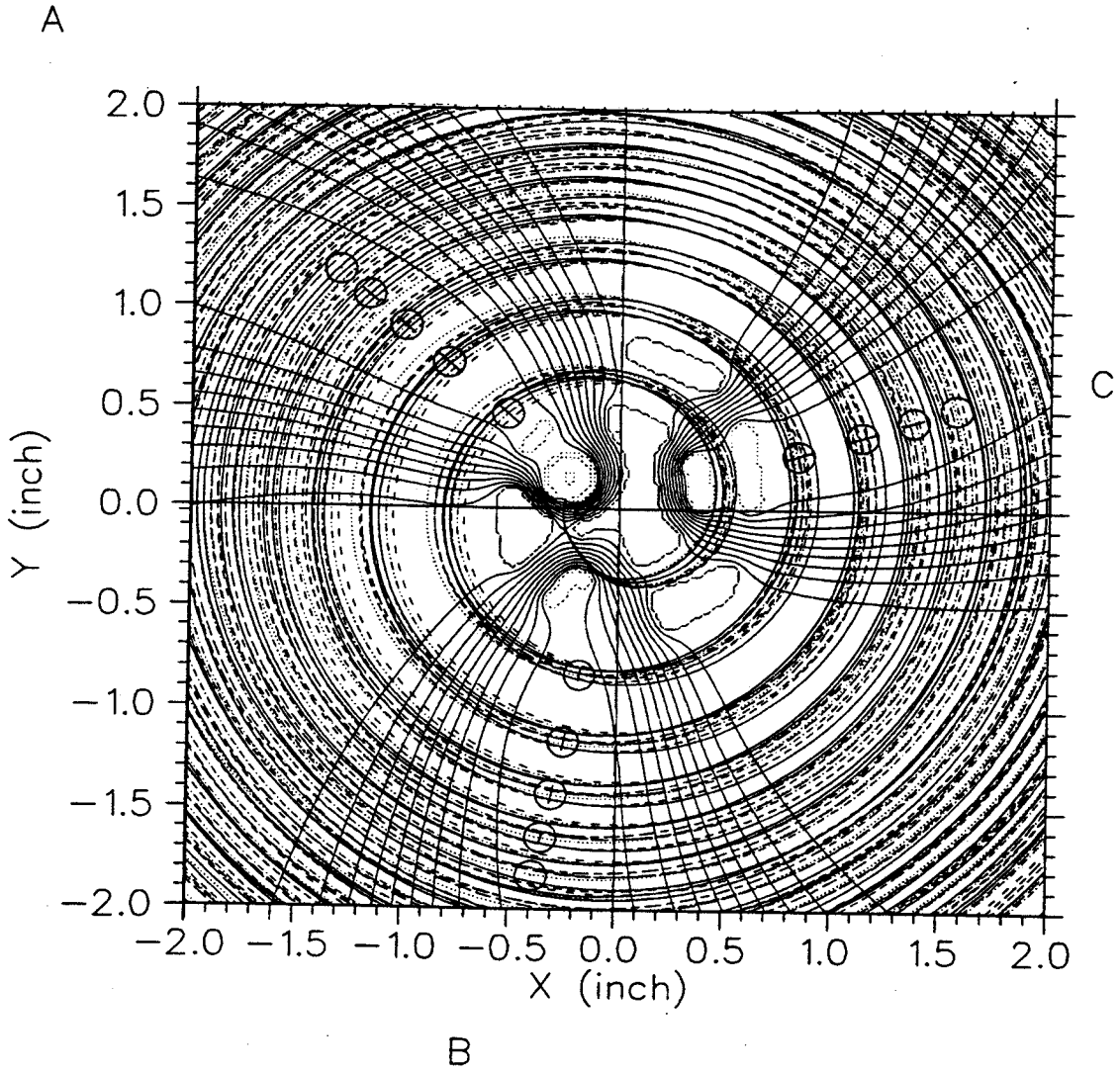

Figure 3.19: Calculated orbits for the range of starting times that clear the central region posts for each of three voltages. Orbits are calculated for $V_{dee} = 47$ kV, $\tau_o = 246.5°, 248.5°, 250.5°$; $V_{dee} = 44$ kV, $\tau_o = 241°, 243°, 245°$; and $V_{dee} = 41$ kV, $\tau_o = 232.5°, 234.5°, 236.5°, 238.5°$.

Chapter 4

HIGH FIELD, ULTRA COMPACT CYCLOTRON FOR NUCLEAR PHYSICS RESEARCH

This chapter examines the feasibility of using an existing 8 tesla magnet as a component of an ultra-high-field cyclotron. General features of the cyclotron are shown in Figure 4.1. Such a machine would use the highest magnetic field of any cyclotron to date, *viz.* 7.6 T averaged azimuthally with 8.5 T in the hills. The K95 'Eight Tesla Cyclotron' would have roughly the same magnetic rigidity ($B\rho$) as the Oak Ridge Isochronous Cyclotron [31] in a package of only one fourth the radius, and one 25th of the weight with a corresponding reduction in cost. Such a cyclotron could accelerate particles with a charge state Q/A = 1/4 to a final energy of 5 to 6 MeV/nucleon, an energy range of much current interest in the study superdeformed, high angular momentum nuclei that result from glancing collisions. Our study of the high field cyclotron has stressed achieving sufficient vertical focusing (ν_z) despite the high magnetic field level, and finding a central region geometry that fits comfortably in the limited space available while providing centering and early-turn focusing properties that are similar to those of less compact machines.

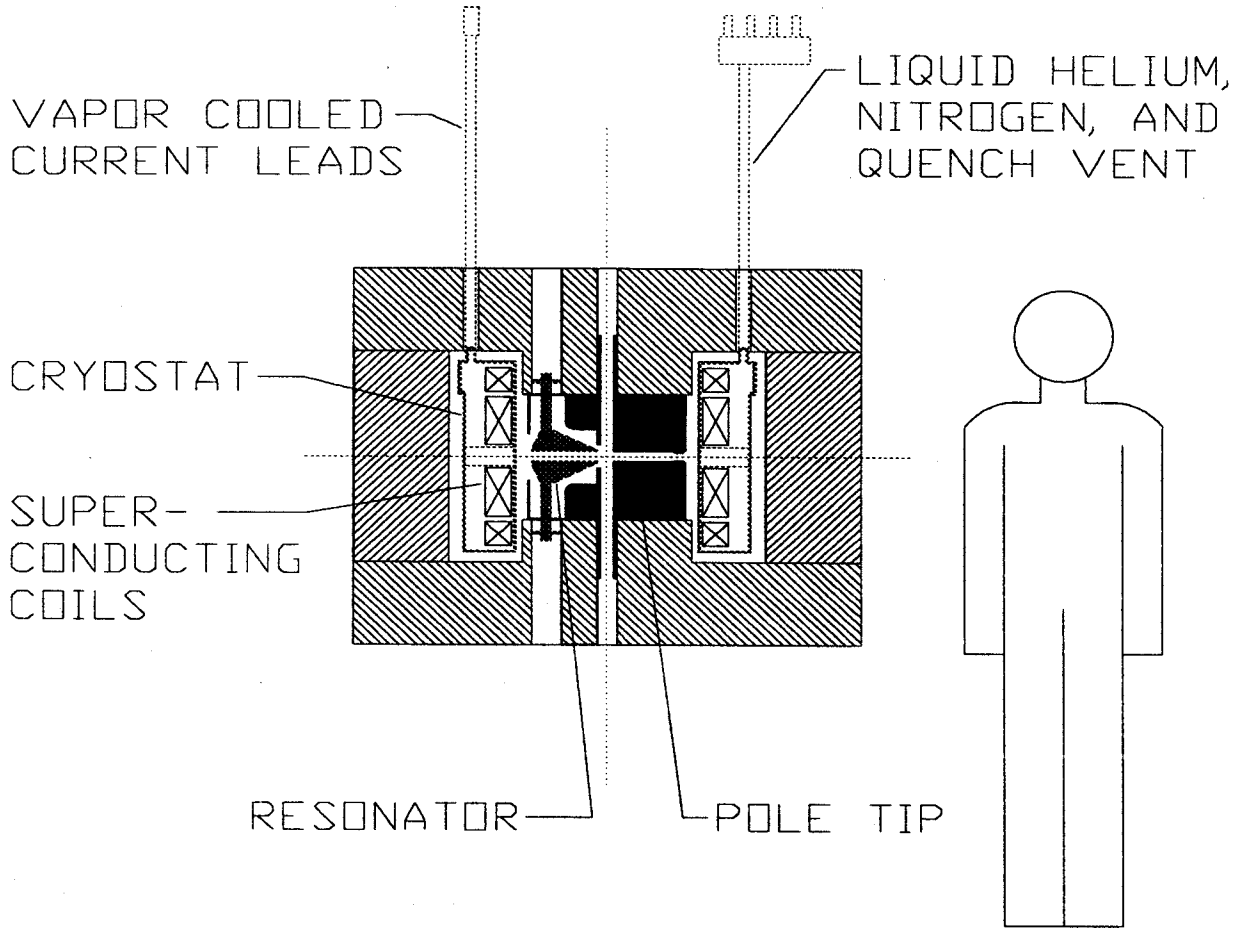

Figure 4.1: Schematic view of the Eight Tesla Cyclotron. The Yoke is 128 cm in diameter and 104 cm in height.

4.1 Overview

4.1.1 Advantages of High Fields

We know from the cyclotron equation (Chapter 2) that the orbital frequency of a particle (of charge to mass ratio q/m) in a classical cyclotron is proportional to the strength of the magnetic field B. It is also understood that the orbital frequency ω of a particle describing a circle is the tangential velocity v divided by the radius of the circle ρ.

$$\omega = qB/m = v/\rho \tag{4.1}$$

$$\rho \propto 1/B \tag{4.2}$$

We see then, that the radius of an orbit of a given rigidity ($B\rho$) in a classical cyclotron is inversely proportional to the magnetic field. A smaller machine results in floor space and material cost savings, with the most important cost reduction being that of the iron for the magnet's yoke.

The practical effect of increasing the magnetic field in a cyclotron can be seen from Figure 4.2, which plots the yoke weight as a function of bending strength for the large cyclotrons of the world, and the proposed Eight Tesla Cyclotron. Looking at the three cyclotrons on the left side of the graph, we see that the Oak Ridge Isochronous Cyclotron (ORIC), the Harper Hospital Medical Cyclotron, and the proposed eight tesla machine all have about the same bending strength, (all are approximately K100) but ORIC has a 2 tesla field and weighs over 200 tonnes. Raising the field up to 8 tesla cuts the weight by more than an order of magnitude.

4.1.2 Design Issues of High Fields

The primary drawback of moving to higher fields is weakening of the axial focusing. As discussed in Chapter 2 the restoring force term in the axial focusing equation

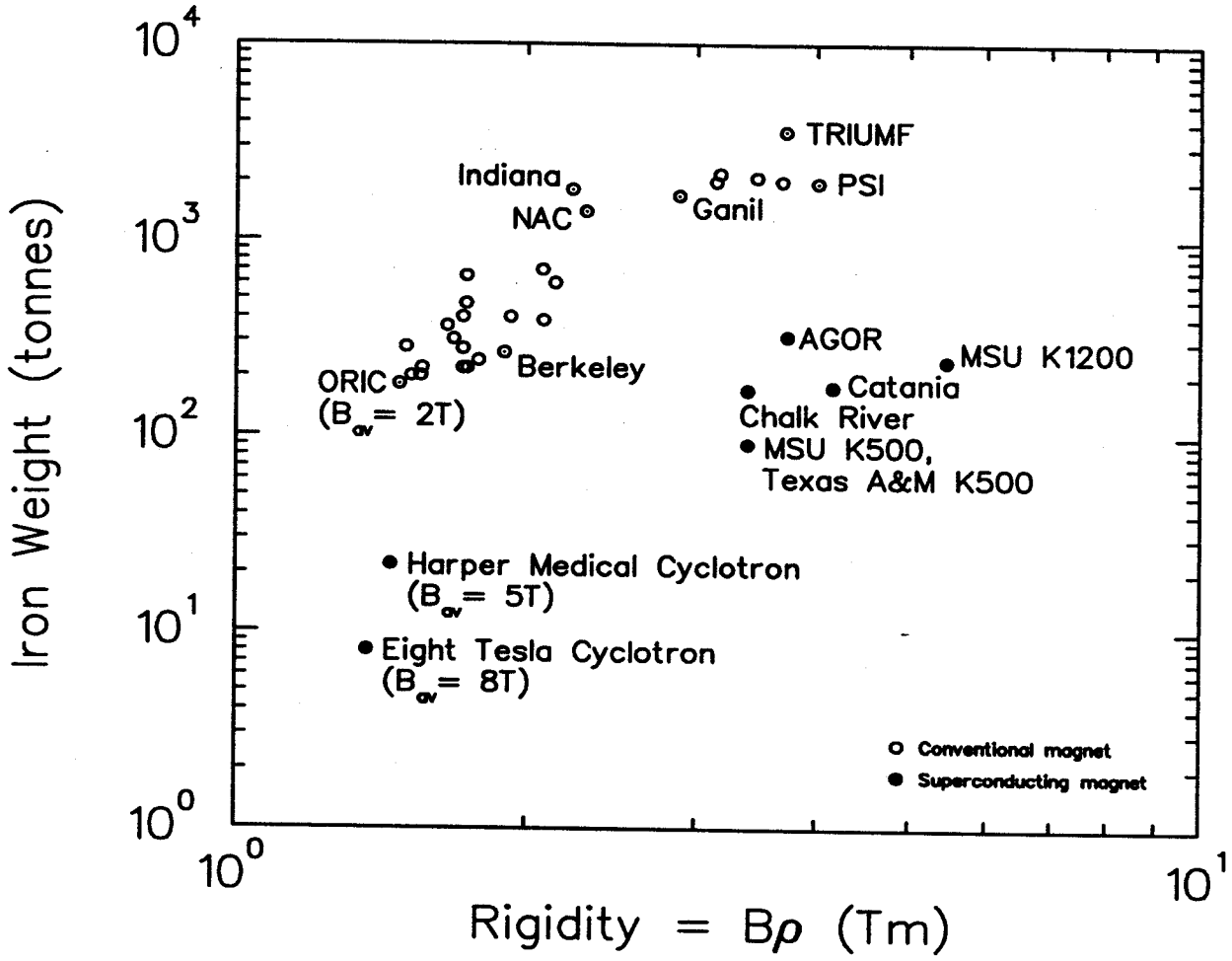

Figure 4.2: Yoke weight as a function of maximum bending power for the large cyclotrons of the world, and the proposed Eight Tesla Cyclotron. The open circles represent normal magnets with typical fields of 1.5 tesla, and the closed circles are superconducting cyclotrons. (Except for the Eight Tesla Cyclotron, superconducting cyclotrons use 4-5 tesla.) A four-fold increase in magnetic field strength from ORIC to the Eight Tesla Cyclotron yields a 25-fold reduction in iron weight.

is proportional to the flutter of the hills and valleys. Once the iron in a cyclotron magnet is saturated, only the geometry of the coils will determine the shape of any additional field produced. Thus the designer can raise the overall field level, but for $B > 2$ T, the difference between the hill and valley fields which give rise to flutter focusing is difficult to increase (unless much more difficult non-circular coils are introduced.) For fields much greater than two tesla, the axial focusing frequency is roughly proportional to the inverse of the field level (using equations 2.7 and 2.9 and assuming a similar spiral and k small compared to F). A ν_z value of .1-.3 is generally accepted as sufficient for most compact cyclotrons [12]. In most larger lower energy machines this level of focusing is easily provided by the poletips.

The non-isochronous field of the central focusing cone (described in Chapter 2) causes the initial phase to shift toward the region of negative phase and negative electrostatic component to the total axial focusing. (This must be offset by using an initial phase which is as strongly positive as the need for first-turn energy gain permits.) In the 4.6 tesla field of the Harper cyclotron the minimum magnetic focusing barely reaches $\nu_z = 0.1$, [17] and orbit simulations that account for electrical effects indicated the existence of a region of defocusing for particles starting as late as $\tau_o = 215°$ [27]. (The beam experiences a phase inversion in the Harper cyclotron central region so ions with later starting times move to earlier phases and visa versa.) If the medical cyclotron's central region and poletips were geometrically scaled to fit into the 8 Tesla Magnet then we would expect a further reduction in the magnetic contribution to the axial betatron frequency ν_z of roughly $B_{Harper}/B_{8Tesla} \approx (5/8)$, while we would not mitigate the electric dofocusing component of ν_z. The Medical Cyclotron was designed to produce a specific current for a specific application and was not optimized further than necessary. In order to build a similar cyclotron in a higher field, however, further optimization is essential. The primary aim of the work

described in this chapter is to develop a design for the magnet poletips and central region electrodes which provides strong axial focusing at all points between the source and the extraction radius.

4.1.3 Goals of the Eight Tesla Cyclotron Project

The Eight Tesla Cyclotron is conceived as a two stage project. The first stage of the project will be to build an internal beam cyclotron to accelerate He^+ from a PIG ion source to an internal beam stop. The design parameters for this stage are listed in Table 4.1. In this configuration the miniature cyclotron would demonstrate the ability of a high field magnet to provide adequate focusing to deliver a beam from the center of the machine to the extraction radius, and the current available for extraction could be measured. At a later time the accelerator is to be converted from a test stand to a nuclear physics tool by replacing the internal ion source with an axial injection system and installing an extraction system. The cyclotron would then accelerate heavy ion beams of any species capable of producing a charge state near Q/A = 1/4. The cyclotron's extracted 6 MeV/nucleon beam would then be delivered to a target at the center of a 4π gamma-ray coincidence detector similar to GAMMASPHERE or EUROGAM [32]. In this chapter, design features of such a cyclotron are developed.

4.2 The Magnetic Field

The Eight Tesla Magnet has been in operation with flat poletips since 1994 [33]. The magnet excitation reported in Table 4.1 was chosen because this is the highest current at which the magnet has operated reliably to date. Further development work on the magnet should make it possible to raise the average field with sectored pole tips to 7.8 T. This would place the third harmonic, Q/A = 1/4, RF frequency comfortably

Table 4.1: Design Parameters of the Internal Beam 8 Tesla Cyclotron.

ORBIT PARAMETERS	
Charge state	0.250
Final energy	5.93 MeV/u
Final radius	18.9 cm
Turn number	175
MAGNET	
Magnet bending limit	95 MeV
Rigidity	1.42 Tm
Ampere-turns	3.1×10^6
Central magnetic field	7.58 T
Maximum hill field	8.47 T
Minimum valley field	6.75 T
Iron weight	8 tons
Pole radius	19.9 cm
Hill gap	2.54 cm
Valley gap	29.8 cm
Sector number	3
Sector spiral	7.46°/cm
Sector width at max radius	62.1°
RF SYSTEM	
Harmonic number	3
RF frequency	87.1 MHz
Peak dee voltage	28.5 kV

inside the FM band, allowing use of a commercially available transmitter intended for FM radio stations, rather than a more expensive custom built transmitter.

The detailed design of the magnetic field is an iterative numerical modeling procedure. Having decided the number of sectors, we guess an initial geometry by scaling from previous cyclotron designs. This guess is then numerically modeled using the 2-dimensional code POISSON [34] to compute the average field and a set of 3-dimensional codes written at the NSCL to model the flutter produced by the iron pole pieces assuming full saturation in the z direction. The field is then analyzed

using orbit tracking codes. Iron is added or removed from the valley floors in order to obtain the desired azimuthal average field $\langle B \rangle$ at each radius, while keeping the valleys sufficiently deep to provide flutter for axial focusing. The spiral of the hills is simultaneously adjusted. Although increasing the spiral increases ν_z, it also reduces the perpendicular distance between hills. At some point the hills become too close washing out the flutter, and the reduction in flutter eliminates any further gains from the increase in spiral. After each change the magnetic field, and the associated phase and focusing curves are recalculated.

A non-isochronous field cone is included to provide magnetic focusing for the first five or so turns in the central region where the flutter is negligible. While providing magnetic focusing the cone drives the beam's phase toward negative (earlier) values which reduce electric focusing and may cause electric defocusing. At first the size of the cone is based on a guess or scaled from other cyclotron designs. The entire process is then revisited during the design of the central region so that the effect of electric focusing can be folded into the magnetic field design and the size of the central focusing cone can be optimized.

The final design of the iron poletips is shown in figures 4.3 and 4.4. The poletips are small enough to permit machining sectors out of a single piece of iron for each pole. Unlike the three previous superconducting cyclotrons built at the NSCL, this design includes iron in the ion source. The iron was needed because we wished to use an NSCL standard 1.375" diameter ion source. Increasing the field of the cyclotron causes all of the particle orbits to shrink. As the radius of the first turn shrinks, but the central hole in the yoke does not, the depression in the center of the magnetic field, caused by the hole, becomes more serious. We attempted to compensate for the hole with careful design of the center plug, but in the end it was necessary to incorporate iron into the ion source itself. Although this complicates the ion source

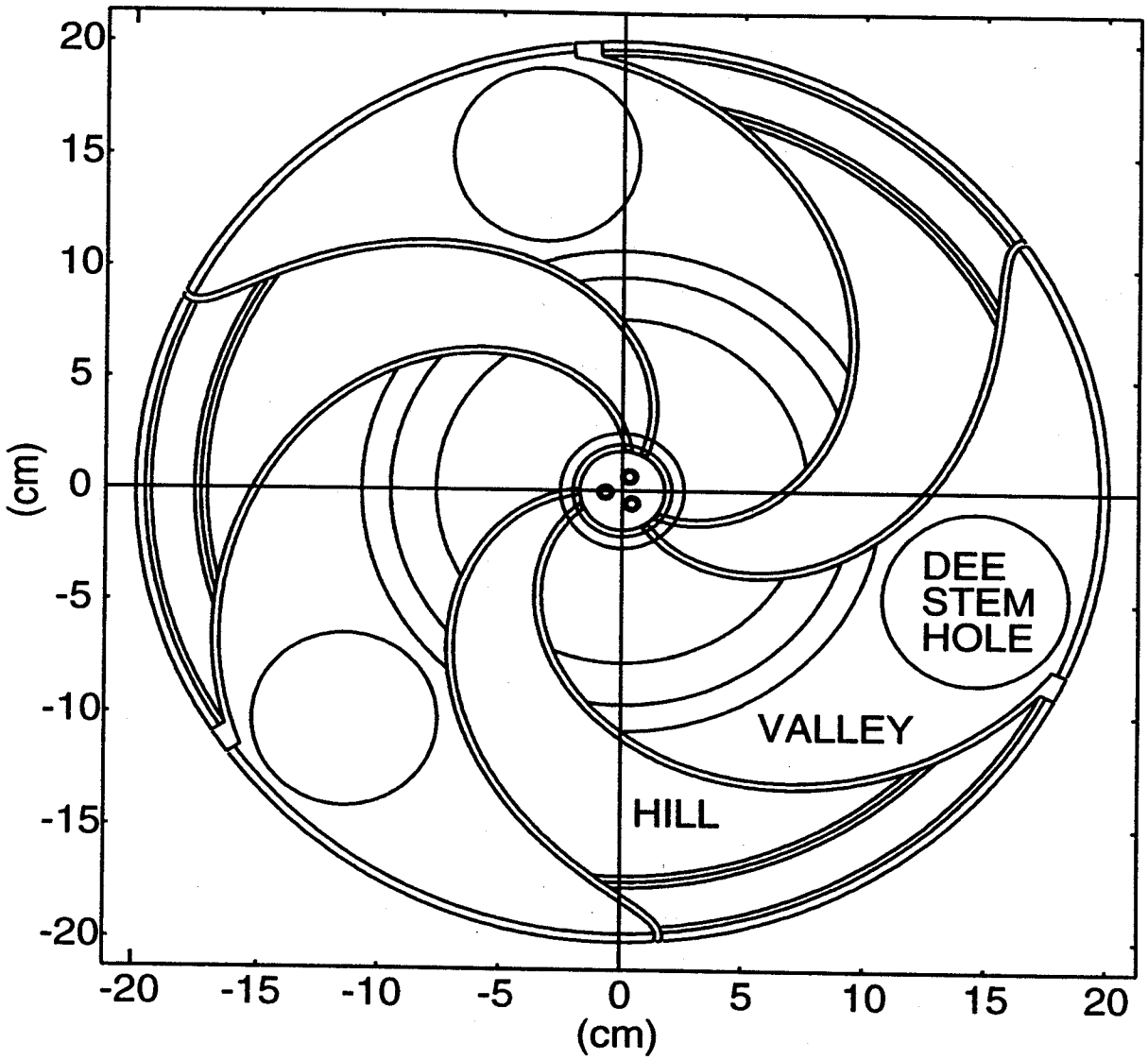

Figure 4.3: Median plane view of the pole tip geometry used to calculate the midplane magnetic field. (Double lines represent steps used to simulate the effect of smooth chamfers on the edges of the hills.)

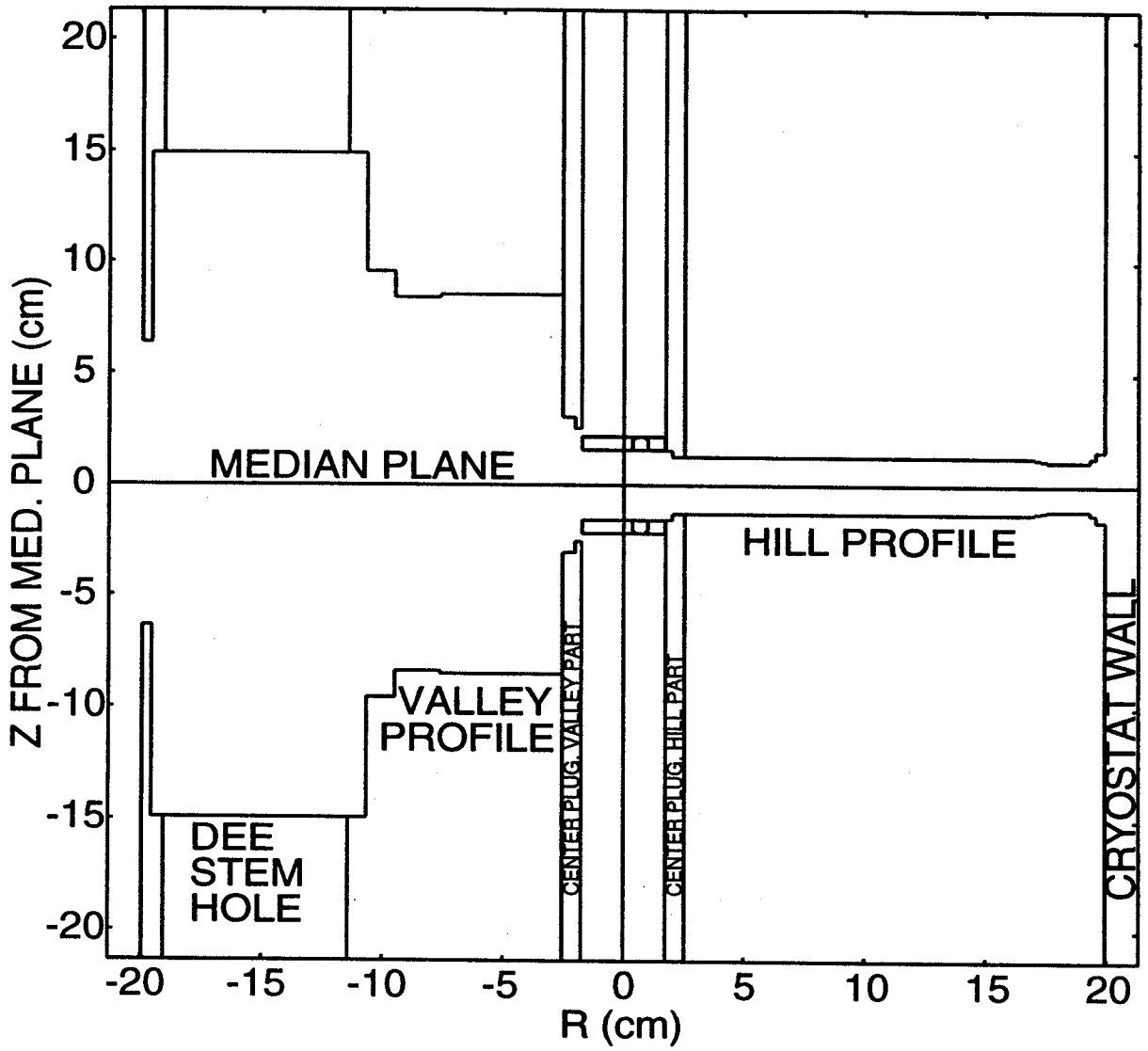

Figure 4.4: Radial profile of the pole tip geometry. Chamfers on the hill edges ($r = 0.25$".) and on the inner valley shim ($r = 1.0$") have been approximated by steps which remove the same amount of iron as the actual chamfer. Iron will be incorporated into the ion source (as shown here) or spiral inflector to shape the magnetic field in the central region.

Figure 4.5: Contour plot of the median plane magnetic field. Contour spacing is two kilogauss with the dotted contour at 6.8 T and the double weight contour over each hill at 8.4 T.

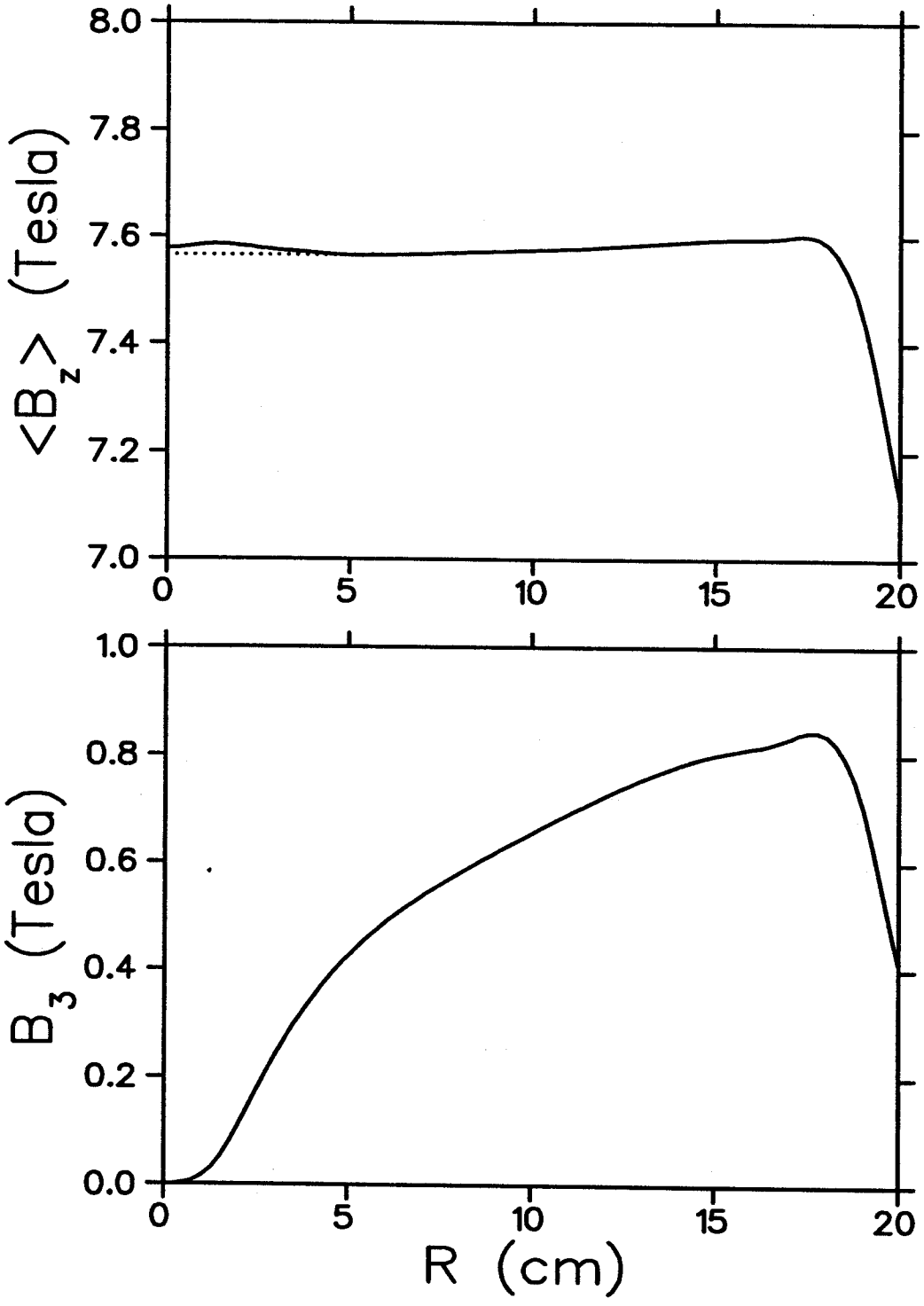

Figure 4.6: Top: the azimuthal average of the axial component of the calculated median plane field (solid line) and a perfectly isochronous field (dotted line.) Bottom: the third harmonic component of B_z that mainly gives rise to 'flutter' focusing. The 'central focusing cone' (apparent in the top graph) is used to enhance focusing of the early turns, before the flutter rises to a high enough value.

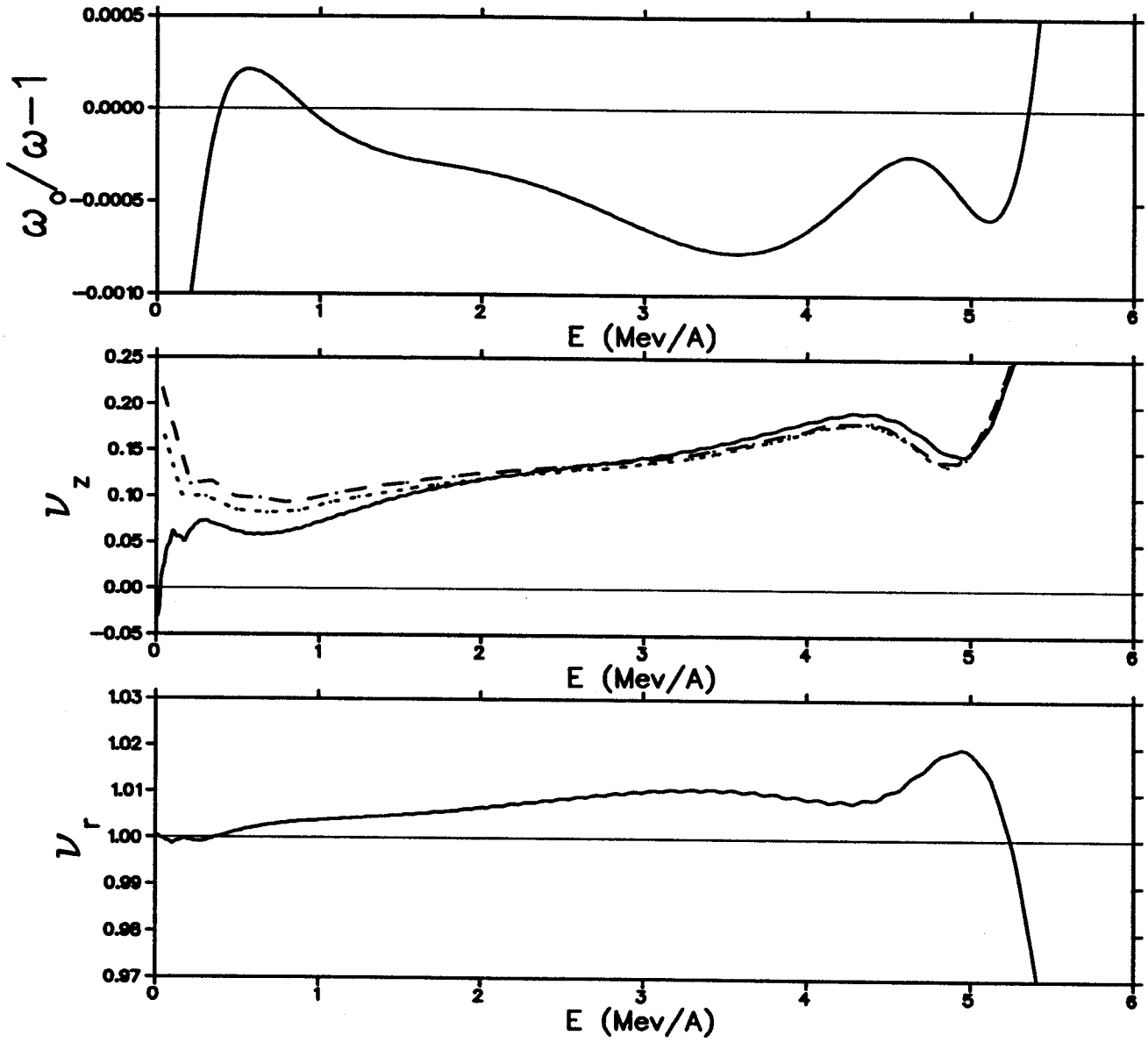

Figure 4.7: Equilibrium orbit properties as a function of energy calculated by the NSCL equilibrium orbit code. Top: orbital frequency relative to isochronous frequency. Middle and Bottom: axial and radial focusing frequencies. Also plotted are the total axial focusing frequencies for accelerated orbits leaving the ion source at RF times $\tau_o = 207°$ (dashed line) and 201° (dotted line.) Peak dee voltage occurs at $\tau = 270°$.

design considerably, it fills in the field hole adequately and makes the shaping of the central field cone much easier. Because this is a fixed energy single charge state machine we may accomplish all other needed field shaping with hill and valley shims so no trim coils are needed.

The resulting calculated magnetic field is shown in figures 4.5 and 4.6. The fields are first analyzed with 'equilibrium orbit tracking codes.' The 'equilibrium orbits' are smoothly closed coasting orbits for a set of particles with an array of starting energies and for each energy the code searches for the radius and direction which gives the smoothly closed orbit for that energy. The NSCL's 'EO codes' use an iterative search algorithm to find one such orbit for each specified energy, and then test these orbits to determine the focusing properties of the magnetic field as a function of energy. The 'equilibrium orbit properties' for this field are shown in Figure 4.7.

As stated in section 4.1.2, raising the overall field level $\langle B \rangle$ beyond saturation has little effect on the variation between the hill and valley fields. For this cyclotron the third harmonic component B_3 of the midplane field $B_z(r, \theta)$ peaks at 8 kG (Figure 4.6) which is almost identical to the case for the 4.6 T Harper medical cyclotron. Flutter focusing depends on the ratio of $B_3/\langle B \rangle$, so the higher the field, the smaller the contribution of flutter focusing to the total ν_z. Although the flutter component of ν_z is sufficient at middle energies, it rises slowly near the center so the central focusing cone and electrostatic focusing are more important to the early turns in the high field machine than in its low field predecessors.

4.3 The Central Region

Central regions for multiple species cyclotrons can be designed by scaling from a previous well-behaved central region using the Reiser parameter, χ, which gives dee

voltages and/or field levels to guide different nonrelativistic particles through the same central region geometry [35].

$$\chi = \frac{l_1^2 B_1^2 (Q/A)_1}{V_1} = \frac{l_2^2 B_2^2 (Q/A)_2}{V_2} = constant, \tag{4.3}$$

where B is the magnetic field strength at a reference point, Q/A the charge state in units of e/m_0, V the peak dee voltage, and l a reference length, usually the dee gap, relating the scaling of the central electrode system. The subscript 1 refers to the reference particle and 2 refers to any other particle. The relationship may be used to expand or reduce the central region from one machine to work for a different particle in the same or a different machine. For two given particles, magnetic fields, and dee voltages, the orbits and electrodes in system 2 will be a photographic enlargement of system 1 by a scale of $l_2 : l_1$.

The central region for the 8 Tesla Cyclotron was initially scaled from that of the Harper Medical Cyclotron [36] which accelerates deuterons ($Q/A = \frac{1}{2}$) in a central field of 4.6 T. The Harper geometry is reduced by a factor of 0.80 to run ions with a charge state of $Q/A = \frac{1}{4}$ in the higher magnetic field while reducing the dee voltage so that the risk of sparking will not be increased in the reduced source-to-puller gap. The scaled dee voltage of 28.5 kV is used for all of the calculations presented in this chapter.

Electric fields in the central region are computed by RELAX3D [26] and then orbits are tracked by the NSCL code, CYCLONE [16]. Initial conditions for orbit simulations were chosen by running a variety of orbits in the scaled central region. Particles that left the chimney at an RF time $\tau_o = 204°$ were found to be the best centered (relative to other starting times) and since experimental data was not available at the time, these orbits were presumed to best characterize the beam in the actual Harper cyclotron.

The scaled geometry was then modified to further optimize beam centering in preparation for extraction studies. A post was added to eliminate the phase inversion and the design was also modified to compensate for the magnetic focusing that is lost due to the higher field. The optimized central region layout is shown in Figure 4.8 and the resulting electric field is plotted in Figure 4.9. The first accelerating gap (from the chimney to the field free region at the center of the puller) has been shifted 4° clockwise by the orbit code to simulate lengthening the puller gap in order to shift all phases in the positive direction. Particles spend more time drifting through the lengthened puller and so are delivered to the rest of the machine at a later time to improve electric focusing [10]. Figure 4.10 shows the average phase per turn calculated from the time that a particle arrives at the electrical center of each gap.

The first gap position and cone field size have been chosen to keep the average phase near +30° for the first 1 MeV/u of acceleration (about 30 turns) in order to maximize electrostatic axial focusing in the region where the magnetic contribution to ν_z is below 0.1. The axial motion itself of these rays and corresponding rays with linearly independent displacements is plotted in Figure 4.11. (The total focusing plotted in Figure 4.7 is measured from half cycles of vertical oscillations of a ray that is displaced 2 mm vertically at the puller and then accelerated to full energy.)

Axial and radial confinement were investigated for starting times from $\tau_o = 201°$ to 207°. We are interested in the area occupied by the beam in a 2 dimensional spot-size divergence space, known as the 'emittance.' The maximum emittance that can be accelerated from a given point to the target or extraction channel is known as the 'acceptance.' To measure the acceptance we create sets of rays displaced from the central ray at the puller and accelerate these rays until they are either lost or they reach the outer radius of the machine. The maximum displacements in axial position and momentum (at the puller) which remain within the beam aperture approximate

an ellipse in z-p_z phase space corresponding to a total normalized acceptance of 1.0πmm-mrad for the range of starting times studied. Similar studies of orbits that are displaced radially at the puller indicate a normalized radial acceptance of at least 0.15π mm-mrad for the same range of starting times.

4.4 Feasibility of Axial Injection

In order to produce Q/A = 1/4 heavy ion beams of $\mathcal{A}$(40 (for nuclear physics experiments) the cyclotron would need an external ion source and an axial injection system. A spiral inflector geometry can be scaled from the design used in the K500 and K1200 cyclotrons [37] by holding the parameter $K = \mathcal{A}/2R_m$ constant, where $\mathcal{A}$ is the inflector's electric radius of curvature (and the height of the inflector) and R_m is the magnetic radius of curvature in the center of the cyclotron [38]. The K1200 runs He^+ ions in a 3.54 T field. The height and width of the inflector are inversely proportional to the magnetic field, so the dimensions of the inflector will by scaled by a factor of $\frac{B_{K1200}}{B_{8TCyclotron}} = 0.468$, resulting in an inflector which is 0.81 cm tall with a 2 mm gap.

If a new central region were scaled from the K1200 [39] using the same method as in the previous section, then the scale factor would be 0.408. The scaled inflector is too large to perfectly match the scaled central region, but the discrepancy is only 15% so the needed adjustments should be minor.

The electric field in the inflector gap increases in proportion to the magnetic field. Our field is more than double the K1200's, so we would have to increase the gap electric field from 11 kV/cm to 24 kV/cm, which is still comfortably within the operating range of such devices.

The primary difficulty appears to be machining and properly positioning the

'miniature' inflector electrodes. More detailed studies may be necessary to investigate increasing the gap height and the corresponding electrode voltage.

4.5 Feasibility of Extraction

We plan a resonant extraction system similar to the ones in use in the K500 and K1200 cyclotrons [40]. In this system a first harmonic perturbation in the magnetic field interacts with the $\nu_r = 1$ resonance at the edge of the field to drive the beam off center and increase the turn spacing at a particular azimuth. This azimuth is then used to locate the entrance to the electrostatic deflector which peels the final turn away from rest of the internal orbits.

The magnetic field bump would be produced by a set of iron rods (1" in diameter) similar to the Chalk River trim rods [41]. The rods eliminate all space and cooling issues associated with trim coils and they can be centered at the radius where $\nu_r = 1$, so that only a small displacement is needed to produce a sufficient first harmonic.

The turn separation produced by a $B_1 = 5$ gauss field perturbation can be seen in Figure 4.12. Here the $\tau_o = 204°$ central ray from the internal ion source central region has been tracked from the source ($E_o = 10$eV/u) to the likely position of an electrostatic extraction channel. The septum would be located near a radius of 18.5 cm. A phase space is defined by eight rays displaced in r or p_r from the central ray at the puller to form a 1 mm diameter circle in r-p_r phase space. Each of the eight rays' phase ϕ (at the puller) has been adjusted so that its energy gain (and phase averaged over one turn) is similar to that of the central ray by the 33rd turn ($E = 1$ MeV/u). The first harmonic perturbation causes little distortion of the phase space while providing a turn-center to turn-center separation of 2 mm.

The low first harmonic used for the initial off-centering helps to minimize the axial

expansion of the beam which occurs at the $\nu_r = 2\nu_z$ resonance roughly ten turns after the $\nu_r = 1$, resonance. A beam which fills the 7.5 mm puller aperture has a height of roughly 5 mm at the entrance to the electrostatic deflector. A corresponding axial phase space distribution is tracked from 16 cm to extraction in Figure 4.14.

From this point a pair of 56° long electrostatic deflectors in successive hills, followed by a 64° electrostatic deflector located behind a dee, can extract the beam with an electric field of 130 kV/cm in a gap 2.5-3.5 mm wide, which is within the range of electric fields used successfully at the NSCL [42]. The conceptual layout of the extraction system and one primary ray orbit is shown in Figure 4.14.

4.6 Conclusion

The miniaturization of cyclotron components for an 8 tesla magnetic field poses no critical problems for the energy and charge-to-mass ratio studied. Such a machine would be a natural extension of the development work already performed at the NSCL on super-conducting cyclotrons.

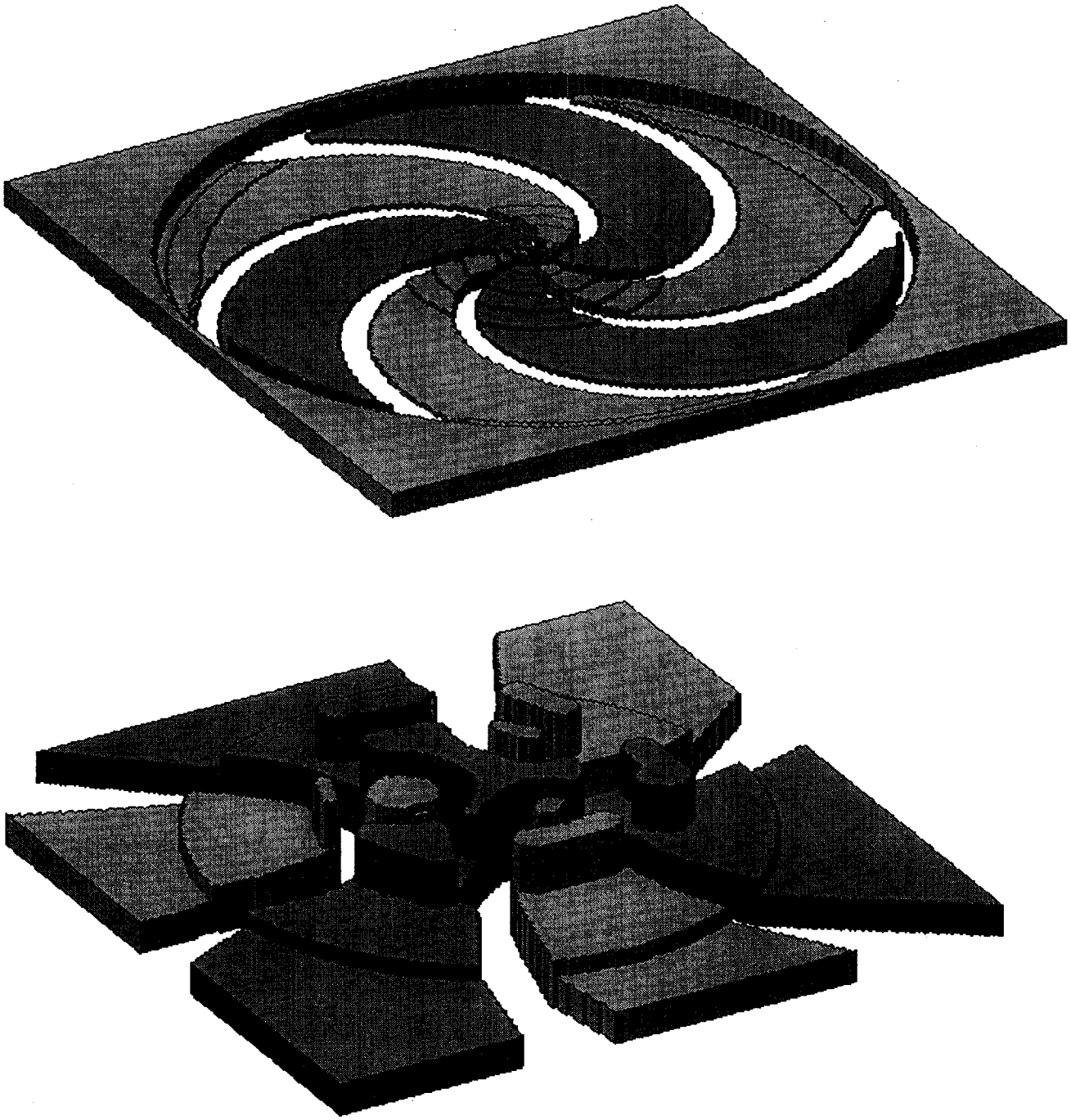

Figure 4.8: Bottom: lower half of the central region electrodes, sliced at the median plane. The lighter color is ground potential; the darker color is dee potential. The electrode area is 2×2 inches. Top: Electrode model used to calculate electric fields beyond the central region. Electrode area is 16×16 inches.

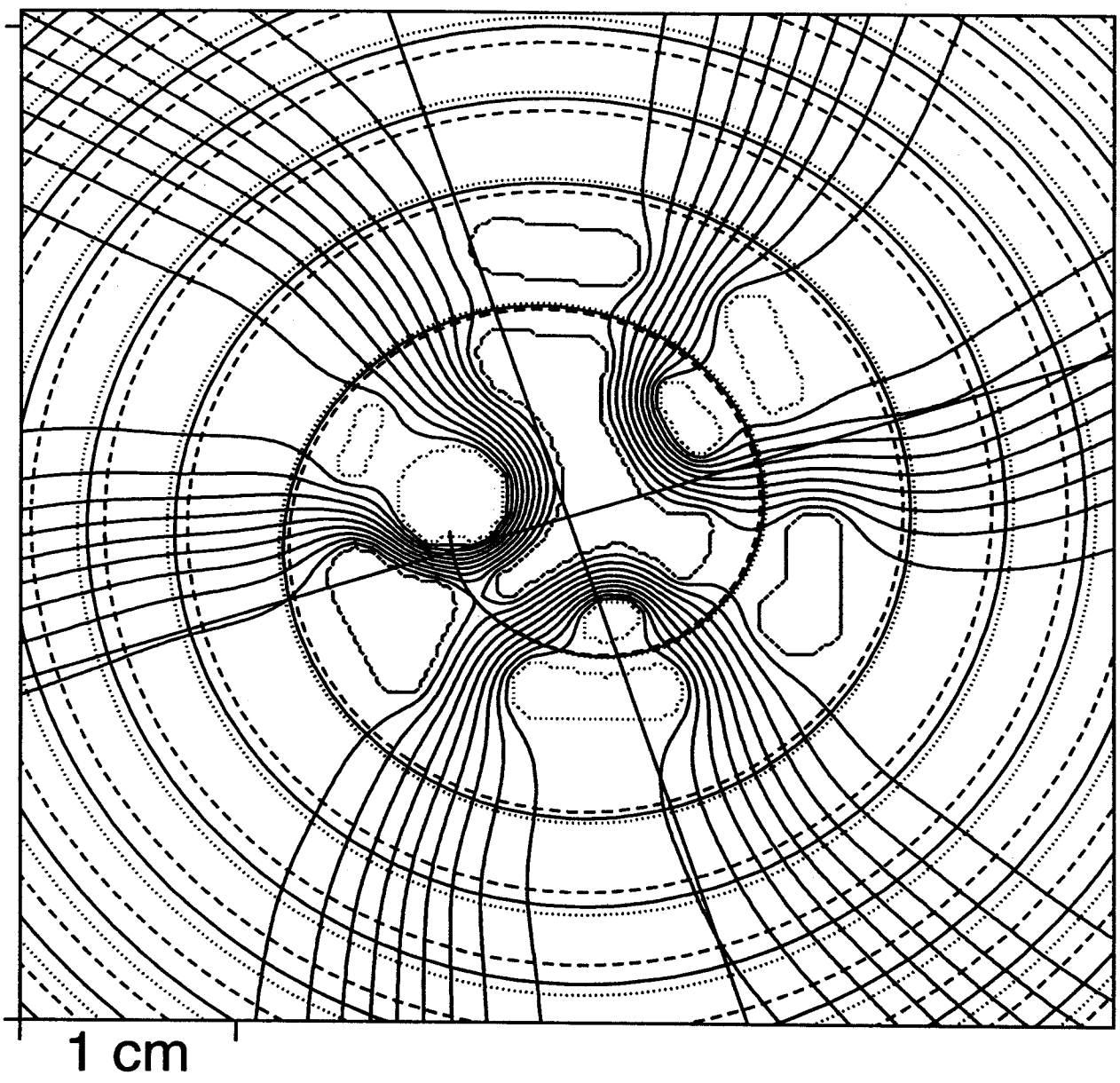

Figure 4.9: Equipotential field map (produced by RELAX3D) and the first few orbits for beam leaving the ion source at RF times $\tau_o = 201°$ (dotted line), 204° (solid line) and 207° (dashed line).

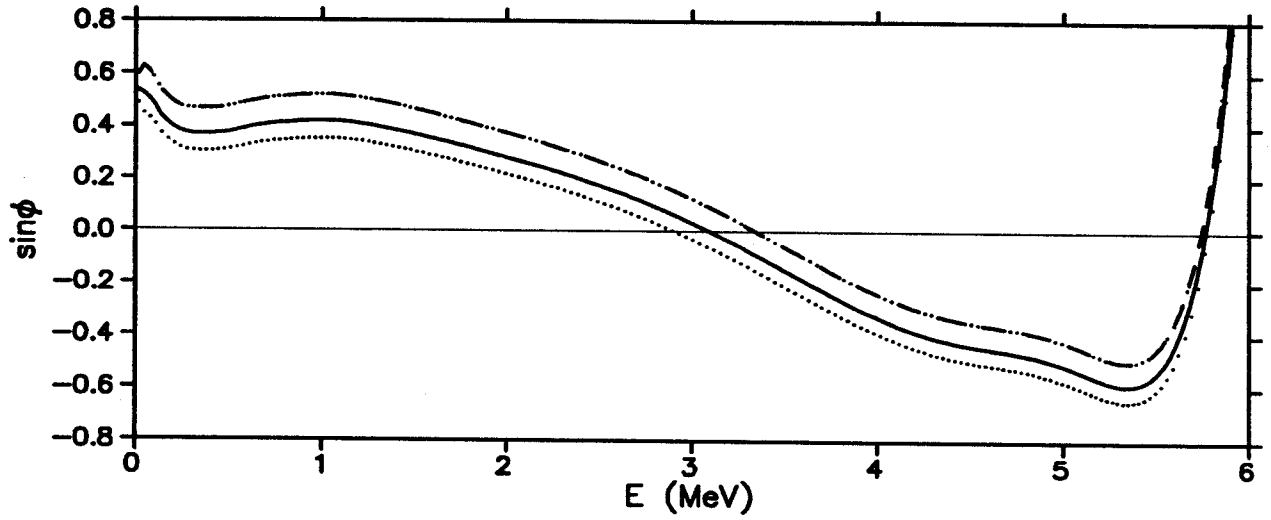

Figure 4.10: Turn average phase for the three accelerated orbits leaving the chimney at RF times $\tau_o = 207°$ (dashed line), $\tau_o = 204°$ (solid line) and 201° (dotted line.) Peak dee voltage occurs at $\tau = 270°$.

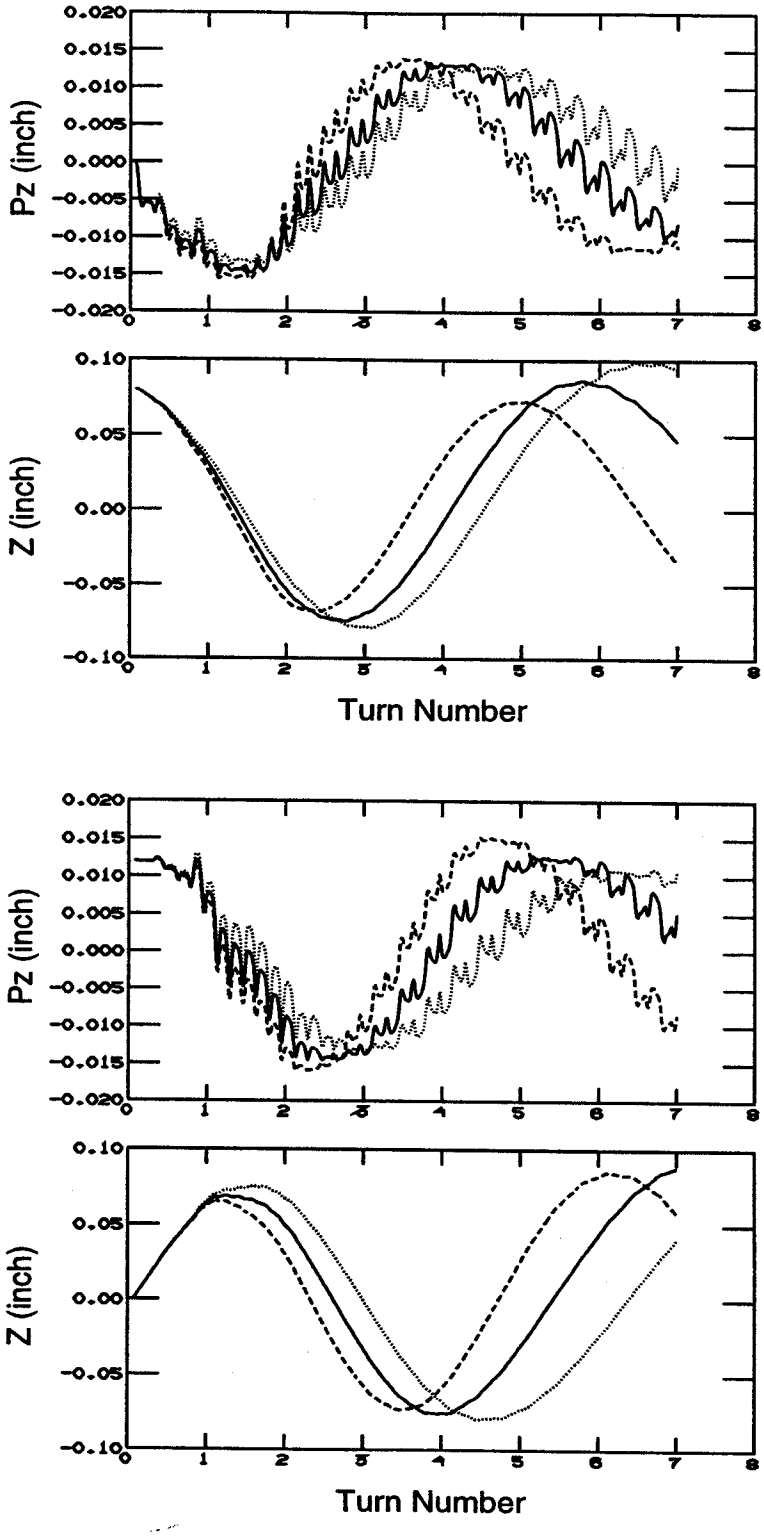

Figure 4.11: Axial motion for the same three rays as in the previous two figures. Each ray is displaced in z (top two graphs) or p_z (bottom two graphs) at the puller.

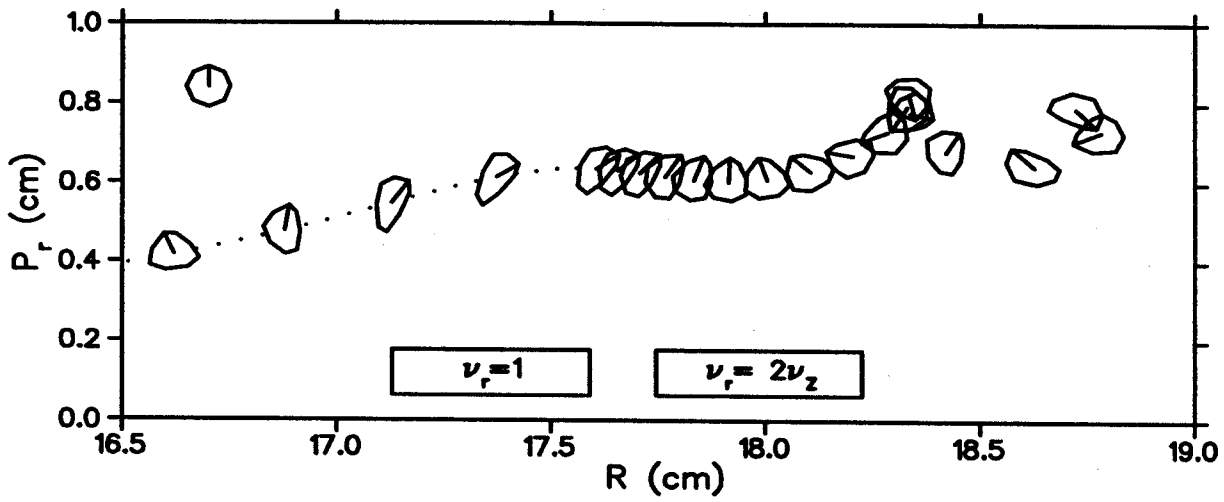

Figure 4.12: Radial phase space behavior of a family of accelerated rays plotted at the azimuth of the electrostatic deflector entrance. Each of eight rays is displaced 0.5 mm in $r - p_r$ phase space from the $\tau_o = 204°$ central ray at the puller. (The shape of the initial phase space (at the puller) relative to the central ray is indicated at the upper left.) The entire family of nine rays is then accelerated to maximum energy. Separation between turns N = 175 and N = 176 is produced by a 5 gauss first harmonic magnetic field perturbation located at an azimuth of $\theta_{B_1} = 347.5°$ at the radius where $\nu_r = 1$. (Radial momentum p_r is divided by $\omega_o m$ to yield units in cm.)

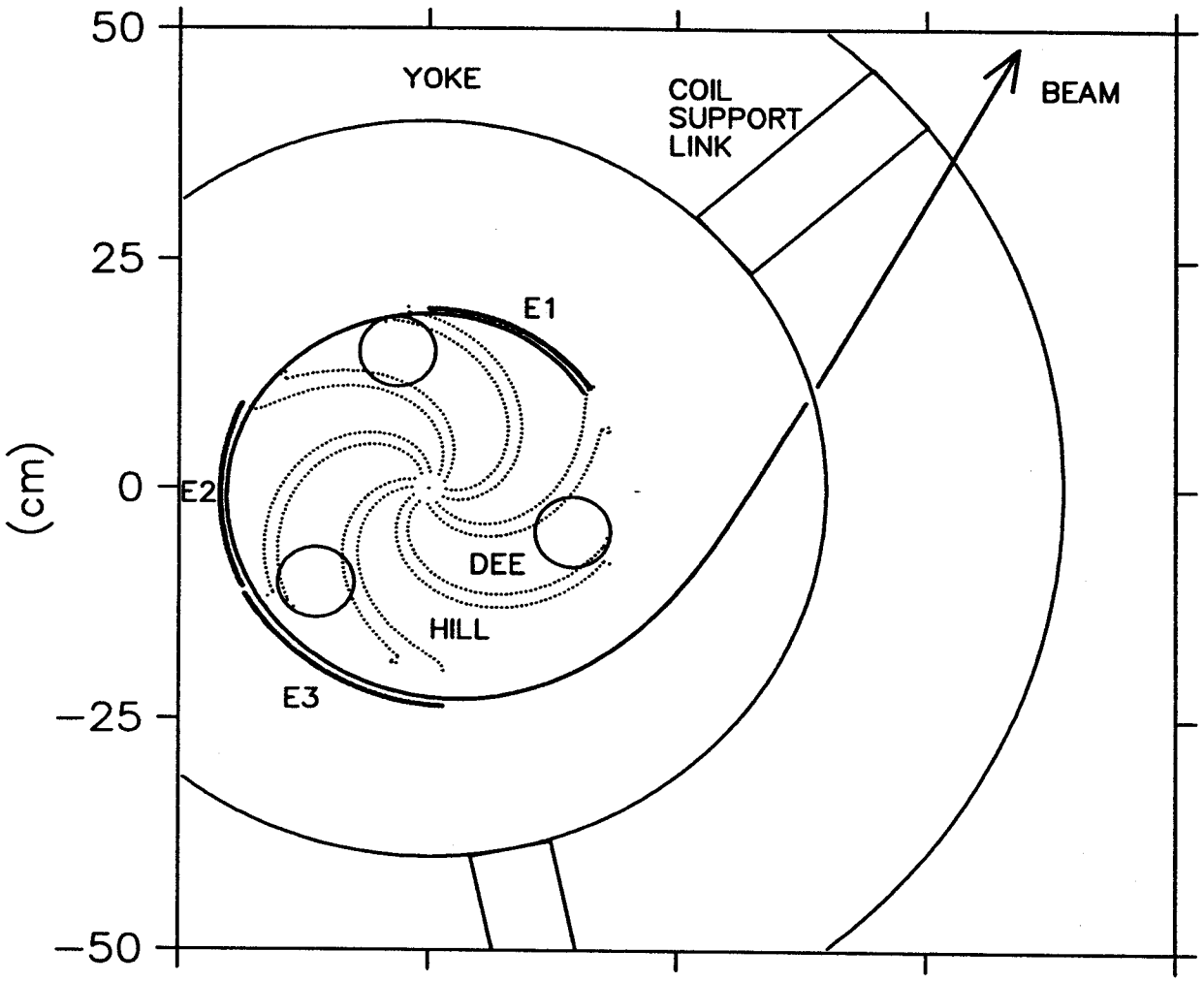

Figure 4.13: Plan of the extraction system. Each of the three electrostatic deflectors (labeled 'E1,' 'E2,' and 'E3') uses a 130 kV/cm field in a 2.5-3.5 mm wide gap.

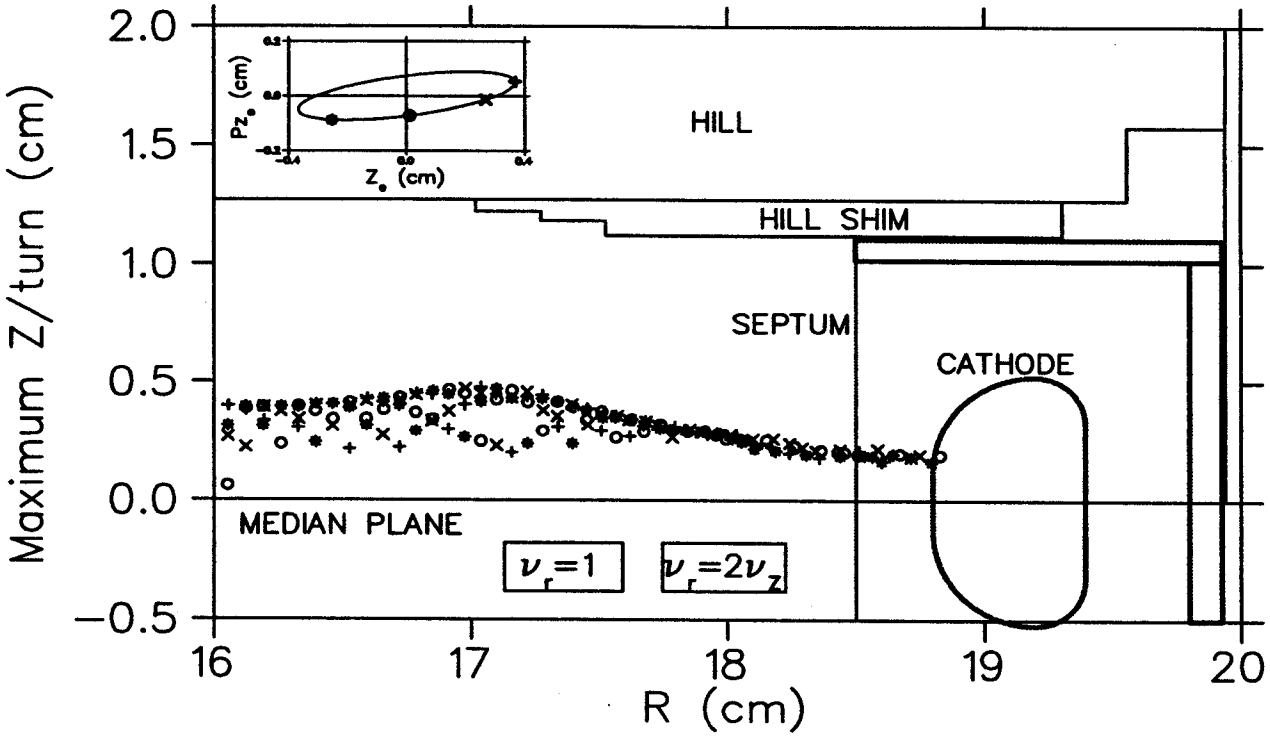

Figure 4.14: Axial envelope of the beam near extraction, and a possible deflector geometry. the maximum z value of each of four rays is plotted for each turn. Inset shows the axial phase space of four rays at $r = 16$cm. (Axial momentum p_z is divided by $\omega_o m$ to yield units in cm.)

Chapter 5

HIGH RESOLUTION CYCLOTRON FOR ACCELERATOR MASS SPECTROMETRY

Accelerator mass spectrometry (AMS), used as method of determining the abundance of radioisotopes, is approximately 1000 times more sensitive than traditional decay counting [43]. Since the introduction of AMS in 1977 many electrostatic accelerators have been converted into ^{14}C measuring devices for archeological and biomedical research. With AMS, accurate ages of artifacts may be obtained with as little as a milligram of carbon. The reduced sample size is of great value to archaeologists as well as art historians who must destroy part of an artifact in order to extract enough carbon to date it. More recently AMS has been investigated as a tool for detecting radioisotopes that are used as tracers in biomedical experiments. As in archeology, the 1000 fold increase in sensitivity has driven rapid development of this new industry. The Center for Accelerator Mass Spectrometry (CAMS) at Lawrence Livermore runs over 10,000 samples a year using 8 different isotopes. 80% of the AMS work at LLNL involves measuring ^{14}C at abundances of 10^{-12}–10^{-15} relative to ^{12}C [44].

CAMS and most other commercial AMS laboratories use electrostatic tandem

Van de Graaff accelerators with energies of at least 1 MeV, which require terminal voltages of at least 500 kV. After acceleration in the tandem the various components of the high energy beam are separated in a magnetic dipole spectrometer. The large size and cost of tandem accelerator systems has motivated a few groups to study the possibility of a cyclotron-based AMS system which should be much smaller and cheaper for a given resolution. Because the cyclotron automatically selects one charge to mass ratio (Q/A) to accelerate, the acceleration and mass-separation are performed in a single step. Cyclotrons are also capable of isolating ^{14}C in beams with energies as low as 50 keV/ion, [55] which reduces the voltage required by at least three orders of magnitude (see Table 5.1) relative to tandem-based AMS.

In late 1995 the NSCL began to investigate the possibility of building a minicyclotron for ^{14}C measurements. Since a magnet with sectored poletips was available in the lab (originally an energy analysing magnet of the K50 with poletips left over from a terminated contraband detection study) this magnet became the starting point of the feasibility study.

5.1 Principle of Operation

The resonance condition for an isochronous cyclotron tells us that for a given magnetic field, B, and particle frequency, $f_p = \frac{1}{2\pi}\frac{qB}{m_o}$, only ions of one charge to mass ratio, q/m_o, may accelerate without experiencing a phase change, $\Delta\phi$. Non-resonant background particles (e.g. species with the same charge but a different mass, m) will experience phase-slip proportional to their mass difference, $\Delta m \equiv m_o - m$. Once a particle slips more than 90° out of phase it is decelerated back toward the center of the machine and lost. The AMS cyclotron, then, relies on a large number of turns to allow the phase-slip of background particles to accumulate and/or a high harmonic

($h = \frac{f_{RF}}{f_p}$, where f_{RF} is the RF frequency) to maximize the phase-slip/turn.

5.1.1 Calculating the Resolution of a Cyclotron Mass Spectrometer

The resolution of the cyclotron mass spectrometer is defined as the inverse of the mass difference required to shift a background particle from $\sin\phi = 1$ to $\sin\phi = -1$, which would insure that background particles of any possible starting phase will cease to accelerate. An approximate expression for the resolution R is derived by Clark [45].

$$R \equiv m/\Delta m = \pi N_o h$$

where N_o is the number of turns an in-phase particle would experience. The finite phase width of the injected beam reduces the resolution [45] so the above formula is typically rounded down to

$$R \approx 3N_o h \tag{5.1}$$

for initial calculations of machine parameters [46, 47, 48].

To separate $^{14}C^+$ from $^{14}N^+$ the spectrometer would need a resolution of 83,000 [49]. Nitrogen, however, does not form a stable negative ion and can therefore be eliminated by using a negative ion source, such as a Cs-sputter source to produce $^{14}C^-$. To separate $^{14}C^-$ from its nearest molecular isobar, $^{12}CH_2^-$, requires a resolution of only 1800.

A cyclotron operating in 3rd harmonic mode would require approximately 200 turns to isolate $^{14}C^-$. Conversely, a 50 turn cyclotron could achieve the same resolution if it were operated at 12th harmonic. The final energy of the beam is only relevant to the problem of detection. A large energy gain per turn, E_t is only desirable to facilitate injection and extraction of the beam. Otherwise a low value of E_t, and hence, a low dee voltage is desired in order to maximize the turn number. The

maximum resolution of a given cyclotron is proportional to the minimum E_t required for some fraction of the beam to clear the inflector after its first complete turn.

5.1.2 Maximizing Injection Clearance

For a commercial machine a high injection efficiency is required both to increase the speed of the measurements and to reduce the mass of sample material required. To maximize the efficiency, the radius gain from the injection point to the beginning of the second turn $\Delta r_{1\to 2}$ should be at least the radial width of the injected beam Δr_i. The orbital radius r of an ion of mass m and charge q in a flat magnetic field B is given by

$$r = \frac{mv_\perp}{qB},$$

where $v_\perp$ is the velocity component perpendicular to B. For nonrelativistic $^{14}C^-$ ions traveling in the median plane of a flat-field cyclotron this expression reduces to

$$r = 17\frac{\sqrt{E}}{B}, \tag{5.2}$$

where r is in units of cm, E is the energy in keV/ion, and B is the midplane magnetic field in kG. From equation 5.2 we can write an expression for the first turn clearance of an initially centered beam as a function of injection energy E_i and the first turn energy gain.

$$\Delta r_{1\to 2} = \frac{17}{B}\left(\sqrt{E_i + E_t} - \sqrt{E_i}\right). \tag{5.3}$$

The above equation may be rearranged to dictate energy gain per turn as a function of required radius gain, magnetic field strength, and injected beam energy. If we also set $\Delta r_{1\to 2}$ equal to Δr_i then

$$E_t = \left(\frac{B\Delta r_i}{17}\right)\left(\frac{B\Delta r_i}{17} + 2\sqrt{E_i}\right) \tag{5.4}$$

is the minimum energy gain that will permit 100% of the injected beam to clear the central region. If the energy gain is reduced below this level then the resolution of the

machine will increase in proportion to the turn number (which is linear with ΔE_{turn},) but the beam current will fall in proportion to the first turn radius gain.

5.1.3 Minimizing the Transit Time Effect in The First Turn

As we begin to explore high harmonic numbers (and shorter RF cycles relative to the beam's orbital cycle), we must consider the effect of transit time on the energy gain of the first turn. Because the dee voltage is varying while the particle passes through the accelerating gap, the energy gain of the particle will be reduced by a factor that depends on the width of the gap. For a first harmonic machine, Livingood derives an expression for the effect of transit time on energy gain of a single gap E_{gap} by using a particle's average velocity while in the gap:

$$E_{gap} = qV_{dee}\left[\frac{\sin X}{X}\right]\sin\phi$$

where

$$X \equiv \frac{g}{2r} \approx \frac{1}{2}\Delta\theta_{gap}$$

where g is the effective linear gap width, θ_{gap} is the effective angular gap width, and we have allowed the approximation $\sin(\Delta\theta_{gap}) \approx \Delta\theta_{gap}$. The effect of phase on energy gain is given by the factor $\sin\phi$ and the term in brackets is known as the 'transit time factor' [12]. For $h > 1$, X is replaced by hX which is approximately one half of $\Delta\tau_{gap}$, the angular width of the gap in RF degrees, or the time required to traverse the gap's electric field. In a low voltage cyclotron the dees may be spaced so close together that the effective gap length is dominated by the fringing of the electric field caused by the gap between upper and lower dee edges. Following the method of Jongen, [50] we can then approximate the effective gap length in the median plane as equal to the vertical aperture of the dee ΔZ_{dee}. In this case the time that a median plane particle

spends crossing the accelerating gap is roughly

$$\Delta\tau_{gap} = h\Delta\theta_{gap} \approx \frac{\Delta Z_{dee}}{r}.$$

If we rearrange the above equation into an expression for the harmonic number,

$$h \approx \Delta\tau_{gap}\frac{r}{\Delta Z_{dee}}\frac{2\pi}{360^{\circ}}, \tag{5.5}$$

then we have the maximum allowed harmonic that will result in a given maximum gap transit time as a function of injection radius and dee aperture. For a 1 cm dee aperture and an allowed transit time of $60^{\circ}RF$ the maximum allowed harmonic is roughly equal to injection radius measured in centimeters. In this case a median plane, on-phase particle would experience an effective dee voltage that is 95% of the actual dee voltage during the first turn.

5.2 Existing AMS Cyclotrons

Three cyclotrons have been built solely for the purpose of mass spectrometry. During the 1980s Lawrence Berkeley Laboratory (LBL) built a proof-of-principle machine known as the 'cyclotrino,' which had 10 cm radius flat poletips and relied on the fringe electric field in the dee gaps to provide vertical focusing [51]. The cyclotrino detected ^{14}C at natural levels but suffered from a very small phase acceptance. A successor to the cyclotrino with an improved injection system and a novel permanent magnet system is nearly completed and awaits testing at LBL [52].

At the Shanghai Institute of Nuclear Research, Chen *et al.* have extracted ^{14}C from a 48 cm radius sector focused cyclotron [53]. A schematic of the Shanghai Mini-Cyclotron for AMS (SMCAMS) is shown in Figure 5.1. The SMCAMS uses an unconventional dee structure to provide greater energy gain on the first and last turns

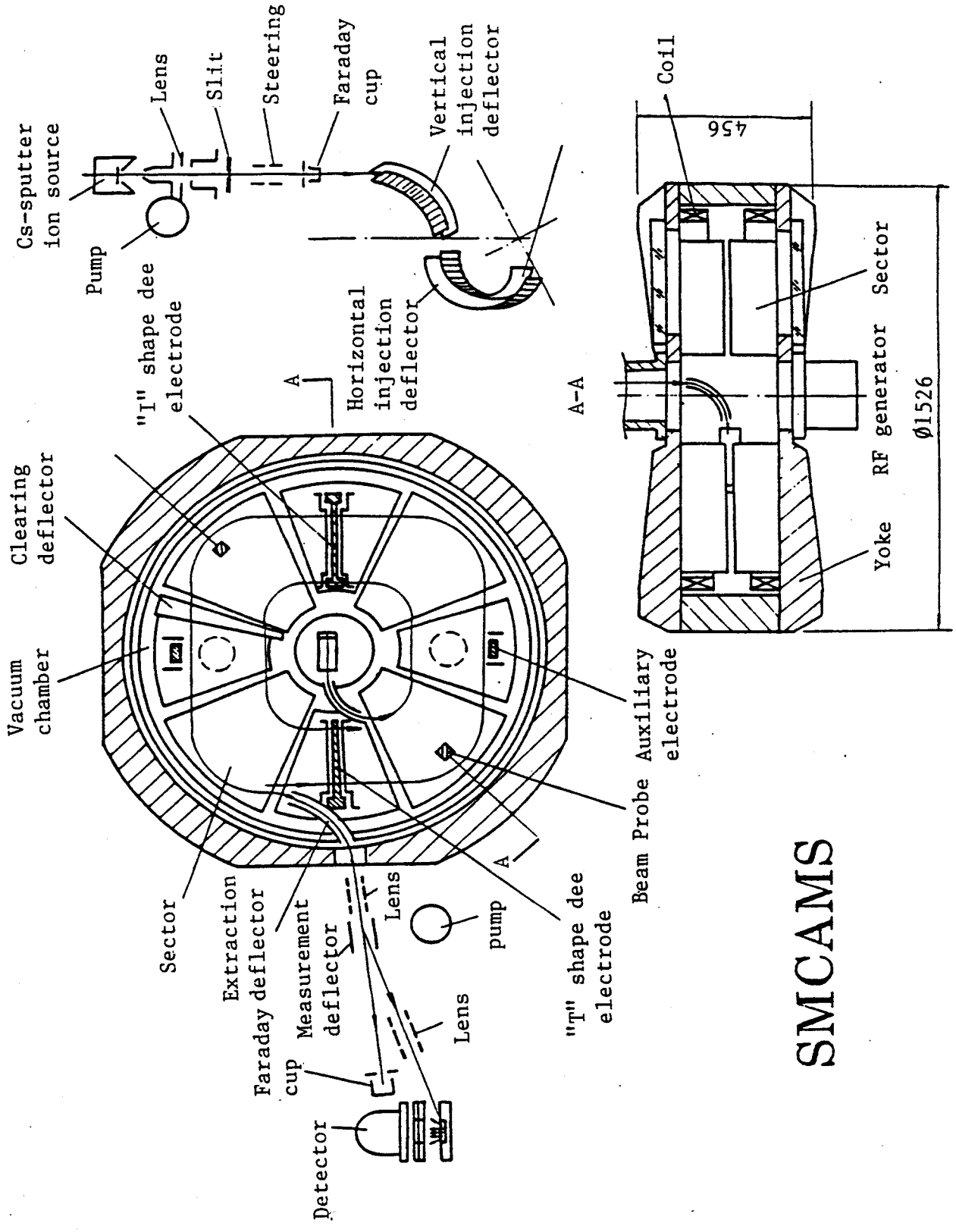

Figure 5.1: The Shanghai Mini Cyclotron for AMS [54]. Dimensions on the yoke are in mm. The injection and extraction radii are 20 cm and 48 cm respectively. The ^{14}C detector is shown on the far left. ^{12}C current is measured in the faraday cup next to the ^{14}C detector in order to normalize the count rate.

Table 5.1: AMS cyclotron design parameters.

Parameter	SMCAMS	LBL Cyclotrino	LBL Permanent Magnet Cyclotron
Resolution	3000	variable	1800
Ion Source	Cs sputter	Cs sputter	Magnetic multicusp
Ion Species	Carbon 14	Carbon 14	Carbon 14
Injector type	Vertical and horizontal electrostatic channels	Midplane injection with electrostatic mirror	Spiral inflector
Injection energy	20 keV	5 keV	5 keV
First orbit radius	24.5 cm	2.8 cm	4 cm
Extraction radius	47.5 cm	10.5 cm	12 cm
Extraction energy	50 keV	40 keV	50 keV
Pole face radius	60 cm	15 cm	15 cm
Pole gap	2.5 cm	3.2 cm	1.6 cm
Magnetic Field	2.35 kG average 4 kG in hills	1 T	1 T
Field source	normal magnet	normal magnet	SmCo Magnets
Harmonic number	16	11-15	15
RF frequency	4.8 MHz	11-15 MHz	16 MHz
vertical dee aperture	10 mm	8 mm	N/A
RF voltage peak	500 V	300-400 V	N/A
Number of dees	4	1	1
Energy gain per turn	500 eV	260 eV	500 eV
First turn separation	6 mm	1 mm	2 mm
radial width of injected beam	$\leq$6 mm	3 mm	N/A
Minimum turn number	100	50	40
Reference	[56, 53]	[49, 57, 51]	[46]

(to minimize injection and extraction losses) and a lesser energy gain in between to allow a large number of turns.

Basic parameters of the three cyclotrons are shown in Table 5.1. In all three machines individual ^{14}C ions are counted using a detector developed for cyclotron AMS at Berkeley [55]. The low operating voltage raises the possibility of using non-sinusoidal RF waves, such as a flat-topped sine or even a square wave, to increase the phase acceptance of the cyclotron. Chen *et al.* claim to have increased their total particle acceptance by a factor of 30 by using a novel triangular waveform with off-peak acceleration [56]. The SMCAMS has achieved a resolution of 3000 with an extracted ^{12}C beam of 500 nA, which corresponds to 5 counts per second of ^{14}C in a sample of 'modern' carbon (i.e. a sample with an atmospheric $^{12}C/^{14}C$ ratio.)

5.3 Feasibility of a Low Cost Cyclotron Using the Airport Cyclotron Magnet

Our goal is to design the cheapest possible system capable of measuring radiocarbon for outside users at the NSCL. We are also interested in a system that is suitable for accelerator development work to improve resolution and/or injection and extraction efficiency.

Although radiocarbon can be detected with a resolution as low as 1800, we will aim for 2400 as a conservative starting point. For simplicity we will use an available magnet and assume for this study that its geometry is fixed. Thus, we begin our conceptual design with the mothballed NSCL beamline steering dipole known M3. In the early nineties a development program sought to convert M3 into a four sector cyclotron for contraband detection (the 'airport cyclotron.') Poletips were procured and the midplane field was modeled and mapped [58]. An eighth section of the yoke

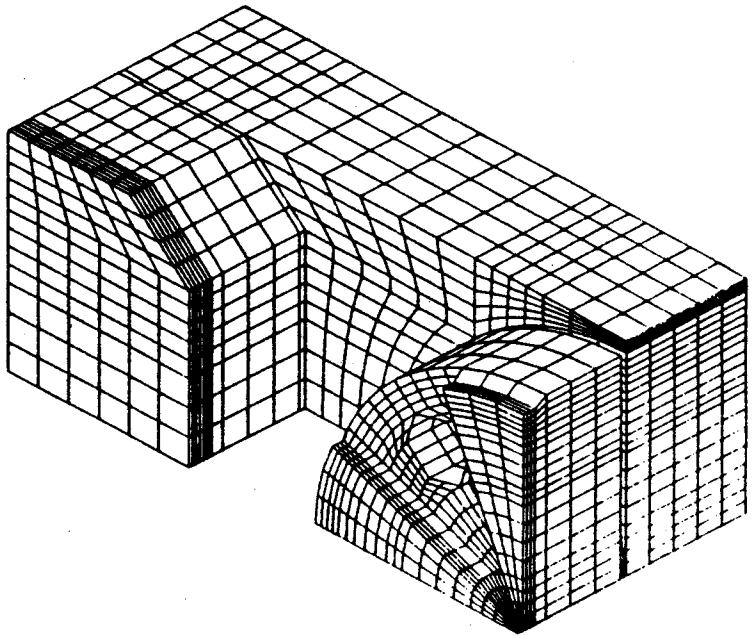

Figure 5.2: Mesh used for the calculation of the midplane magnetic field of the airport cyclotron [58]. One eighth of the magnet is represented, with the machine's central axis at the lower right.

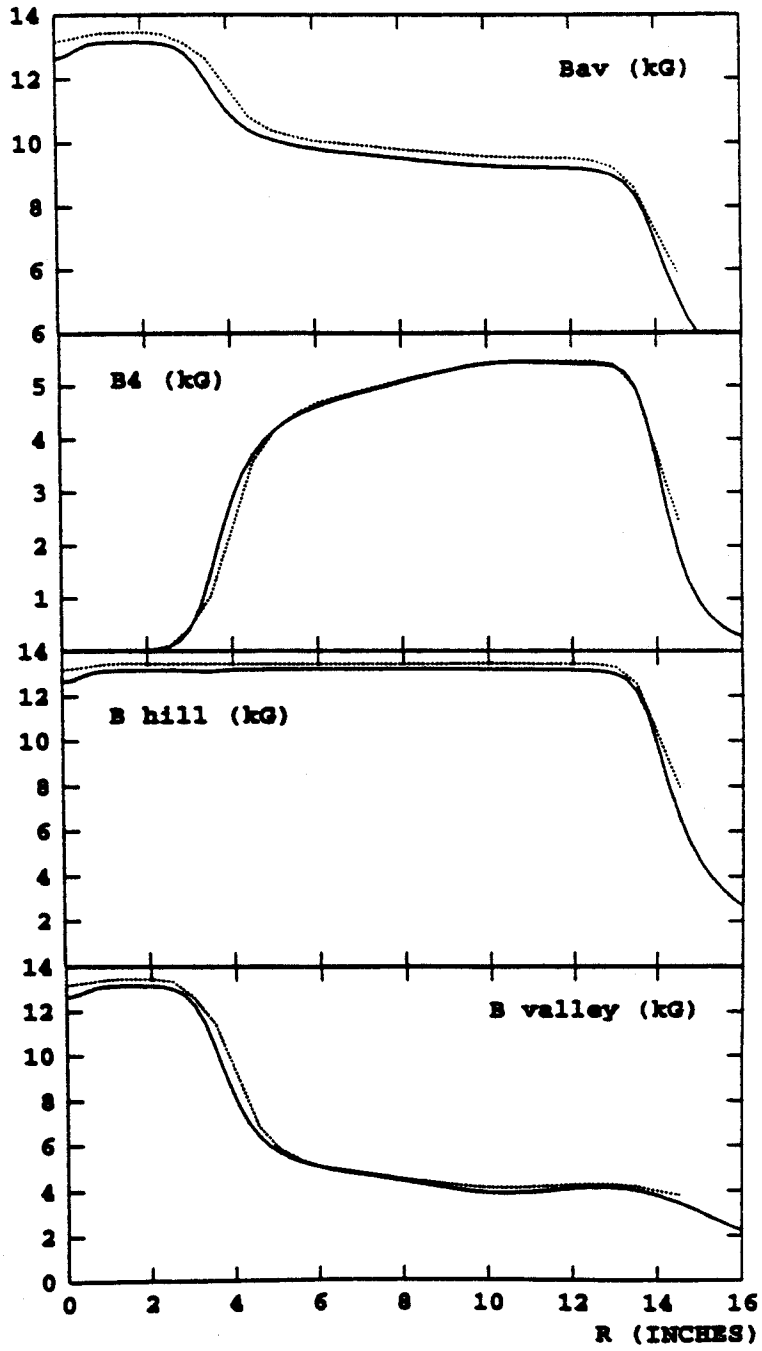

Figure 5.3: Main field parameters in the median plane of the airport cyclotron magnet for both the calculation (dashed line) and measurements (solid line) [58]. Since the magnet iron is unsaturated, the field shape should be preserved when the overall field level is reduced to match the requirements of the AMS cyclotron.

and poletip is shown in Figure 5.2. Properties of the midplane field are plotted in Figure 5.3. Because of the low energy involved, the field index $k \approx \gamma^2 - 1$ should be negligible beyond the central focusing cone and spiral sectors are not needed to provide focusing. Equation 2.8 then shows that axial focusing is dominated by flutter. Because the magnet iron is not saturated, flutter should be roughly constant for any excitation of the magnet, and in this magnet flutter should be dominated by the fourth harmonic component of the field. Equation 2.8 then reduces to

$$\nu_z^2 \approx \frac{1}{2} \frac{N_{sect}^2}{N_{sect}^2 - 1} \left(\frac{B_4}{\langle B \rangle} \right)^2 \tag{5.6}$$

for radii beyond the central field cone. Equation 5.6 yields $\nu_z = 0.4$ using $\frac{B_4}{\langle B \rangle} \approx \frac{5}{9}$ based on the data in Figure 5.3. The nearly flat $\langle B \rangle(r)$ function (beyond the field cone) means that ν_r will be approximately unity for this region. Although this prolonged resonance is undesirable, Bertsche has shown that the detrimental effects of radial instability in a low energy cyclotron can be minimized by properly centering the beam [59].

To maximize the accelerated current we need a highly isochronous field. Any phase shifts during acceleration will push some of the ^{14}C beam beyond $\sin\phi = \pm 1$ and these particles would be lost. Therefore the central focusing cone built into the airport cyclotron, with its associated phase shift, is undesirable. As in the SMCAMS we should plan to inject the beam at a great enough radius that flutter focusing is already near its maximum value so that the beam will use little or none of the cone field. In this case, the airport cyclotron would offer a minimum injection radius of approximately 12.7 cm (5") and a maximum extraction radius of about 31.75 cm (12.5"). Any average field level can be used up to a maximum of 9 kG.

A used commercial Cs sputter negative ion source was located that could produce a 20 keV beam with a 15 mrad divergence that appears to originate from a 2 mm

diameter spot [60]. Since the beam will experience some growth in the injection beamline we make a conservative guess that the beam will have a 3 mm waist when injected into the cyclotron. It is worth noting that the cyclotrino group minimized the size of their machine by extracting a 5 keV beam from a commercial source designed to make a 20 keV beam. This increased the normalized emittance of their beam to a value that was not accurately determined [49]. Since our magnet is three times larger than the cyclotrino magnet we should have no need to reduce the starting energy below 20 keV for the initial design.

If we try a harmonic number $h = 16$ (based on the SMCAMS) then roughly $N = 50$ turns would be needed to make a resolution of $R \approx 3Nh = 2400$. Based on the Berkeley and Shanghai experience we will plan to extract a 50 keV beam. Since a total energy gain of 30 keV is needed the energy gain per turn should be
$30\ keV/50\ \text{turns} = 600\ eV/\text{turn}$.

Now we must see if a magnetic field level exists which will allow a 3 mm separation between the first and second turn while permitting us to inject and extract beam (with the desired energies) at radii that fit within our fixed magnet geometry. Equation 5.3 tells us that in a flat field a 3 mm turn separation can be achieved between 20 keV and 20.6 keV with a field of 3.78 kG. Orbit tracking studies in an actual magnetic field map would be required to properly account for the scalloped orbit that occurs in a magnet with sectored poletips, but at this stage we only need an approximation to establish the basic parameters.

If the average field of our magnet is set to 3.78 kG then the injection radius for a 20 keV ^{14}C beam would be roughly 20 cm (8") which is well above the minimum working radius of our magnet. We can see from Figure 5.3 that by this radius the flutter field has turned on and there is no need for the magnetic focusing cone, or a

complex central region for electric focusing. The center plug which shapes the cone field could be removed to make room for a bulky injection channel similar to the one used in Shanghai. The beam would be centered by adjusting the position of the injection channel.

At this radius if we choose a vertical dee aperture of 1 cm (similar to that of the cyclotrino) then the maximum harmonic that would allow an effective gap length of $60° RF$ would be $h \approx 20$ so transit time effects should not cause any problems in this cyclotron.

The extraction radius for ^{14}C at $B = 3.78$ kG would be approximately 32 cm (12.5") which is at the edge of the flat field region of our magnet. The maximum pole radius of the Airport magnet is 33.6 cm (14") with a 3.81 cm (1.5") pole gap. If more space were needed after accounting for scalloping we could add hill shims to reduce the pole gap at large radii and extend the maximum working radius of the magnet. Both SMCAMS and the Berkeley cyclotrons use a short electrostatic channel to extract the 50 keV beam. Since our extraction radius and local field will be in between those of the Shanghai and Berkeley cyclotrons, the design should be straight-forward.

It would not be necessary at first to use the advanced dee structures under development in China. An experimental machine could work with a set of wedge-shaped dees and traditional on-peak acceleration. RF power would be minimized with an array of 16 dees, each 11.25° wide. Unfortunately such an arrangement would limit mechanical space for other subsystems such as the injection and extraction channels, and a vertical 'clearing deflector' that is used to periodically remove background ions that accumulate at intermediate radii. Furthermore, Chen has pointed out subtle phase shift phenomena that occur when the dees are not aligned with the centerlines

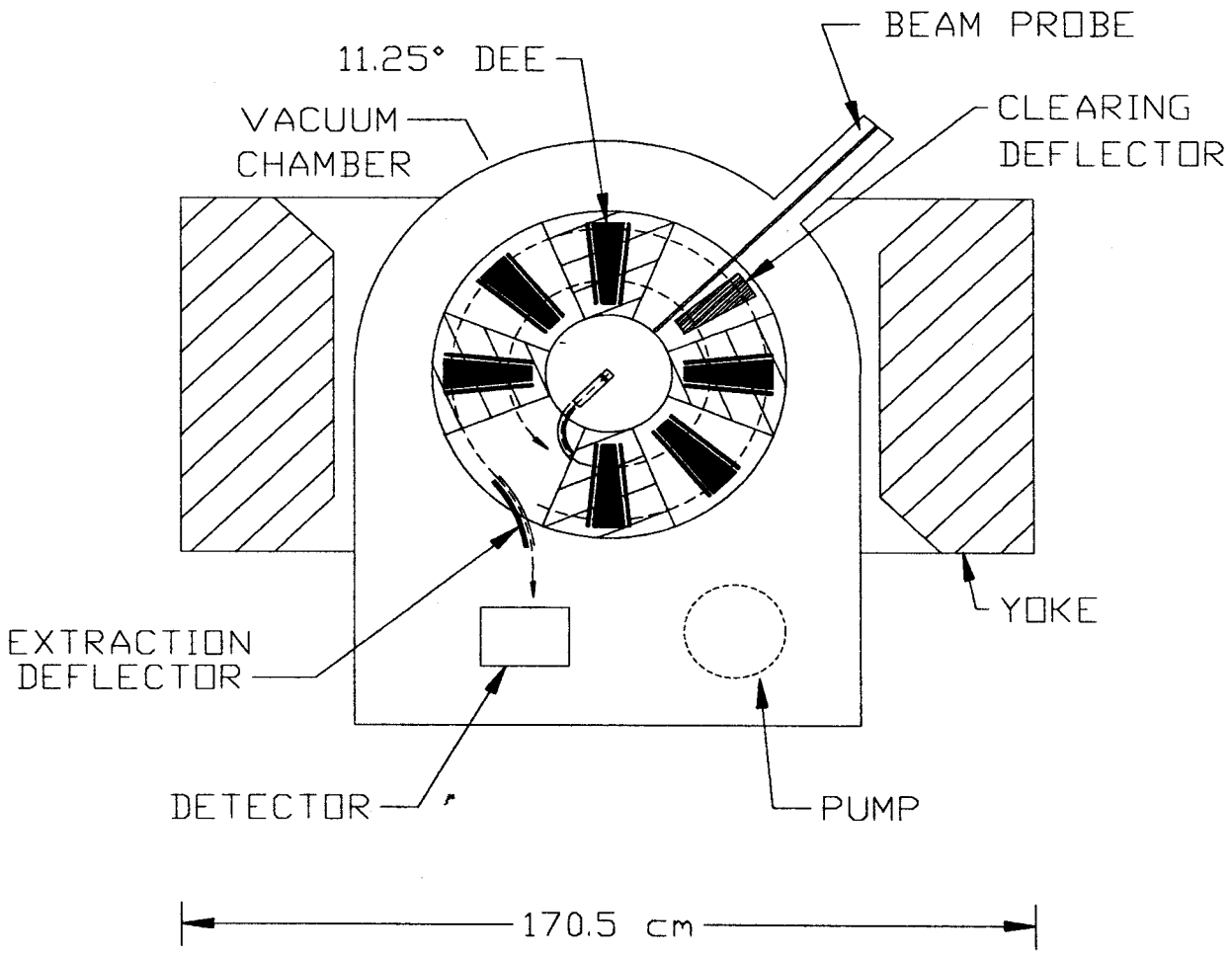

Figure 5.4: A simple AMS cyclotron designed to make use of the Airport cyclotron magnet.

of either a hill or a valley [61]. A more likely dee arrangement is shown in Figure 5.4. With six dees the effective gap voltage would need to be 50 V.

Using the approximation from section 5.1 we calculate a gap transit time at injection of $45°RF$ which would result in a transit time factor of $\frac{\sin(X)}{X} = 0.97$. The peak dee voltage needed to accelerate on-phase particles with enough radius gain on the first turn to clear the injection channel would be 51 V, with an RF frequency 6.65 MHz.

At this low voltage there should be no problem locating dees in the 3.81 cm hill gap, and the dees and dummy dees could be mounted on insulators to simplify the mechanical structure. Furthermore it might be economically feasible to use a nonresonant RF system. If we assume that a solid-state broadband transmitter excites the dees in parallel with a 50 Ω impedance, the total RF power $P_{RF} = \frac{1}{2}\frac{V^2}{R}$ would be only 26.3 W.

5.4 Advanced RF Systems

The resolution of an AMS cyclotron may be increased if the energy gain decreases after the first turn has cleared the injection channel, allowing for more turns in a given design. Jongen proposed a system of rectangular 'sandwich dees' which are $180°RF$ wide at their inner radius and are narrower in azimuth at greater radii. This means that a $\phi = 0$ particle is accelerated by the peak voltage of the RF wave on the first turn but afterward it uses the side of the RF wave so energy gain is reduced in proportion to $\sin(\Delta\tau_{dee})$ where $\Delta\tau_{dee}$ is the width of the dee in RF degrees. The dees themselves take on the appearance of narrow strips that are 'sandwiched' in between the dummy-dees.

Chen *et al.* have adopted sandwich dees in a modified form [61]. The dees (shown

in Figure 5.1) are shaped like a capital letter 'I' so that at the injection radius the dee width is set for optimum energy gain, and then the dee tapers to reduce the energy gain per turn. Near the extraction radius, the dee widens again to raise the energy gain and increase the turn spacing prior to extraction. A pair of 'auxiliary' dees are installed near the outside of the two remaining valleys to further increase the final turn spacing and maximize the extraction efficiency.

The reduction of energy gain with radius in an isochronous cyclotron has the effect of expanding the phase width of the beam. Joho has demonstrated that

$$E_t \sin \phi = constant \tag{5.7}$$

for any given particle, so when E_t is reduced the range of phases within the beam increases [62]. Although this phenomenon will hasten the removal of background particles from the AMS cyclotron, it will also push a fraction of the radiocarbon ions beyond the phase acceptance of the machine. In this case reduced transmission efficiency is traded for increased resolution.

The simplest way to compensate for a low phase acceptance is to use a buncher [63] to compress the DC beam from the ion source into a train of narrow pulses that are synchronized with the cyclotron RF system.

The Shanghai AMS cyclotron employs a triangular RF wave to increase the phase acceptance of the machine itself. In this scheme the dees are always less than $180° RF$ wide and all particles are accelerated by the side of the RF wave. An on phase particle will be pulled into a dee and pushed out of it with kicks of equal strength. An early particle will receive a stronger kick than the $\phi = 0$ particle on entering the dee but a weaker kick on leaving the dee. A late particle will receive the opposite effect. In the case of a sinusoidal RF wave, the off phase rays would still receive a lower net acceleration than the $\phi = 0$ particle. If the dee voltage is linear with time,

however, the early, late and $\phi = 0$ particles will all receive the same total energy. The narrow dee, triangular wave combination is similar to the use of $180° RF$ dees with a flat-topped wave. If one could make a perfectly linear sawtooth RF wave then the accepted phase width would be the 180° accelerating portion of the RF cycle less the transit time in the first gap.

In practice the Shanghai group estimates that their cyclotron's accepted initial phase width is increased from ±2° for the sinusoidal RF wave case to ±20° with a triangular RF wave. Because axial behavior is coupled with longitudinal (phase) behavior, the total particle acceptance is estimated to increase by a factor of 30 [56].

5.5 Conclusion

Cyclotron based AMS offers an elegant low cost alternative to AMS performed with a tandem Van de Graaff accelerator and magnetic dipole mass spectrometer. Coupled with a buncher and/or Shanghai-style triangular RF wave, the AMS cyclotron might compete with tandems in terms of efficiency as well as cost.

Chapter 6

HIGH ENERGY COMMERCIAL CYCLOTRON FOR CANCER THERAPY

The CYCLONE 235, or 'C235' cyclotron is a commercial product of the Belgian firm Ion Beam Applications (IBA) [64]. The cyclotron is designed to deliver a 300 nA 235 MeV proton beam for cancer therapy. As of this writing (December 1997) the prototype C235 is being commissioned at the Northeast Proton Therapy Center at Massachusetts General Hospital. The C235 is part of a new proton therapy system designed by IBA to minimize "...the size, the investment, the complexity, and the cost of operation..." of the entire facility [4]. It is also the highest energy cyclotron yet to be commercialized, and it uses the highest magnetic field of any non-superconducting cyclotron. In this way the cyclotron exploits the cost savings of high-field, compact magnets without introducing a complex cryogenic system into the hospital environment. General features of the cyclotron are shown in Figure 6.1. The cyclotron uses a four sector magnet with two dees in opposite valleys. The dees are galvanically coupled at the center by an 'RF Bridge.' The RF system operates in fourth harmonic mode so that, as in the Harper and 8 Tesla Cyclotron designs, the peak RF voltage of each cycle is used to accelerate on-phase particles.

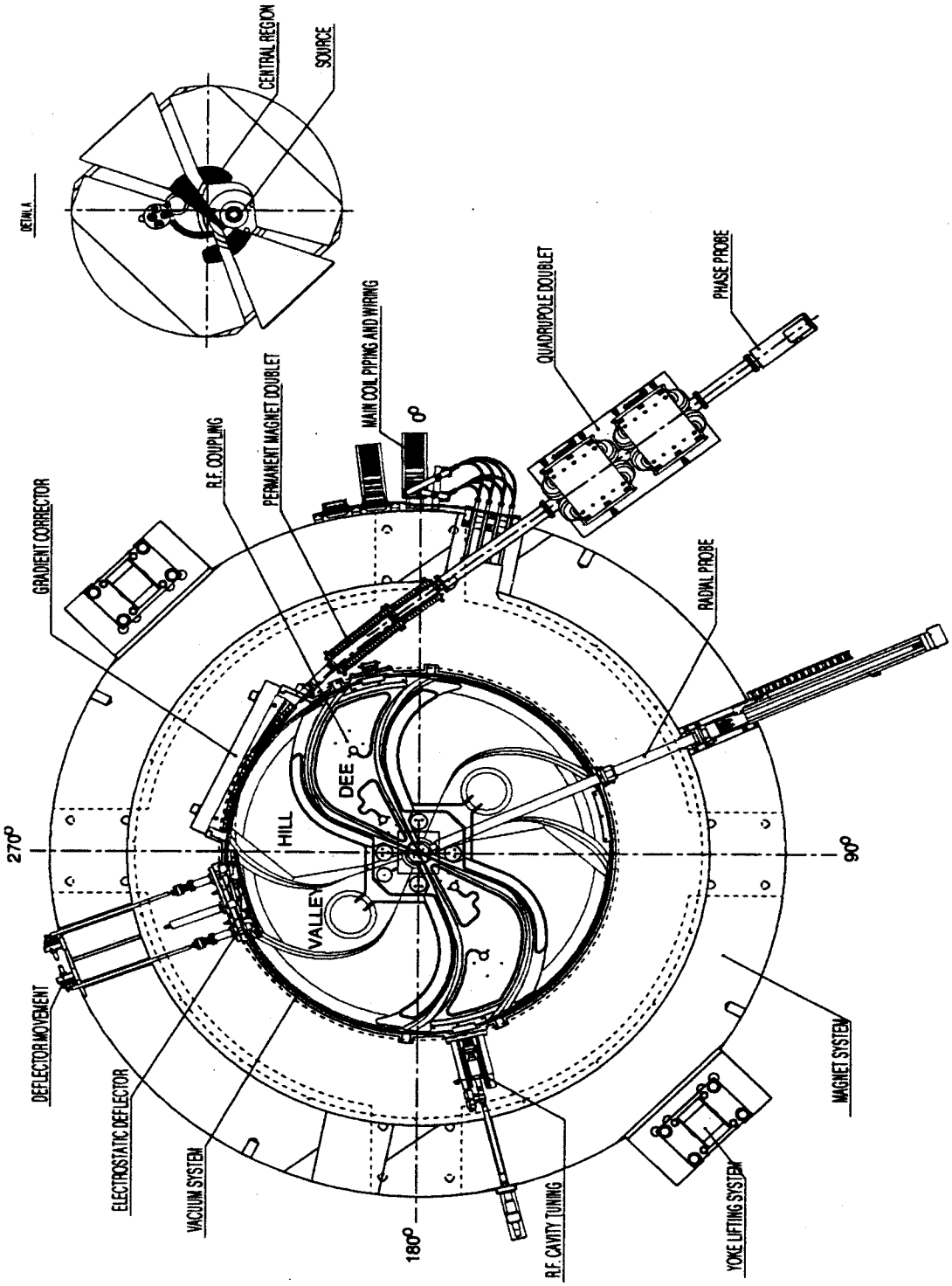

Figure 6.1: A median plane view of the C235. The Yoke is 4.3 m in diameter. The central region, with a 1 cm diameter filament ion source is shown at the upper right. Four circular harmonic coils are shown near the inner radius of each hill. (The circular coils have been replaced by triangular coils to make better use of the limited space available near the central region.) (Courtesy of Ion Beam Applications, Louvain-la-Neuve, Belgium.)

6.1 The IBA-NSCL Collaboration

6.1.1 Goals

The work presented in this chapter is part of an NSCL review of the 'as built' C235 cyclotron. The purpose of this study is "to better understand the behavior of the beam in the present configuration of the cyclotron and...to suggest modifications that would improve the quality of the beam to reduce losses at high energies." [65]

The C235 is at this time producing extracted beam at greater currents than are needed for proton beam therapy, but improvements that reduce secondary radiation in the machine vault will have the desirable effect of allowing more convenient maintenance of the machine as well as producing greater confidence in the technology for potential additional customers. For these reasons secondary radiation levels, and factors that contribute to secondary radiation such as internal beam losses, are figures of merit for the C235 (as for any cyclotron.)

6.1.2 Scope

The IBA-NSCL collaboration has studied the ion orbits from the ion source through the extraction channel. The present report is concerned primarily with the central region and orbits within 40 cm of the center of the machine. The extraction studies will be documented elsewhere.

6.1.3 Methods

NSCL has performed orbit calculations in the C235 central region using our orbit code Z3CYCLONE [16]. The calculations use a magnetic field based on maps made in the IBA factory and modified at the NSCL to account for changes in the iron configuration made after mapping. The electric field for the orbit calculations was

calculated at NSCL based on drawings provided by IBA (updated with measurements of modifications to the central region geometry taken by the MSU team during a visit to the Boston site in August 1997). The resulting field maps are assumed to represent the magnetic and electric fields of the machine as built [66].

6.1.4 Timeframe

This study was conducted between May and October of 1997. During this time experimental data was available from the IBA team in Boston, and empirical studies of possible improvements by the IBA team ran concurrently with the computational studies at MSU. Most of the adjustments tested in Boston concentrated on alternative configurations of the iron shims that are used to fine tune the magnetic field. The magnetic field used for the calculations in this chapter corresponds to the configuration that was in place when the collaboration began in mid May of 1997. This iron configuration was in place during most of the time period of this study; more recently important progress has been made by the IBA Boston team in improving the isochronism of the cyclotron's magnetic field which will change some of the detailed results reported herein. A principal aim of this report, therefore, is to document the study methods in case it is decided to repeat the analysis when more up-to-date magnetic field maps are available.

6.2 Summary of Magnetic Field Properties of the C235

The magnetic field of the C235 was mapped at the IBA factory during 1996. At this time iron shims were added to isochronize the field and the field was remapped. The final map produced, denoted 'map133,' was provided to the NSCL team for this study. During the initial beam tests at the IBA factory several additional modifi-

cations were made to further improve the magnetic field. We have accounted for these modifications with our own magnetic field codes which represent the added (or removed) iron as a 1.7 MA/m current sheet flowing around the r-θ perimeter of the shim. The effect of each iron change is calculated separately and the resulting field contributions are superimposed over the mapped field. This model is strictly true if 1) the added or removed iron is fully saturated, 2) if the magnetic dipole moment of the iron is uniform in the axial direction, and 3) if the added or removed iron has no effect on the magnetization of the unchanged parts of the iron components. The model has been frequently used at NSCL and has been found to be an accurate approximation for iron shims in a high field cyclotron magnet such as the C235.

The following changes were made to the mapped poletip configuration:

- The 'central rings' (O.D. 54 mm with a dumbell shaped hole for the ion source) were moved further away from the median plane. For the final mapping the central rings were +/-60 mm away from the median plane. Later 2.7 mm and 1.7 mm was removed from the upper and lower central ring, putting their median plane surfaces at Z=62.7 mm and Z=-61.7 mm respectively.

- The 'central plugs' (I.D. 54 mm, O.D. 100 mm) were moved closer to the median plane. For the final mapping the hill sections of the central plugs were +/-56.5 mm away from the median plane. Later 1.9 mm and 2.5 mm of iron was added to the upper and lower plugs, putting their median plane surfaces at Z=54.6 mm and Z=-54.0 mm respectively.

- A set of side shims, two above and two below the median plane, measuring $10 \times 16 \times 53$ mm, were added to two opposite hills at a radius of 100 mm. These are sometimes referred to as the '10 cm blocks.'

- A set of side shims, two above and two below the median plane, measuring 10×5×21.5 mm were added to two opposite hills at a radius of 890 mm in the valley with the deflector and at a radius of 888 mm in the valley with the radial probe. These are sometimes referred to as the '1-I' shims.

- A set of trapezoidal side shims two above and two below the median plane, measuring 20×2 mm at the base and 14-16 mm high, were added to two opposite hills at a radius of approximately 1070 mm in the valley with the deflector and at a radius of 1057 mm in the valley with the radial probe. These are sometimes referred to as the '3-III' shims.

- The gradient corrector channel, an iron element of the extraction system that improves axial focusing by reducing the radial gradient of the magnetic field where the beam passes through the field edge, was shortened by approximately 6 cm.

The effect of all these changes is shown in Figure 6.2. The changes in the gradient corrector and the '1-I' and '3-III' shim sets are highly localized and have little effect on the field inside a radius of 40 cm. For consistency, however, we have used the same field map for the central region studies as for the extraction studies.

In addition to adding the contribution of the changes described above, the following modifications to the field map were necessary in order to make the magnetic field compatible with our orbit codes:

- The field was interpolated to provide data at a uniform radial step of 0.5 cm.

- The field was interpolated to provide data at an azimuthal step of 1°.

- The data was converted from units of gauss to kG and rewritten in FORTRAN's

F9.5 format. The procedure added one decimal place to the data (changing the final decimal to the .01G column) prior to calculating the above modifications.

(Additional fields were produced with 0.5° azimuthal steps to assist with the interpolation process and IBA measured large-radius field data with a 2 mm radial step was used for the extraction studies, but these fields were not used for the orbit calculations in this report.)

The NSCL orbit codes use a two dimensional median plane magnetic field as input. The off median plane field is calculated within the programs using a Taylor expansion. Median plane symmetry is therefore enforced by these codes. Where asymmetric modifications to the iron configuration were made we used the average of the upper and lower iron position to calculate the magnetic field. (The inclusion of asymmetric magnetic features in our model would require much greater effort than was feasible within the scope of this project.)

The mapped and modified magnetic fields are plotted in Figures 6.3 through 6.4. The map133 data which has been interpolated to work with our codes is denoted IBAINT.DAT, and the field with the modified iron structure is denoted IBAFILLGM2.DAT.

In addition, a 90° magnetic field named IBAFILLGM24.DAT has been produced by averaging the four corresponding field values from each sector to produce an 'average sector.' The Equilibrium orbit properties for this field and an average sector version of MAP133 are plotted in figures 6.5 through 6.8. The central region modifications appear to have smoothed over a region of low ν_z at $r = 10$ cm. The presence of the shim set at $r = 89$ cm is also apparent in the ν_z and ν_r curves.

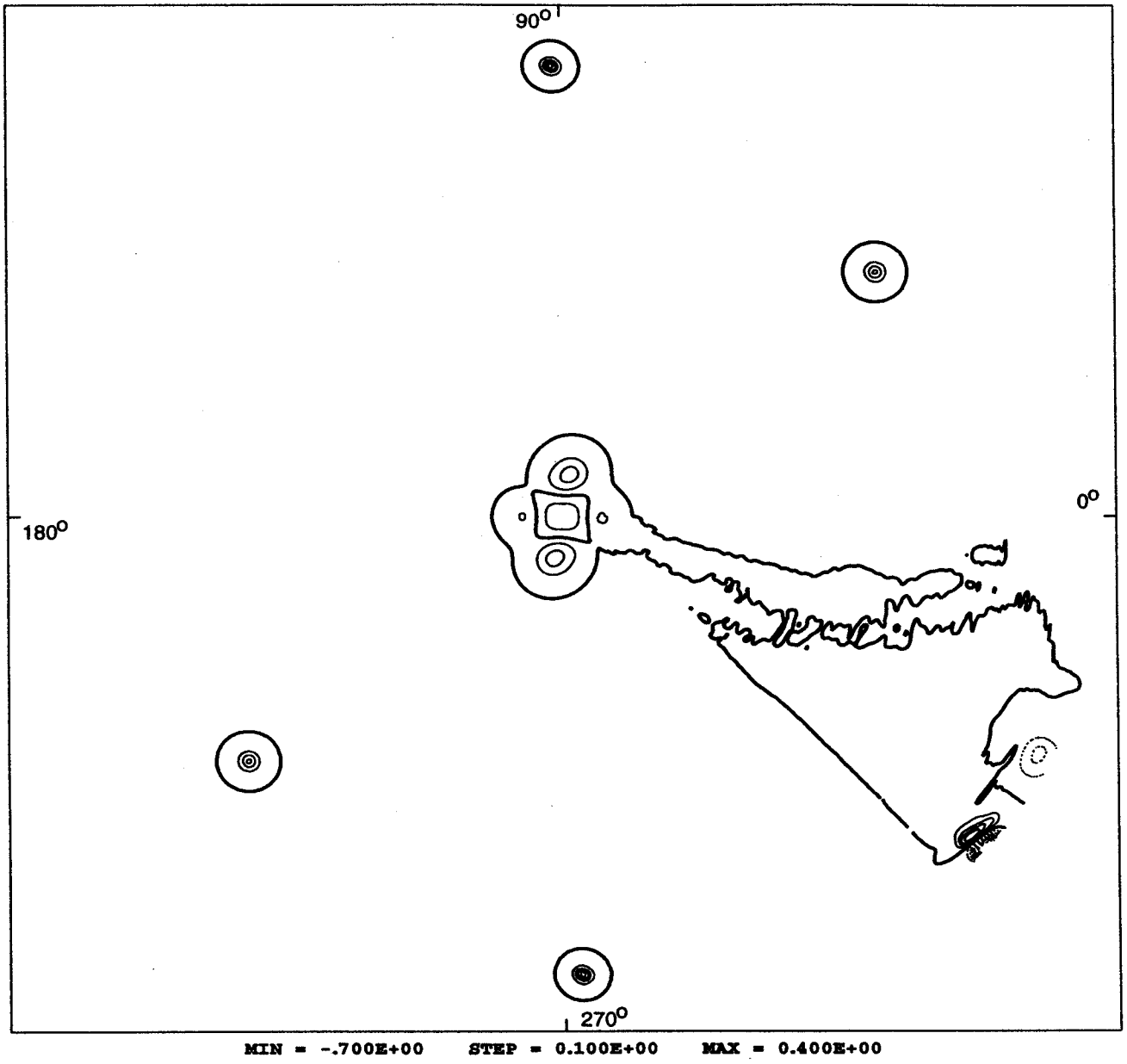

Figure 6.2: Contour plot of the modifications to map133 that were calculated at MSU. Contours are spaced 0.1 kG apart. The double weight line indicates the 0.0 kG contour. Negative contours use a dotted line. (The contour nearest the center is also negative, representing -0.1 kG.) The frame is 2.4 m square. The field is oriented so that the beam rotates counter clockwise. The effect of the shortened gradient corrector appears at the lower right. In order to fully resolve the small iron modifications at large radii, interpolated fields with a .5° step were used to make this plot.

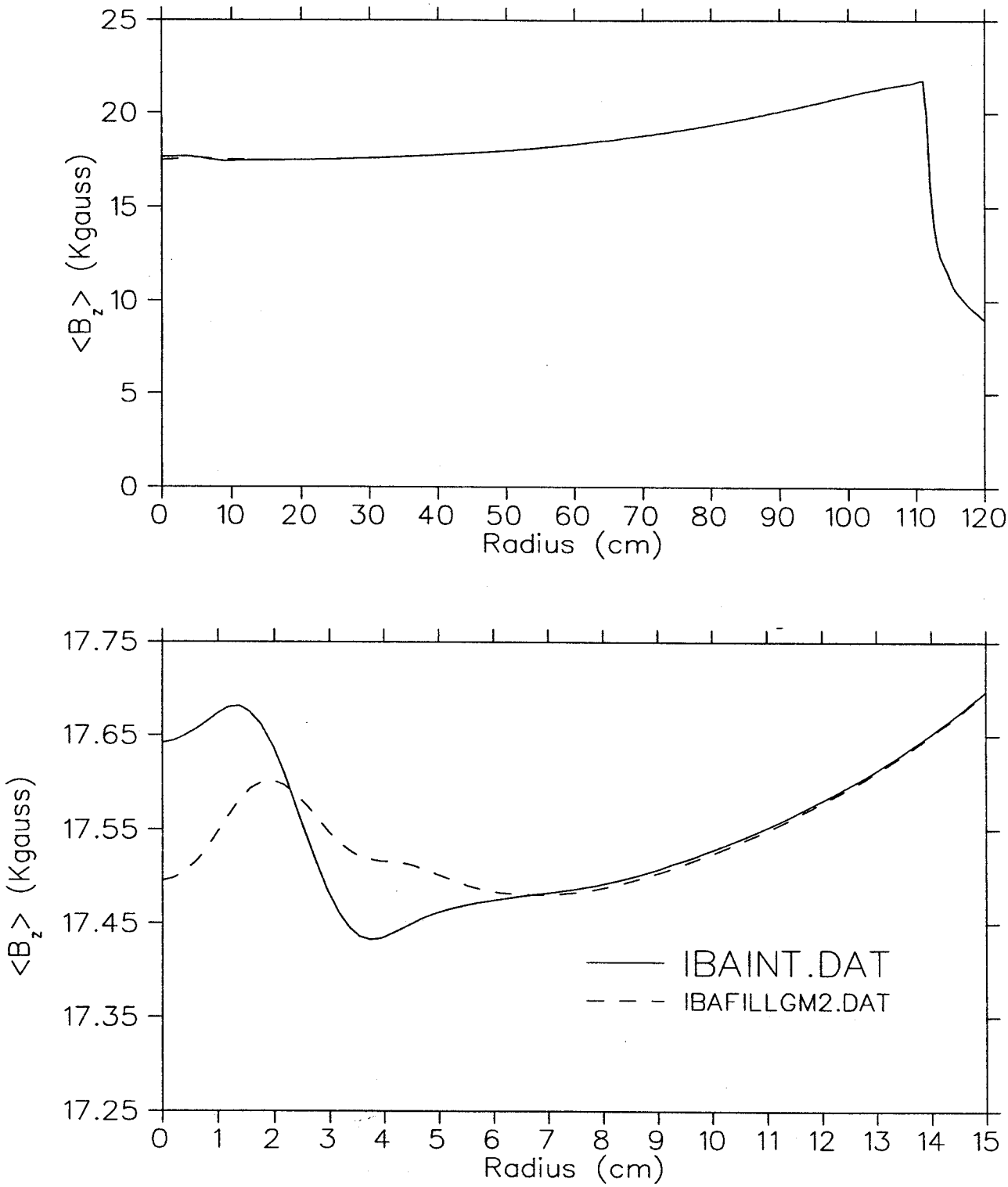

Figure 6.3: The azimuthal average of the axial component of the median plane magnetic field provided by IBA (solid line) and after the modifications computed at the NSCL (dotted line).

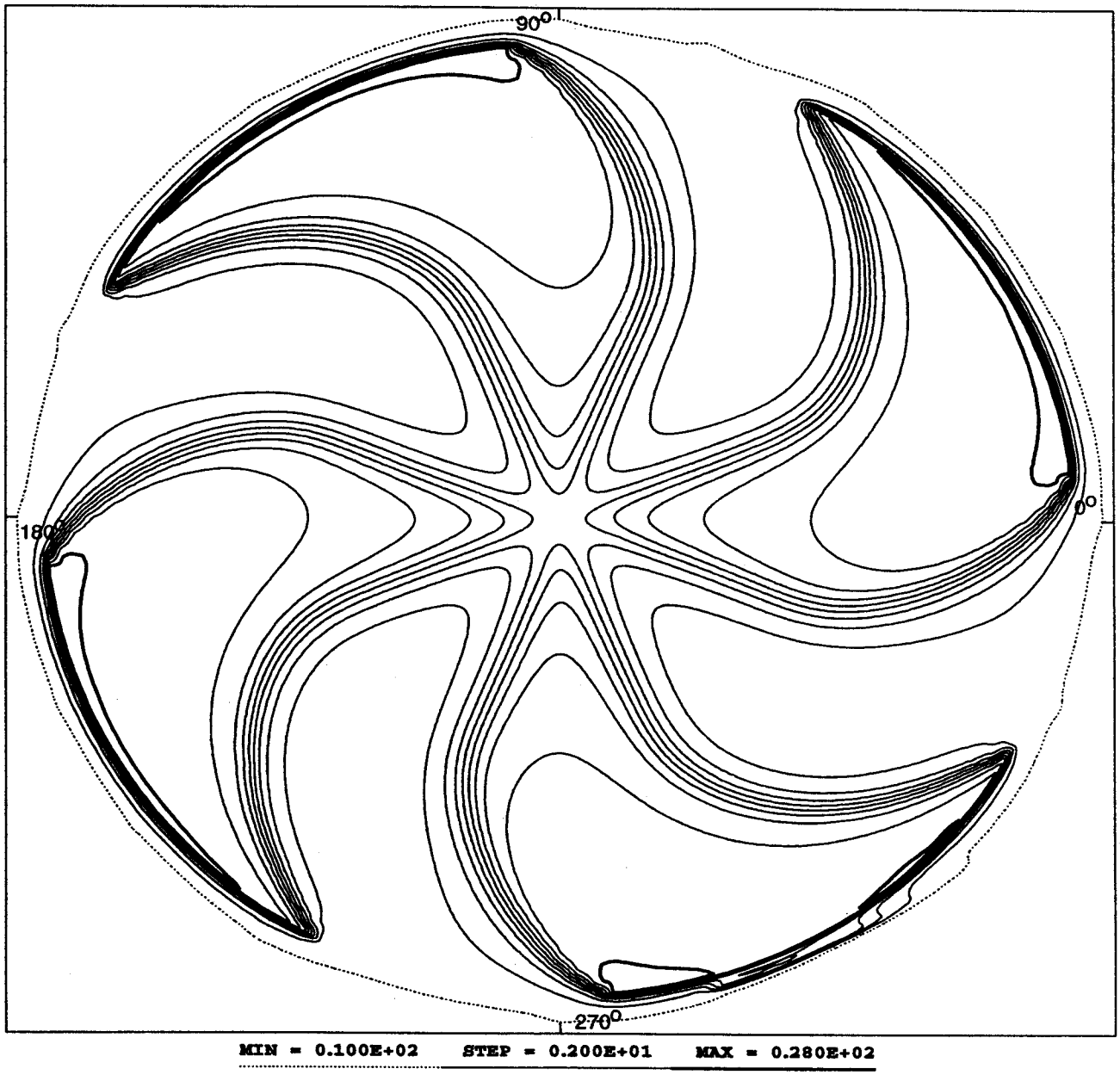

Figure 6.4: Contour plot of the modified magnetic field, IBAFILLGM2.DAT. Contours are spaced 2 kG apart with the dotted contour at 10 kG and the double weight contour at 28 kG. The frame is 2.4 m square

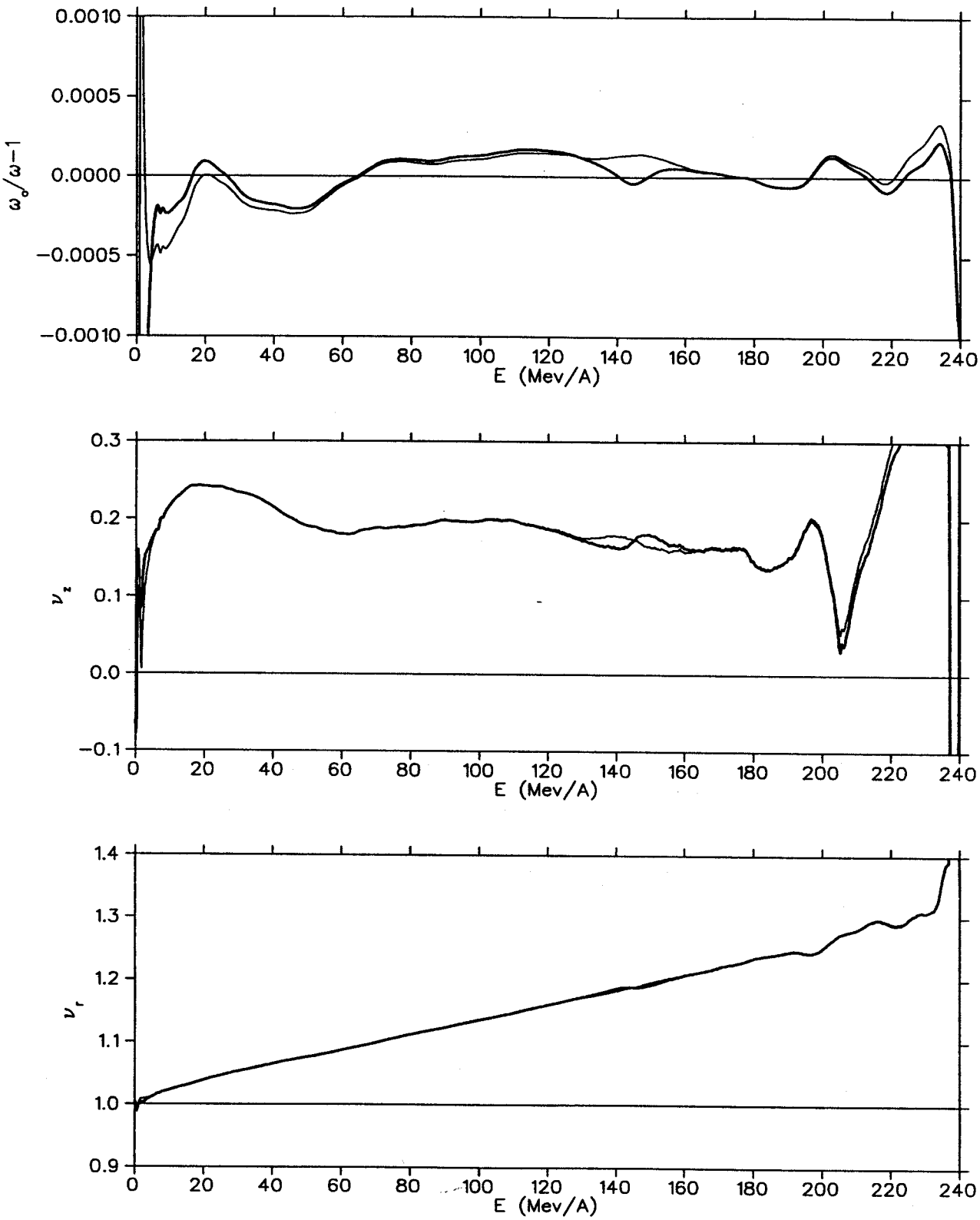

Figure 6.5: Equilibrium orbit properties for the 90° 'average sector' field plotted as a function of energy for the mapped (fine line) and modified (double weight line) magnetic fields. Top: orbital frequency relative to isochronous frequency. Middle and bottom: axial and radial focusing frequencies.

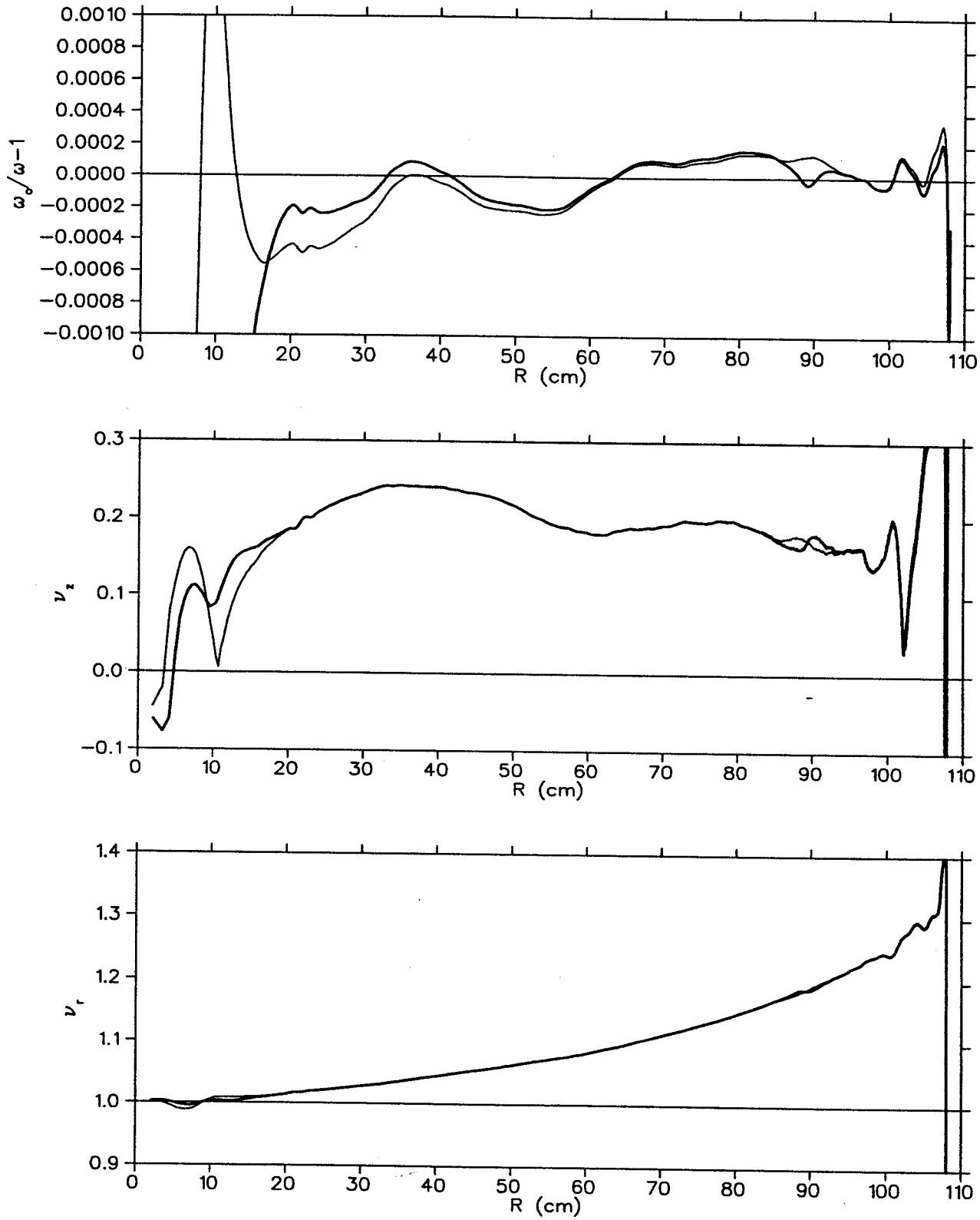

Figure 6.6: The same equilibrium orbit properties as in Figure 6.5, now plotted as a function of radius. Properties of the mapped field are plotted with the fine line and those of modified field are drawn with the double weight line.

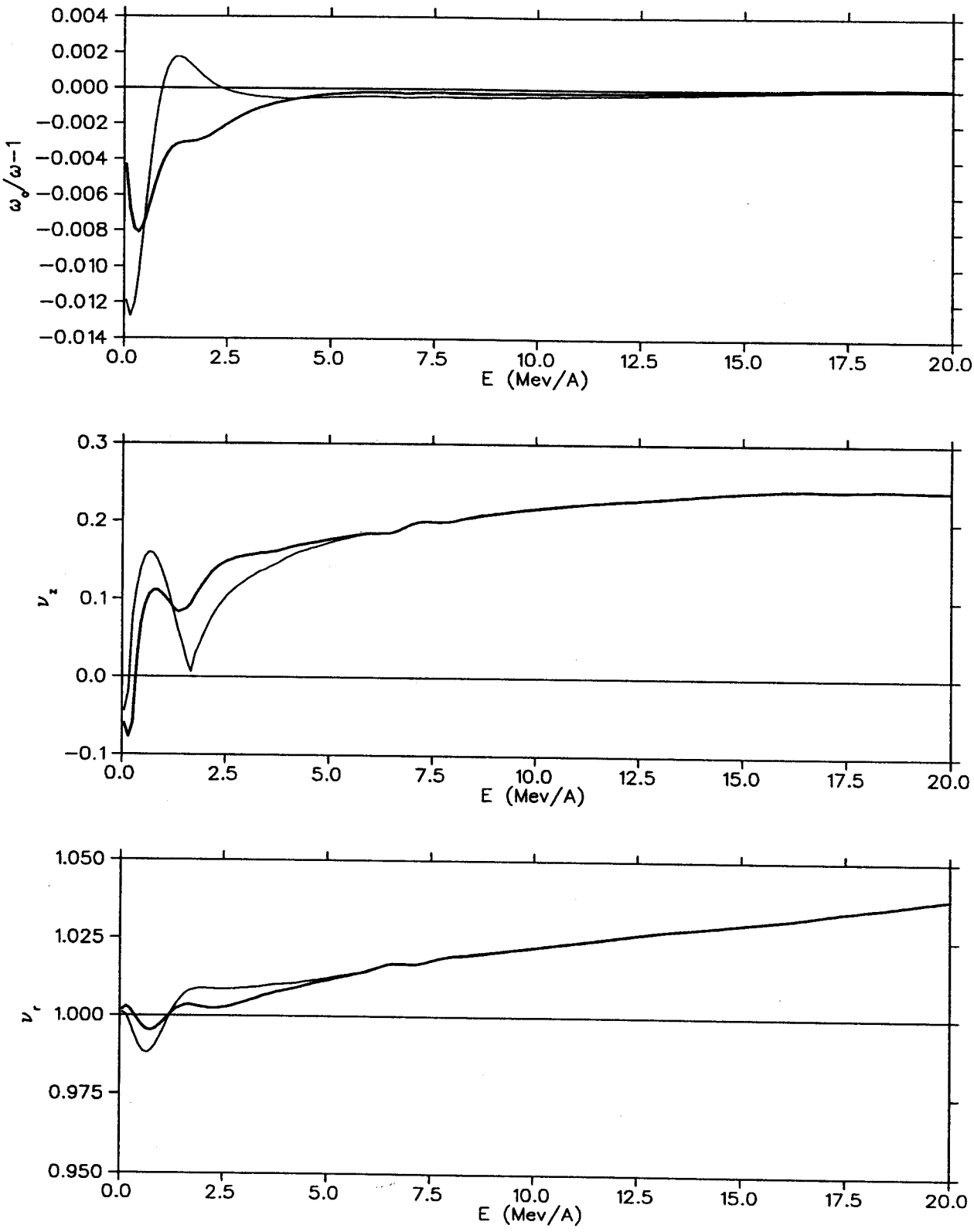

Figure 6.7: The same equilibrium orbit properties as in figure 6.5 rescaled to expand the central region. Properties of the mapped field are plotted with the fine line and those of the modified field are drawn with the double weight line.

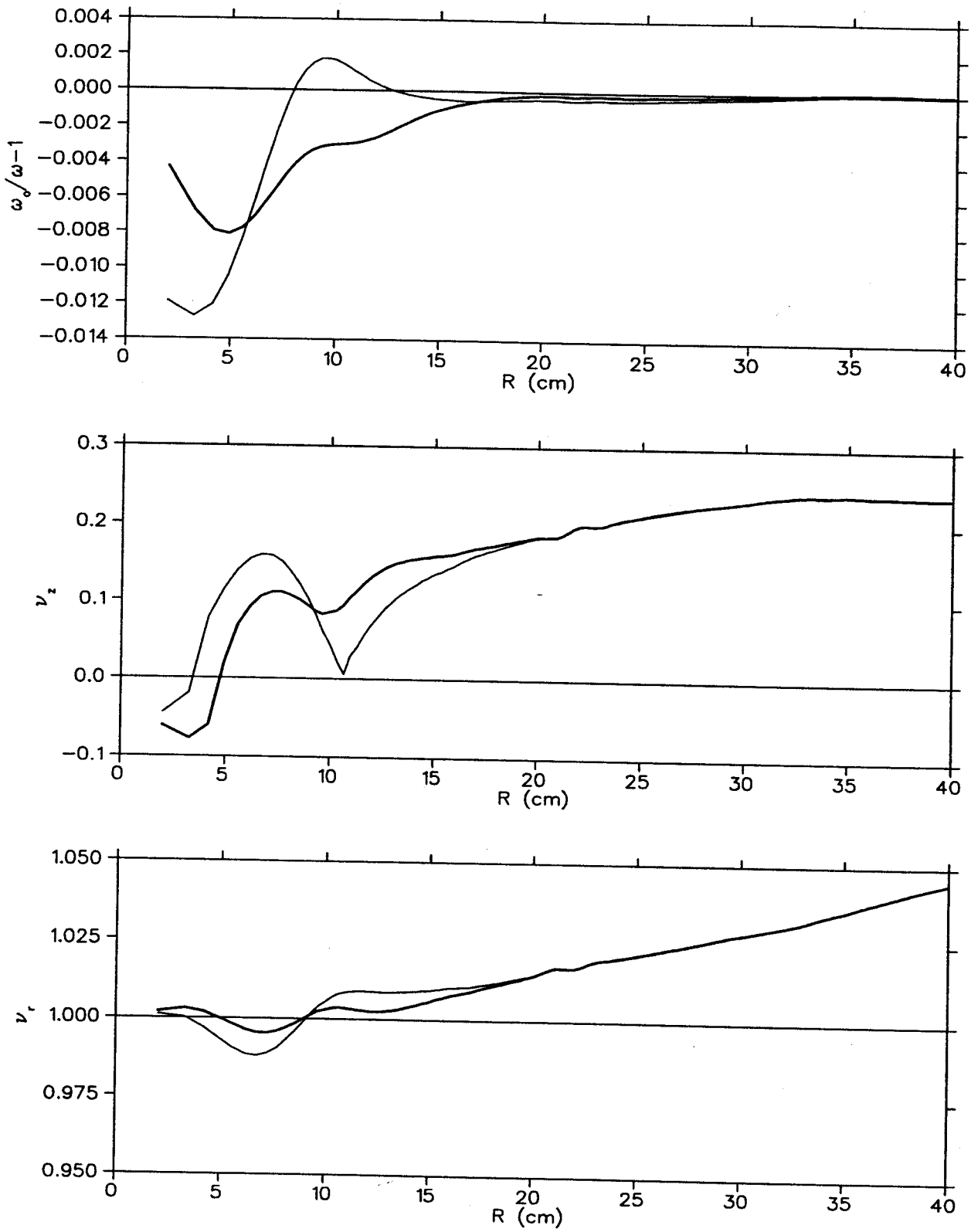

Figure 6.8: The same equilibrium orbit properties as in figure 6.6 rescaled to expand the central region. Properties of the mapped field are plotted with the fine line and those of modified field are drawn with the double weight line.

6.3 Electric Field Computations of the C235

6.3.1 Geometry

Electric fields were computed using the relaxation code RELAX3D [26] from TRIUMF. The NSCL's version of RELAX3D is compiled with an NSCL geometry defining subroutine which allows objects of a given potential to be defined by a perimeter of straight lines and arcs of circles which are parallel to the median plane. Axial tapers such as the slope in the dees and counter dees are represented as a series of steps. All other features may be entered directly from the coordinates in the blueprints and the program chooses the points in a rectilinear grid that most nearly approximate each shape. The geometry installed in the machine in Boston has only three differences from the blueprints that were considered important enough to include in the electric field map:

- The puller has been modified with an extension that lengthens the drift that the particles experience after the first accelerating gap. This drift has a critical effect on the starting phase of the beam.

- The puller tunnel has been widened at one corner. This has a minor effect on electric field penetration into the puller tunnel, and hence on the effective drift length of the puller tunnel.

- The outer post on the counter dee immediately downstream from the puller has had one corner filed to make more room for the beam.

During our August 1997 visit to Boston we examined tolerances in the positioning of the counter dees and the alignment of the central region electrodes relative to the rest of the machine. All such mechanical errors were deemed minor relative to the precision of the grid used for the electric field maps. Thus, only the three intentional

modifications to the initial design that are described above were included in the final calculation of the electric field.

The geometry that is used for the RELAX3D calculation is shown in figures 6.9 and 6.10. Electric fields were calculated for square sections of the machine of several different sizes. The parameters of each relaxation grid are listed in Table 6.1. The largest map uses Neumann boundary conditions at the edges. Each subsequent smaller map uses edge boundary conditions that are interpolated from the previous map. Intermediate maps (not shown in the table) were generated during the relaxation process so that the grid spacing was cut by no more than a factor of two at each stage.

Table 6.1: Parameters of the electric field maps used in Z3CYCLONE.

Name	edge	Grid Spacing			# of grid points		
		hx	hy	hz	Nx	Ny	Nz
E16in.rlx	32"	0.160"	0.160"	.019685" (.5mm)	201	201	25
E8in.rlx	16"	0.080"	0.080"	.019685"	201	201	25
E2in.rlx	4"	0.020"	0.020"	.019685"	201	201	25
Ep25in.rlx	0.5"	0.025"	0.025"	.019685"	201	201	25

6.3.2 The Radial Voltage Gradient

The dee voltage of the C235 has a strong dependence on radius. This has been investigated by IBA resulting in an empirical formula to describe the voltage as a function of radius along each gap (Figure 6.11). During the first 50 cm the gaps on either side of the dee have the same voltage drop and this is taken to represent the potential of the entire dee at that radius.

With the IBA voltage formula we were able to include the voltage gradient in

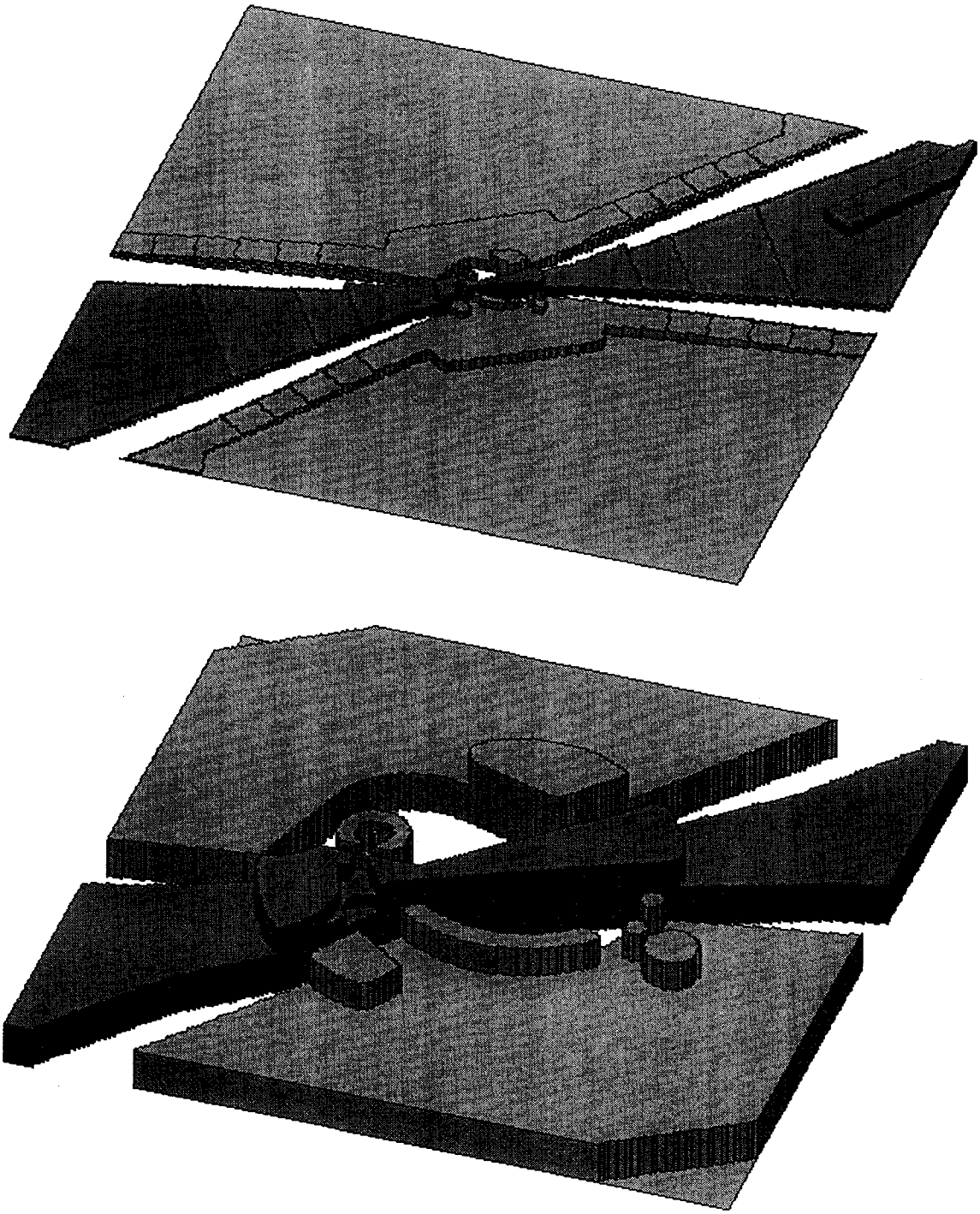

Figure 6.9: The geometry used to calculate electric fields for orbit tracking in the central region. The upper map is 16"×16" (40.64×40.64 cm) and the lower map is 4"×4" (10.16×10.16 cm). Only the half below the median plane is modeled and a symmetry condition is imposed at the median plane. In each case the dark object is the pair of dees joined by the 'RF bridge.' The lighter color indicates the grounded 'counter-dees.' The geometries are oriented so that the beam rotates counterclockwise. A 'vertical slicer,' used during commissioning to remove unwanted beam, can be seen at the right side of the upper geometry. An adjustable set of 'phase pins' with a 1 mm radial gap appears to the lower right of the center of the lower map. Both the vertical slicer and the phase pins are removable.

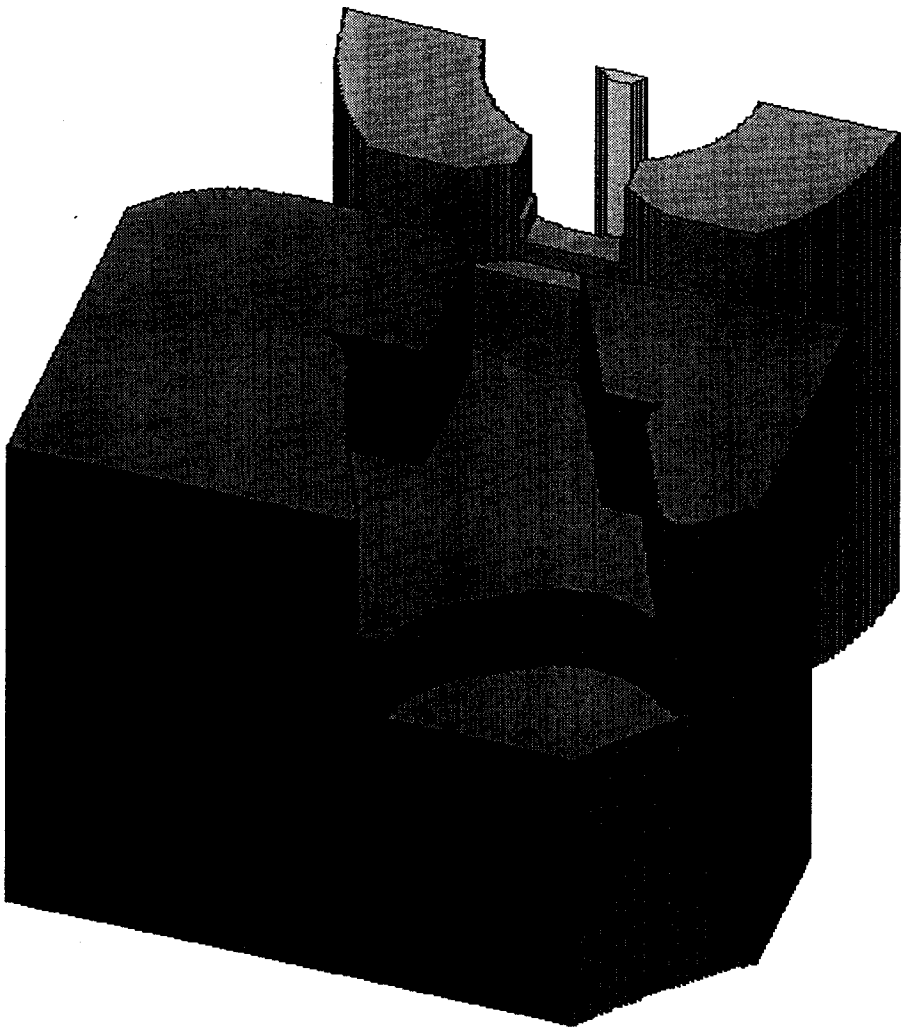

Figure 6.10: The geometry used to calculate the electric field in the source-to-puller gap. The dark object in front is a section of the puller. The lighter object behind it is the grounded chimney. The map is 0.5"×0.5" (1.27×1.27 cm) at the median plane and 0.472" (1.2 cm) deep. The system is rotated so that the reader is looking through the puller at the face of the chimney. The thin vertical object at the axis of the chimney is the 'image-electrode' used to produce an adjustable zero volt equipotential surface in the mouth of the chimney to use as a nominal plasma boundary. The chimney shown here was the one installed at the beginning of the study. Later it was replaced by a chimney with a smaller hole, discussed in section 6.6.

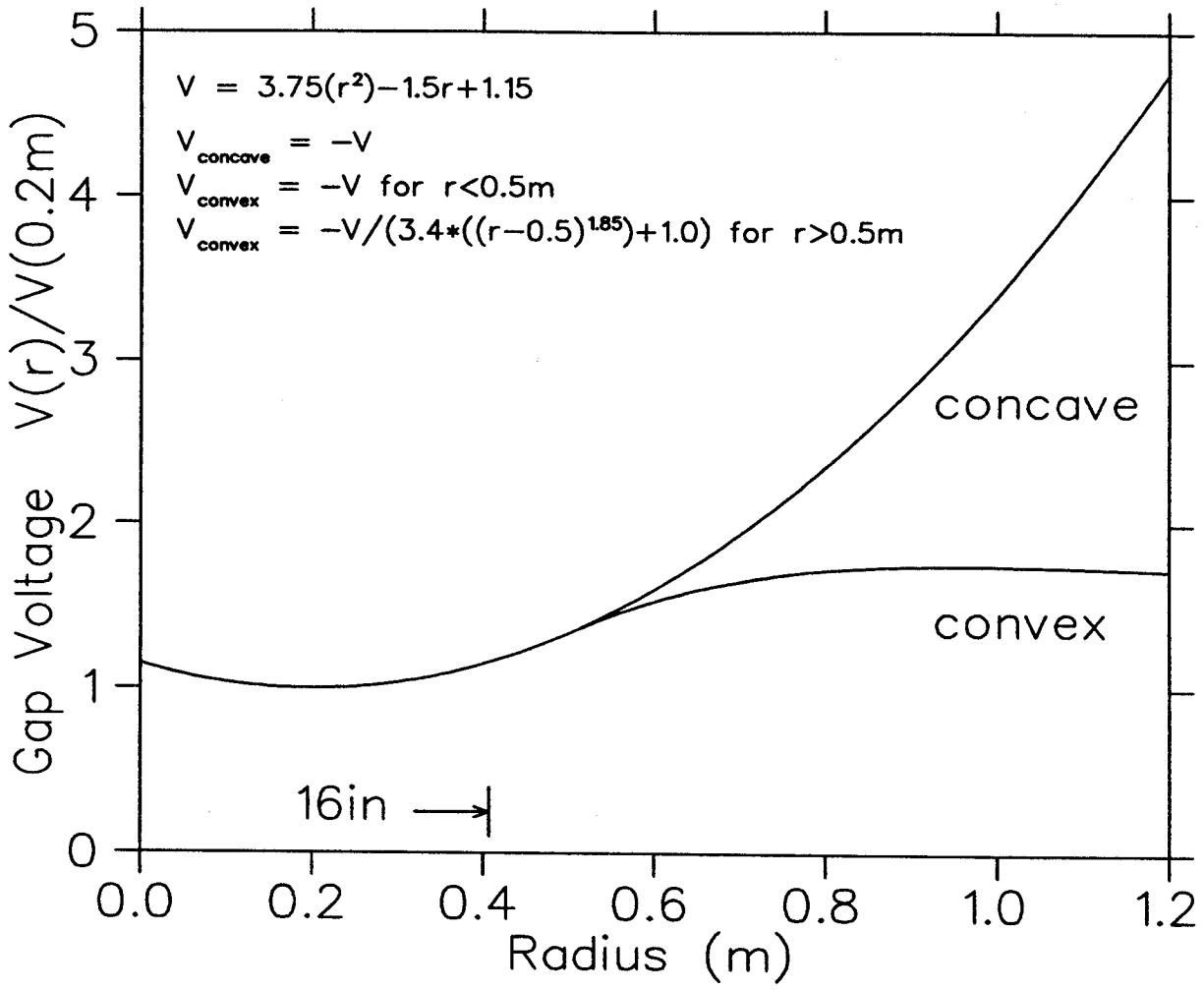

Figure 6.11: The form of the radial voltage gradient on the dees provided by IBA. The largest electric field map used in the MSU orbit studies extends to a radius of 16" (0.4064 m).

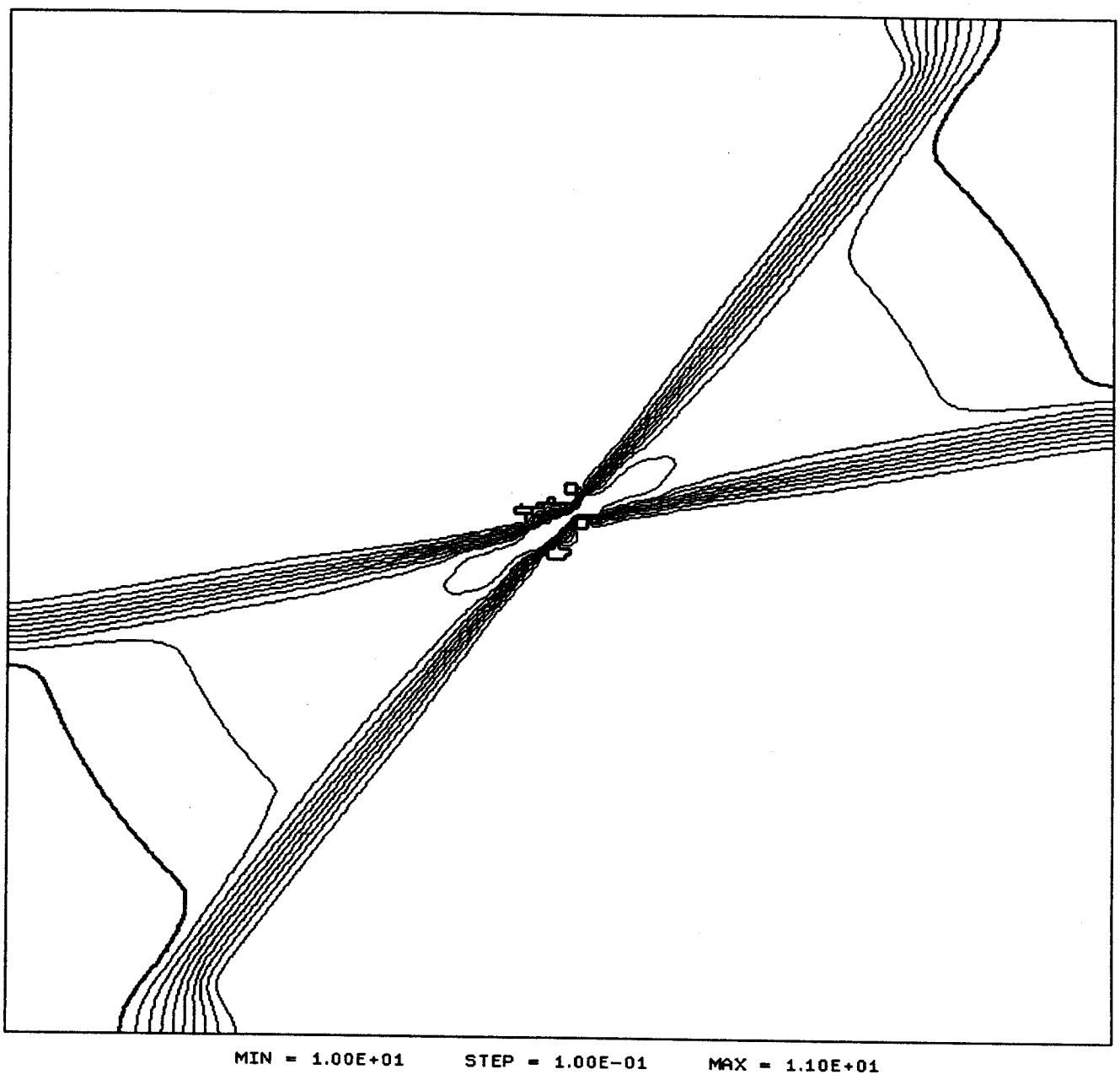

Figure 6.12: The 32"×32" (81.28×81.28 cm) electric field map (E16IN.RLX) with the voltage gradient effect included. Each contour represents 10% of the peak dee voltage at $r = 0$ cm. The posts on the RF-bridge do not appear because their perimeters no longer correspond to an equipotential surface. The effect of the vertical slicer can be seen as a sharpened corner in the 90% contour at the lower left. Distortions in the equipotential due to the Neumann boundary condition are evident at the lower left and upper right. (This part of the field is not used in the orbit calculations.)

the electric field maps. In order to do this each field map was first initialized by RELAX3D with the entire dee at a uniform potential. The unrelaxed field map was then output from RELAX3D and fed to a dedicated program named VGRAD which adjusts the fixed potential at each non-grounded surface point (i.e. every point on the dees) according to the formula for V(r). (If electric fields were needed beyond 50 cm the algorithm would need to be revised to account for the differing potential on each side of the dee.) The new field map was then input to RELAX3D and the relaxation process proceeded normally. The new technique did not cause any convergence problems. The results are shown in Figure 6.12.

6.3.3 The Plasma Boundary

Protons are started with an initial energy of 10 eV directly on the nominal plasma boundary, where the plasma boundary itself is modeled using the method described in section 3.5. A typical source-to-puller field map is shown in Figure 6.13. The plasma boundary may be manipulated to be convex, approximately flat, or concave depending on the potential chosen for the image electrode. The implications of using different shapes for the plasma boundary is a topic of ongoing research at the NSCL, and is discussed further in Chapter 3 and Section 6.6. For the majority of orbit calculations in this chapter we have chosen a boundary which is flat at the median plane as this is believed to introduce the fewest unknown factors to the calculation.

6.4 Calibration of the Dee Voltage

The precise dee voltage produced by the resonator is of interest to IBA in order to better understand the performance of their overall rf system. It is also essential to

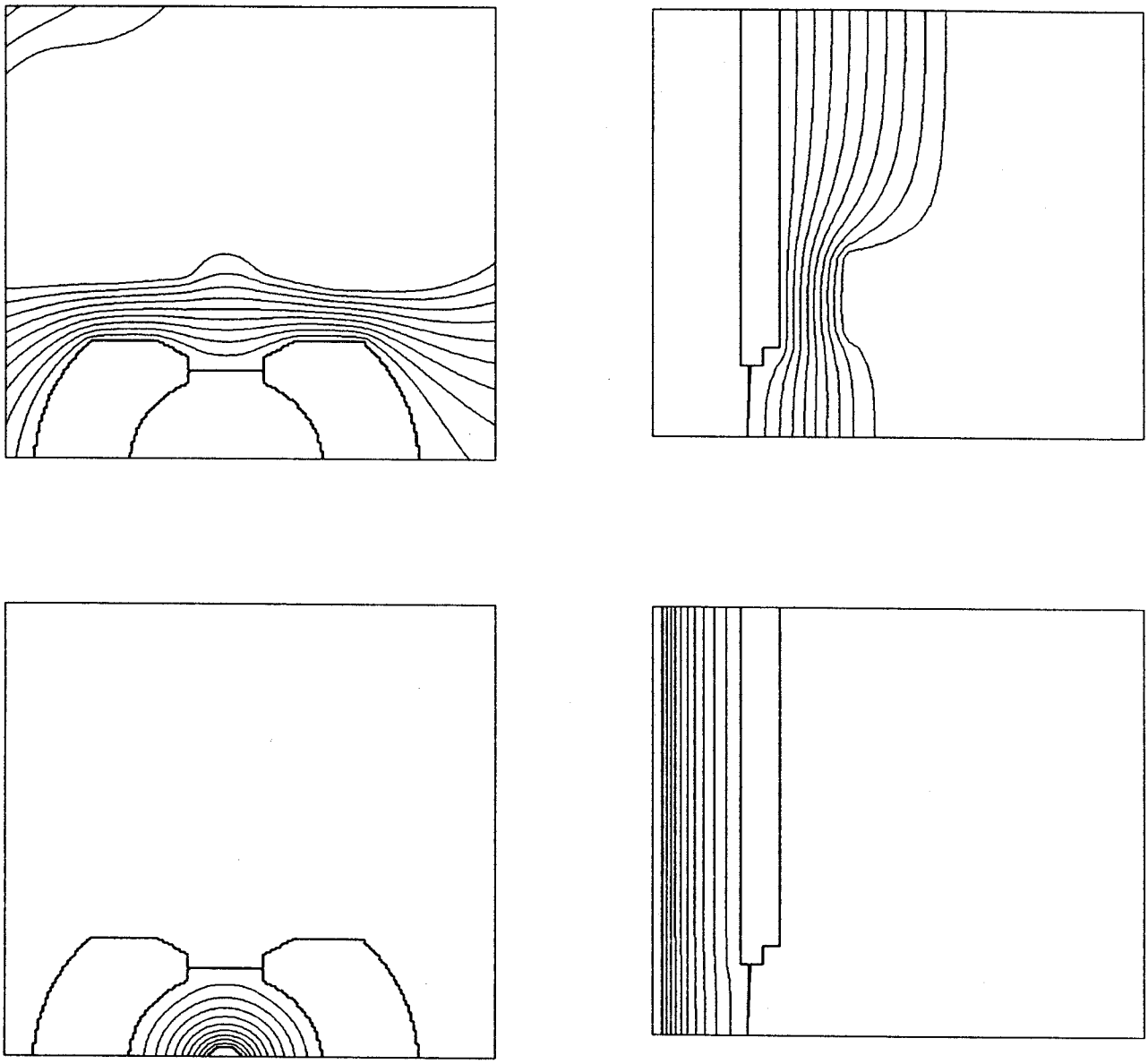

Figure 6.13: Median plane (left) and vertical cross section (right) of the electric field in the source-to-puller gap, using an 'image electrode' to produce an artificial plasma boundary with a smooth voltage gradient. Here the image electrode voltage is equal and opposite to the $r = 0$ dee voltage. The perimeter of the puller does not appear because it is not an equipotential surface (see section 3.2). Each contour represents 10% of the $r = 0$ dee voltage. The upper plots show voltage contours between ground and dee voltage. The lower plots show voltage contours between 'image electrode' voltage and ground. The ion source chimney is 1 cm in diameter.

know the dee voltage in order to accurately calculate orbit trajectories which are the focus of this project.

X-ray end-point measurements have determined that the peak dee voltage at the center of the machine is between 60 kV and 65 kV. The X-ray technique is hampered by unwanted signals from the region beyond a radius of 40 cm where the dee voltage exceeds the value at the center and rises to nearly 300 kV (as shown in Figure 6.11). We have tried to make a more precise calibration of the dee voltage by comparing orbit calculations for a variety of dee voltages to experimental data.

We have tried two methods of comparison. In the first we seek the lowest RF voltage which allows any beam to reach the beam probe at a given radius. In the second we search for the initial conditions (one of which is of course the dee voltage,) which would result in an orbit array matching an experimental probe pattern consisting of roughly fifty discernible turns from a radius of 7 cm to 25 cm.

6.4.1 Finding the Minimum Voltage to Extract Beam from the Central Region

Early in the project we attempted to quantify the minimum dee voltage at which the beam could reach a beam probe located at a radius of 19 cm (where a set of experimental data had been taken by the IBA team). We ran individual rays for a variety of dee voltages V_{dee} and starting times τ_0, and noted which rays were lost before $r = 19$ cm, where τ_0 is the RF time at which each particle left the chimney (the 'starting time') where τ =270° corresponds to the peak of the voltage wave. (The 'starting time' τ_0 should not be confused with the phase ϕ, which is equivalent to the RF time τ (or $\tau - 180°$) at the center of a dee (or hill.)) All rays were run from the center of the plasma boundary and were pointed directly away from the center of

the chimney with an initial energy of 10 eV. Radial and axial phase spaces were not explored. Also, it should be noted that at this early stage the radial voltage gradient (a 15% drop between the center and 20 cm) was not yet included in our central region model. The points of the parameter space that were tested were spaced at 1 kV of voltage and 5° of RF time apart.

The results are plotted in Figure 6.14. We see that beam from a roughly triangular region of the V_{dee}-τ_0 parameter space survives and reaches R=19 cm. The upper left corner of the parameter space (voltage too low and starting time too late) fails to clear the central region electrodes. The lower portion of the parameter space falls out of phase with the RF before reaching 19 cm. The minimum voltage surviving ray corresponded to a dee voltage of 52 kV.

For comparison an experiment was performed in Boston where the dee voltage was lowered from its typical operating value while the beam current was observed on a probe at 19 cm. The dee voltage needed to be lowered approximately 10 kV from the standard operating conditions to reach a voltage where the beam died out, indicating that the typical operating voltage is near 62 kV. This value is in good agreement with the X-ray measurements.

6.4.2 Using Z3CYCLONE to Match Data from the Radial Probe

The previous experiment calibrates the dee voltage at a single point 10 kV below the region of interest. In order to calibrate the RF voltmeter directly at the operating dee voltage we generated orbit patterns with Z3CYCLONE for a variety of voltages in order to see which voltage gave the best fit to data from the radial beam probe. In order to obtain good agreement with the probe data it is necessary to consider

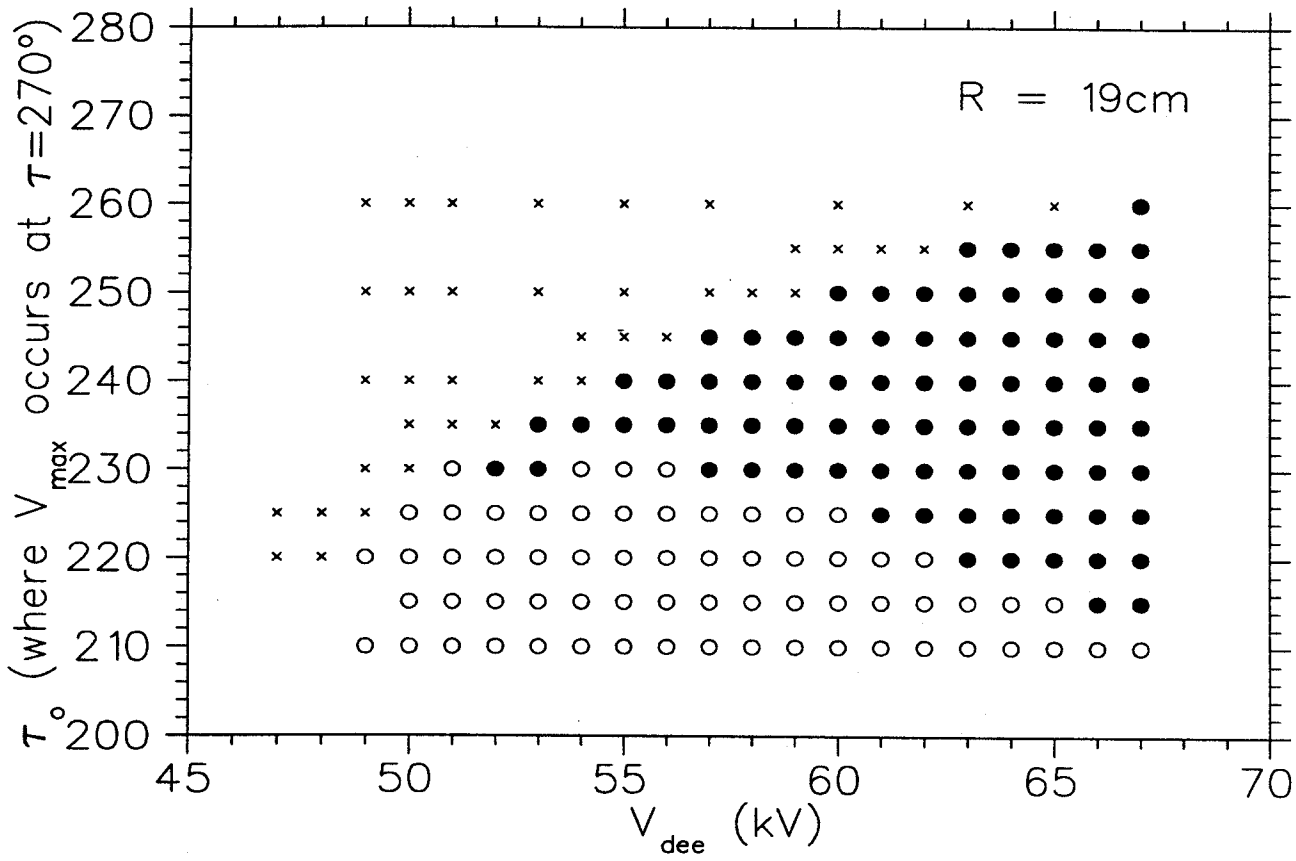

Figure 6.14: The two dimensional parameter space of dee voltage and starting time (RF time at which the particle leaves the plasma) combinations which allow beam to reach a radius of 19 cm. Parameter pairs marked by an 'X' fail to clear the central region. Pairs marked with an open circle are lost due to phase slip before reaching 19 cm. The leftmost black dot represents the minimum dee voltage for which beam is predicted to reach r=19 cm.

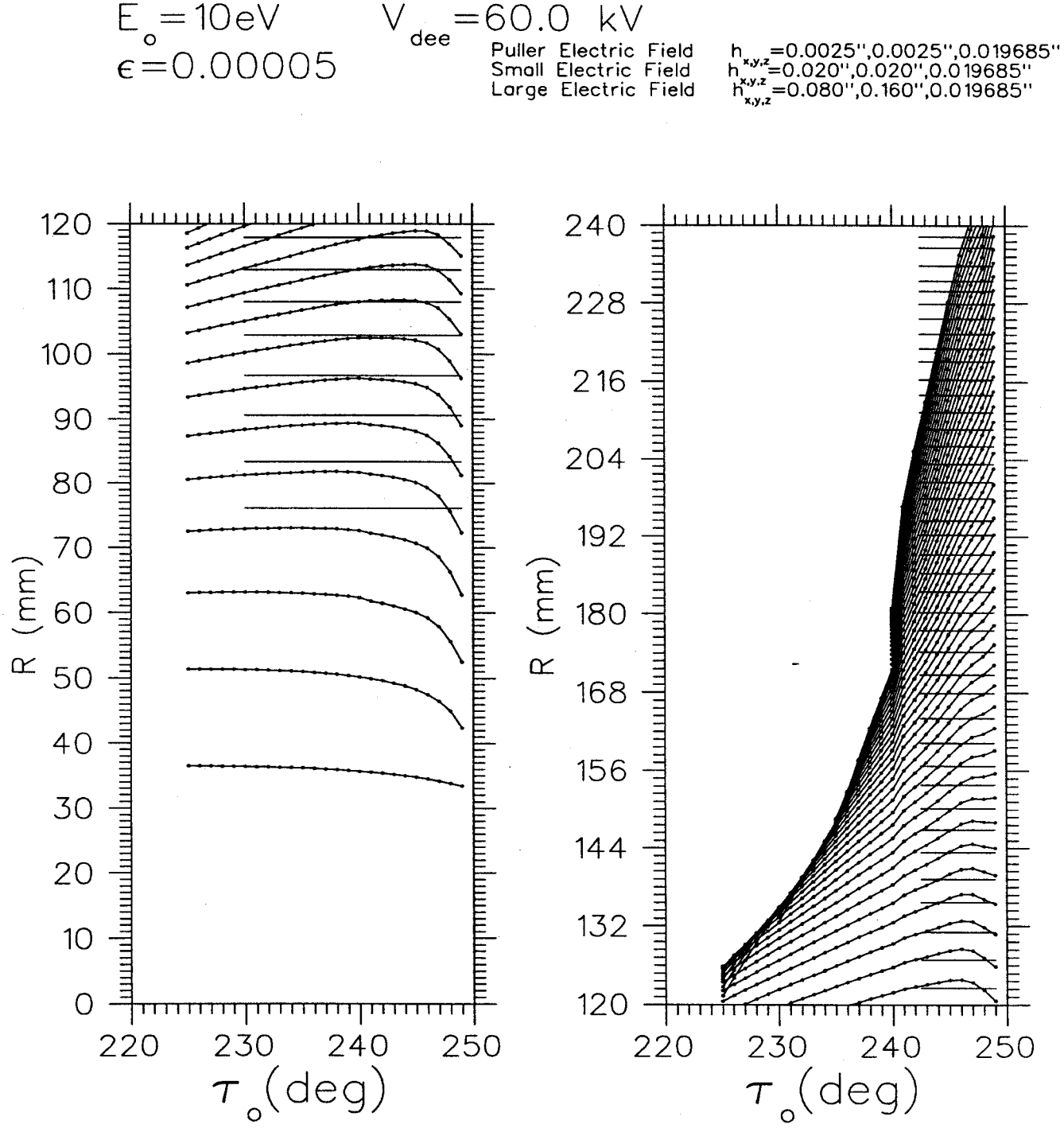

Figure 6.15: Calculated radial position as a function of starting time for the first 60 turns (dots) and radial position of experimental current peaks (bars). The peak radial density can be seen to shift from early to late values of τ_0 as the turn number increases. Rays starting later than τ_0=249° failed to clear the central region posts.

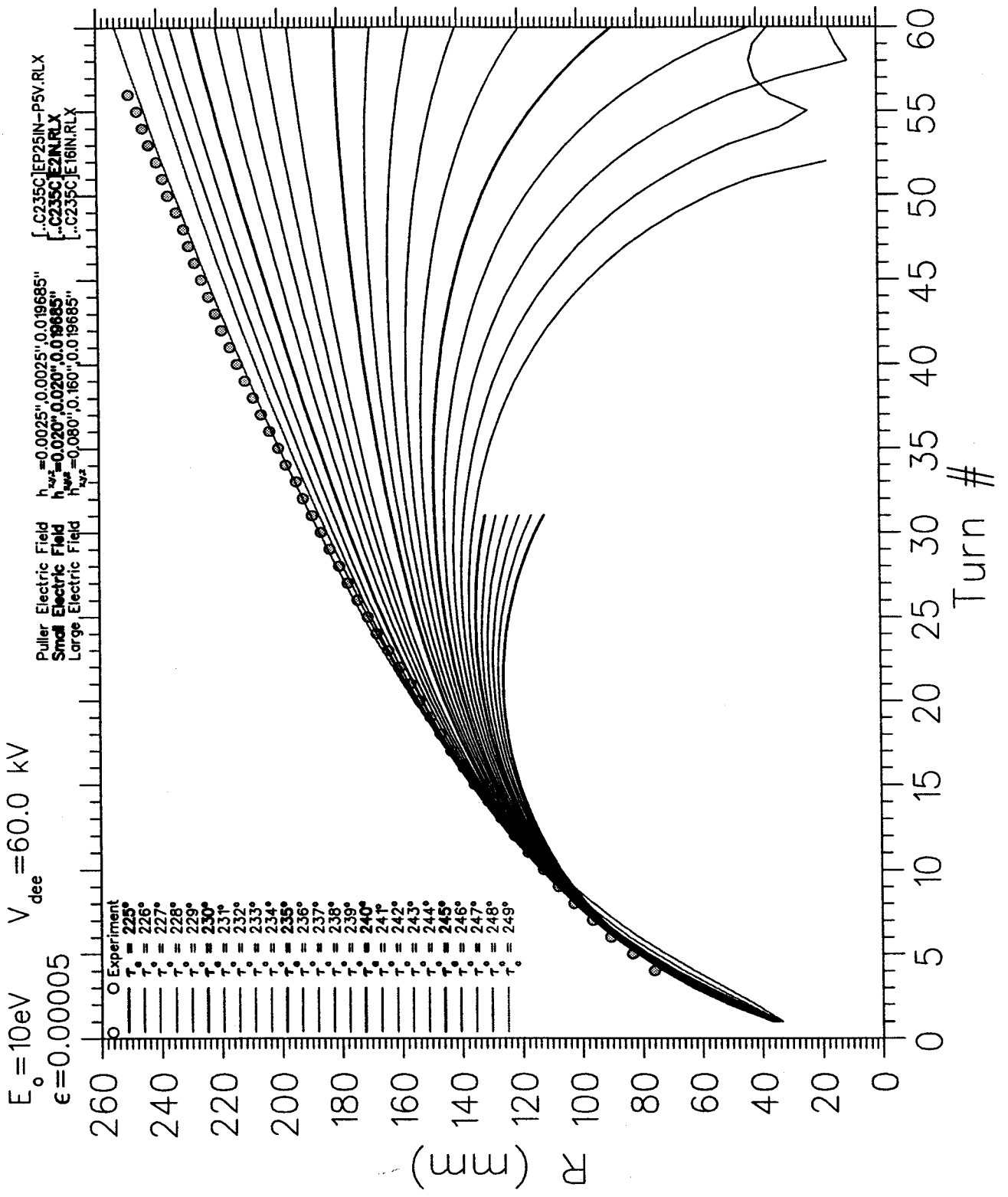

Figure 6.16: The data and calculations from Figure 6.15 recast to better compare the calculated position of peak current (see text) to the experimental data.

that the beam is made of a range of central rays with different starting times (and their associated phase spaces.) Snyder demonstrated computationally that the peak current density (the quantity measured by the differential probe) in each turn is associated with different starting times from one turn to the next [67]. Figure 6.15 shows a computation similar to Snyder's for the case of the C235. The radial positions of a set of central rays are plotted each time each ray crosses the azimuth of the beam probe. The highest radial current density (corresponding to the peaks in the experimental turn pattern) occurs at the τ_o giving the largest radius for each turn. We see that during the first 23 turns the peak current density shifts from the position of the earliest central ray studied to that of the latest which cleared the central region. The phase pins were not included in this calculation.

Snyder used this method to choose the appropriate central ray to compare to each of seven peaks in a set of probe data for the NSCL K500 and thereby calibrated the dee voltage to better than 2 kV. IBA provided us with a turn pattern measured on June 27, 1997, that showed approximately 50 turns with good separation and clearly defined peaks. The radii of the peaks are plotted as bars in Figure 6.15. To more easily interpret the data we plot radius as a function of turn number for each of the considered starting times and for the experimental data in Figure 6.16. In this case, turn number one is defined as the first crossing of the beam probe azimuth. Because the experimental data contains no information about the beam before a radius of 7 cm, the initial turn number for the experimental data must be taken as a free parameter to be fit to the calculated curve. As in Figure 6.15, the ray with the maximum radius represents the expected radius of a peak in the probe data. Therefore the upper edge of the collection of central ray paths is compared to the experimental data. The analysis of Figure 6.16 was repeated for 0.5 kV steps from 59 kV to 61 kV. A visual inspection indicated a best fit at either 60 kV or 60.5 kV.

After the calibration described above minor corrections were made in the electric field map. The source-puller gap geometry and the position of the accelerating gaps beyond 77 mm were adjusted to match additional drawings and measurements of the system as built that had not previously been communicated to NSCL. The effect of the harmonic coils is also not yet accounted for in this calculation. Subsequent work has found little influence of the source-puller gap geometry on the turn patterns. The corrections to the dee and counter dee geometries caused slight changes in the energy gain as a function of radius and also changes in the orbit centering. As a result the peak central ray moved outward about 2 mm near turn 30 and inward about 1 mm near turn 56. The contribution of the harmonic centering coils was then added by making an aircore calculation of their magnetic contribution and adding it to the previous magnetic field. The field of the harmonic coils alone is plotted in figures 6.17 and 6.18. The inclusion of the harmonic coils added a displacement of a similar magnitude to the electric field modifications but in the opposite direction, resulting in an r vs Turn Number curve that was not substantially different from the one presented here.

The quality of the match enhanced confidence in the overall cyclotron model, and added to the evidence that the true central dee voltage of the C235 is near 60 kV. Work on a more precise voltage calibration has been deferred until magnetic field data and beam probe data are available for the recently modified magnet configuration.

6.4.3 Conclusion

The dee voltage calibration study of the C235 represents work in progress; the results presented here serve to support the experimental measurement of a central dee voltage between 60 kV and 65 kV, with the suggestion that the true number lies nearer

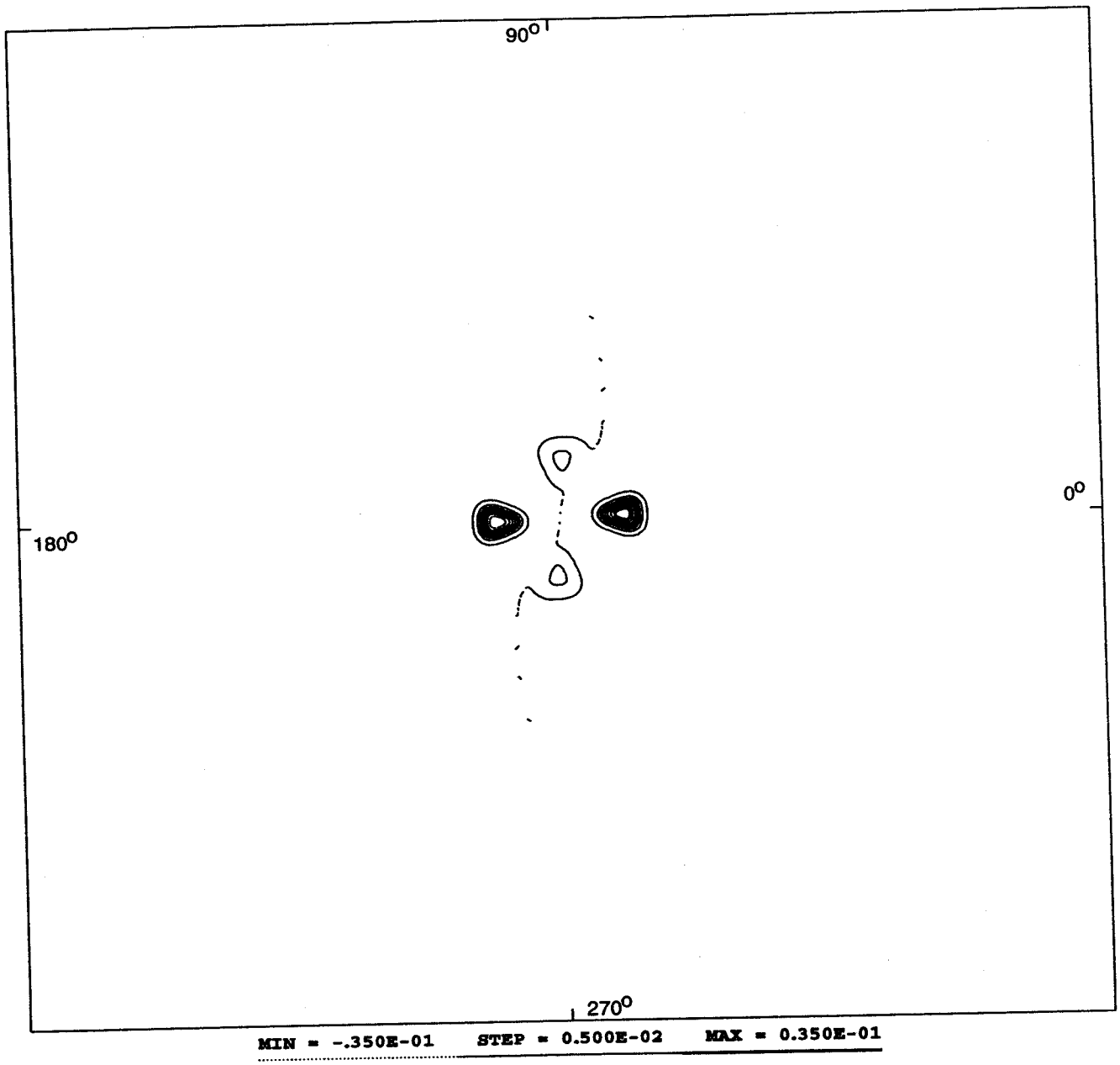

Figure 6.17: Contour plot of the magnetic contribution of the harmonic coils as they were set on June 27, 1997. Each coil is triangular in shape to make use of the limited space near the central region. The coils are set to -1.0 amp in the $H_{1,3}$ set and 0.16 amp in the $H_{2,4}$ set. Contours are spaced 5 Gauss apart with the dotted contour at -35 G and the double weight contour at 35 G. Due to mechanical constraints the four coils are displaced several millimeters from perfect four-fold symmetry. The system retains two-fold symmetry. The frame is 2.4 m square

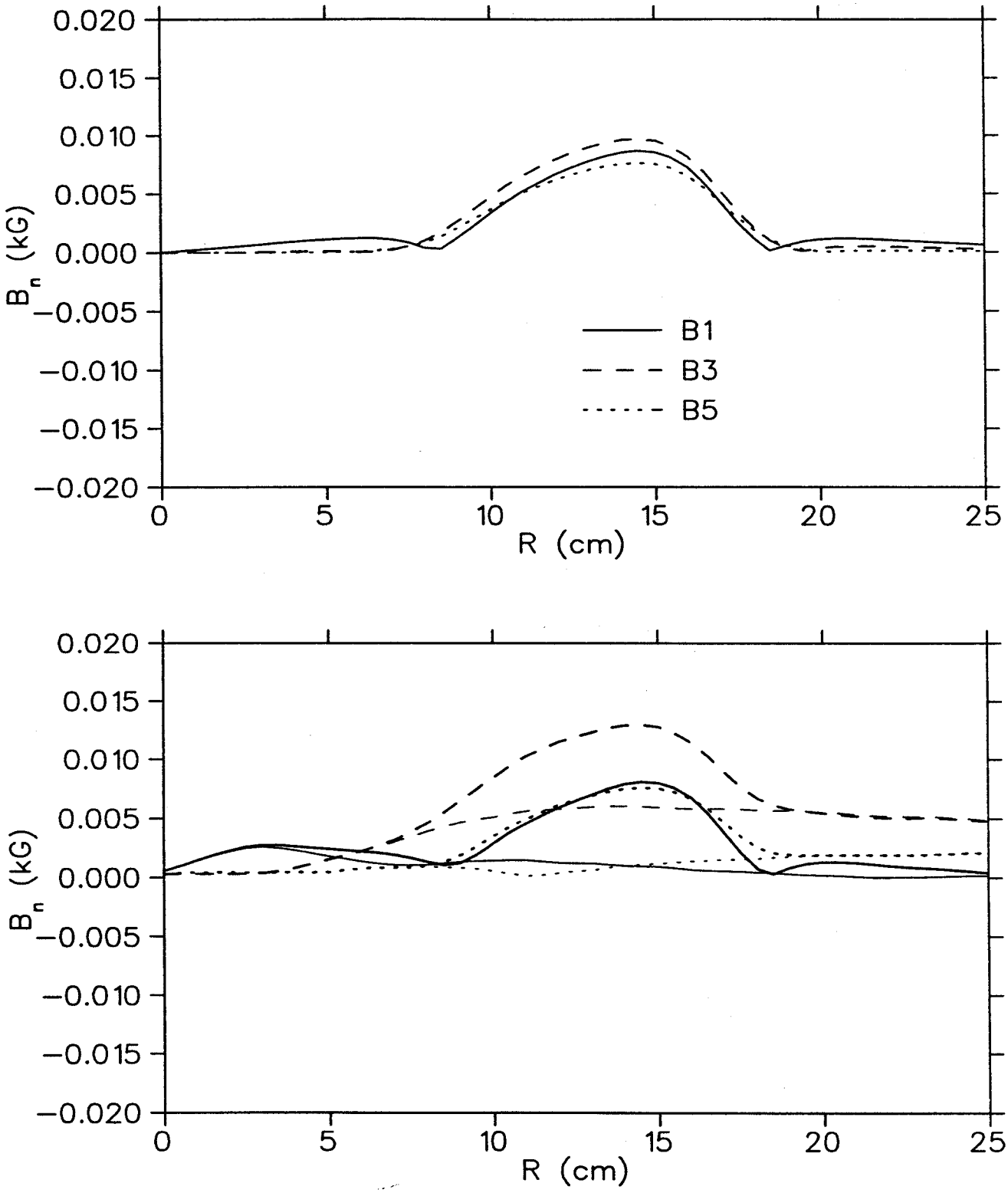

Figure 6.18: Top: first few harmonic components of the field produced by the harmonic coils with the same settings as in Figure 6.17. Even components are null because the system has two-fold symmetry. Bottom: First few odd harmonic components of the total magnetic field before (fine line) and after (double weight line) adding in the effect of the harmonic coils.

to 60 kV. The 60 kV figure was adopted for most subsequent orbit studies presented in this chapter.

6.5 Accelerated Orbit Properties

Because of complicated magnetic features such as the gradient corrector, the Z3CYCLONE program was modified to accept a full 360° magnetic field map, rather than just a 90° map of one 'average' sector. It was then possible to use the same field for all orbit studies from the source to extraction.

A plot of the first few turns for a range of starting times is shown in Figure 6.19. Based on the early orbit behavior the NSCL team concluded that there were no problems with the arrangement of posts in the central region. Therefore, the only modification that was recommended was to change the design of the ion source to reduce the size of an unusually large chimney hole. The effect of this modification is discussed further in section 6.6.1.

6.6 Studies of Alternate Source-to-Puller Geometries

During the course of this study a number of different source-to-puller configurations were tested. Changes included different plasma-boundary positions, different chimney designs, and modifications to the geometry of the puller.

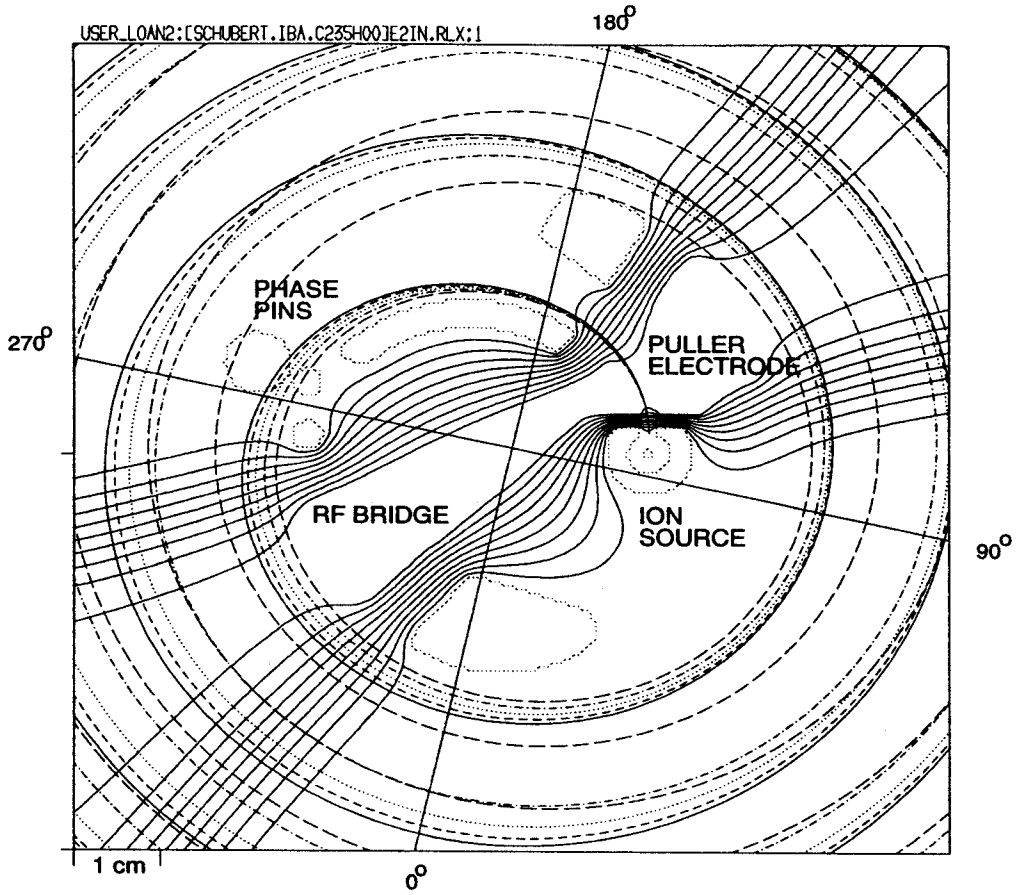

Figure 6.19: Central ray ion orbits for starting times from τ_0 =247° to 259° where τ_0 =259° is the latest ray that clears the central region if the phase pins are not installed. The region shown is 4" square. This calculation uses the updated electric field map with the original chimney. Minor adjustments to the shape of the puller have shifted all starting times 10° relative to the system used for Figure 6.16.

6.6.1 Comparison of Two Chimney Designs

The original chimney installed in the cyclotron is shown in the left side of figures 6.20 and 6.21. The width of the hole should give rise to a large radial betatron oscillation which would increase losses in the deflector. In addition, the length of the 'tunnel' that separates the neutral plasma inside the chimney from the electric field of the source-to-puller gap reduces the electric field at the plasma boundary, which should in turn reduce the amount and intrinsic brightness of the ion beam that is extracted.

Because of these concerns a modified chimney with a smaller hole and a thinner chimney wall was constructed. The right side of figures 6.20 and 6.21 shows the modified chimney. The new chimney was installed in mid August, 1997. Computations with the new design did not predict any significant change in the shape or position of the beam. The computer orbit models did, however, require that all central ray starting times be shifted 20° to 30° in order to match the behavior of the previous system.

When the new chimney was installed with the same source-puller gap as the previous chimney, the beam current sharply increased. No quantitative comparison of the two chimney currents is available, however, because, during testing, the source arc current was always turned down when the new chimney was in use to keep the beam current, and secondary radiation, below a tolerable level.

The increase in output current may be, in part, due to central rays starting closer to the peak of the RF wave, but an inspection of the electric field maps calculated in the source-puller region suggests that the increased electric field has a much greater effect than improved timing. Figure 6.21 shows electric fields for the old and new systems where we have set the image electrode voltage to produce a flat plasma boundary in each case. In addition to the shorter effective gap length for the new geometry

(which is the source of the later starting times for equivalent orbits) the new design approximately doubles the electric field at the plasma boundary for any particular time. The new geometry has moved the plasma boundary closer to the puller without moving the chimney face any closer to the puller, thus gaining the same extracted current advantage as moving the source closer to the puller but without increasing the risk of sparking.

6.6.2 Effect of Changing the Source-to-Puller Distance

All of the source-to-puller electric fields in this study have a source-to-puller distance of 1.6 mm, whereas the actual gap in the cyclotron can be adjusted from the control room and many settings have been used. In order to determine the importance of adding this variable to our computer models a brief experiment was performed during the August 1997 visit to Boston.

With the video beam-probe installed in the cyclotron, we selected an image of a single turn near the center of the cyclotron. This beam spot contained complicated structure in both the radial and axial dimensions. While several people watched the beam spot on the video monitor, the operator moved the source to vary the gap from 3.1 mm to 1.6 mm. None of the observers discerned any changes in the appearance of the beam spot apart from the overall change in brightness that presumably reflected the change in overall current.

This experiment suggests that the paths of the central rays (beyond the central region) and their associated phase spaces are largely unaffected by the pathlength of the first accelerating gap. This evidence may be taken to support the hypothesis proposed by Jongen that the dynamics of the first turns are sufficiently complicated as to erase any memory of the phase space at the exit of the first accelerating gap [68].

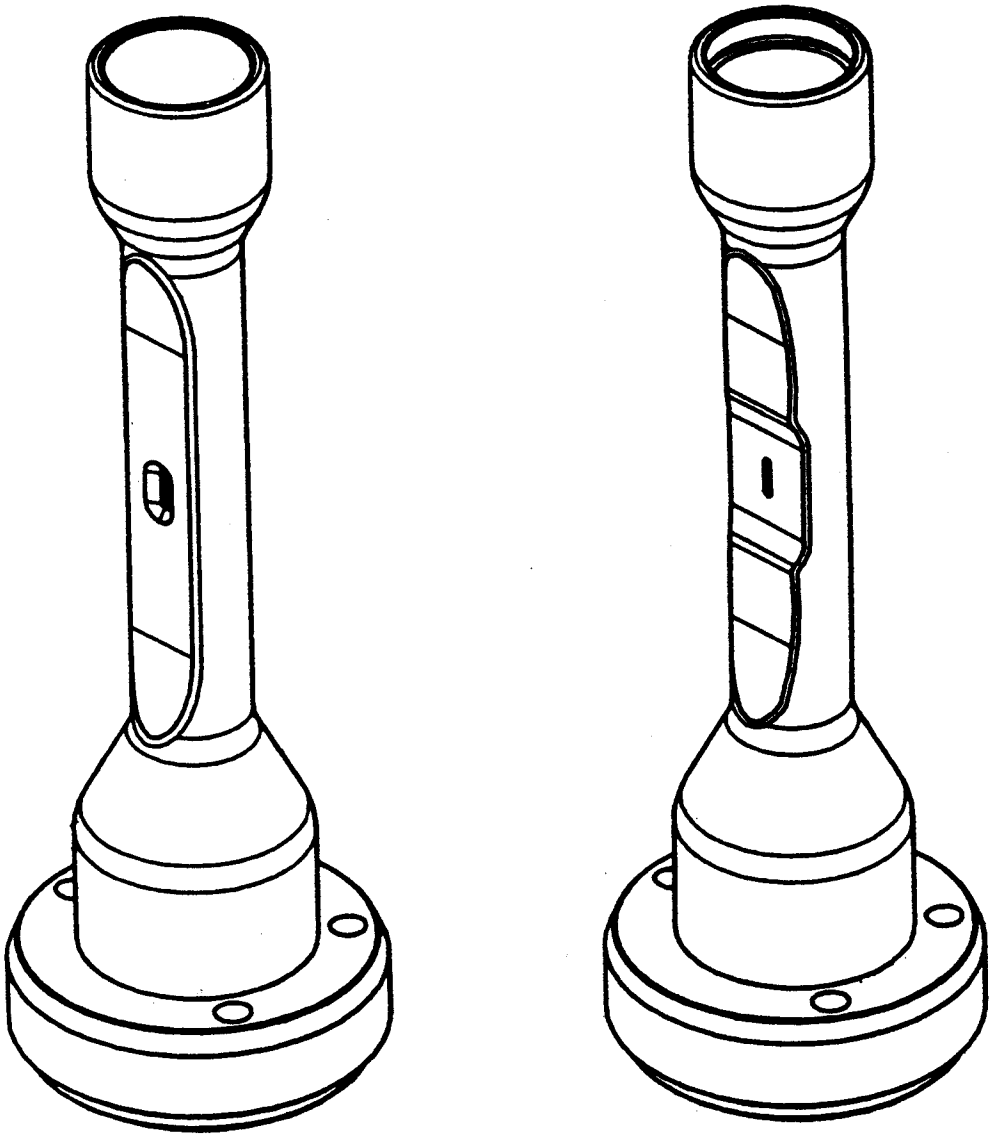

Figure 6.20: The original chimney design (left) with a recessed 2×4 mm hole and the new chimney with a .7×4 mm hole and a thinner wall. (Courtesy of Ion Beam Applications, Louvain-la-Neuve, Belgium.)

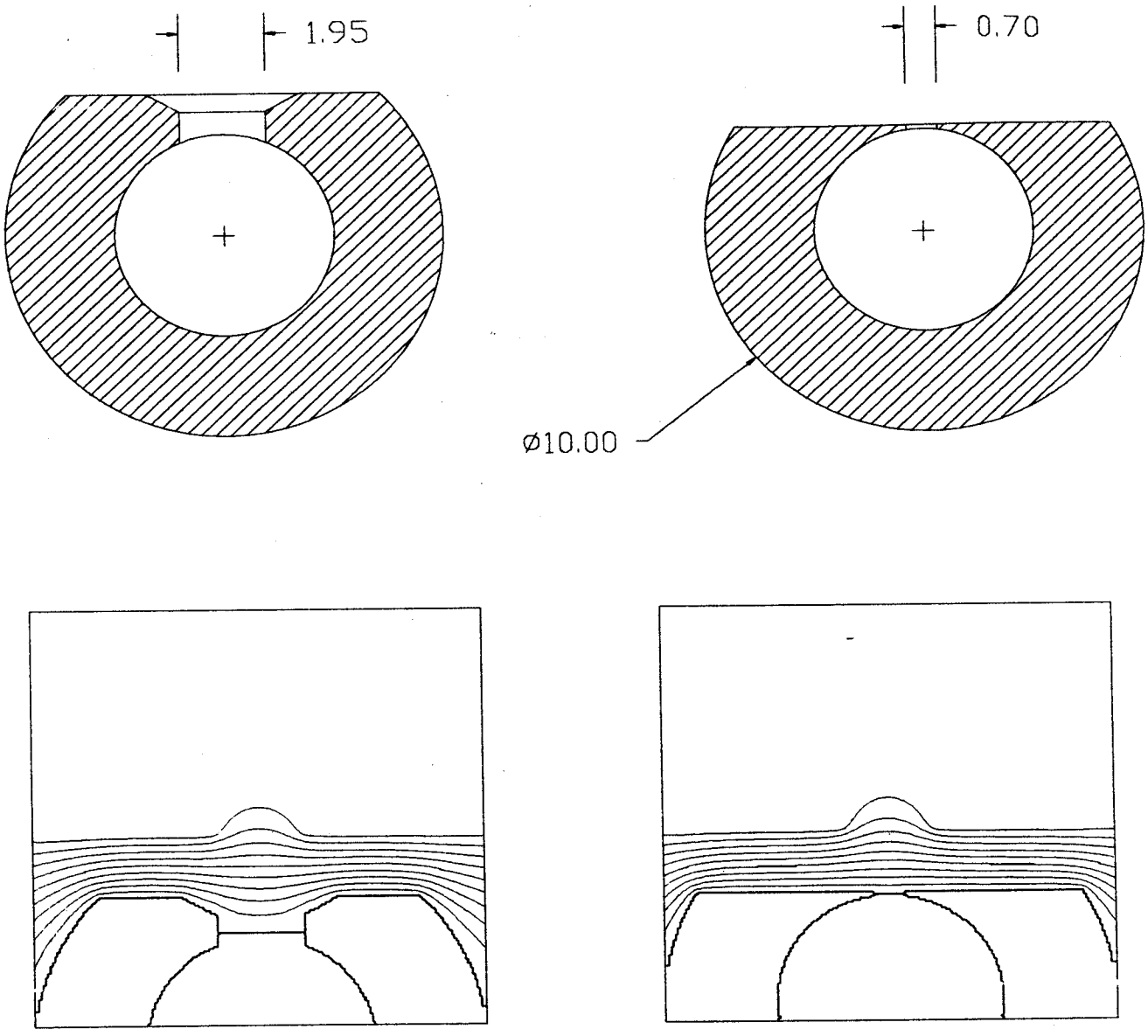

Figure 6.21: Top: median plane cross-section of the original chimney design (left) and the new chimney (right). Measurements are in mm. Bottom: electric field produced in the puller gap (as calculated by RELAX3D) where each chimney is located 1.6 mm from the puller. Notice the relative density of equipotentials at the chimney hole, indicating a stronger electric field for extraction from the new chimney. (Electric field maps are 1 cm square.)

Alternatively this behavior could be explained by our computational experience with other geometric variations (such as changing the plasma boundary shape) in which the peak intensity central ray simply shifts in starting time to compensate for a longer or shorter pathlength in the first gap.

In either case, this evidence suggests that the choice of plasma boundary position, to the extent that it influences the effective gap length, is not critical to orbit calculations. Our computations with different plasma boundaries have usually placed the center of the boundary in a range of a few thousandths of an inch, whereas the experiment described here varied the effective gap length by 60 thousandths of an inch (i.e. a variation greater by an order of magnitude than that allowed in the orbit studies.)

6.6.3 The Effect of Plasma Curvature on Lateral Focusing

The dynamics of the r-p_r phase space in the first accelerating gap were studied briefly for a set of possible plasma boundary shapes. By varying the image electrode voltage we created plasma boundaries with curvatures that were convex, nearly flat, or concave at the median plane.

Figure 6.22 shows a set of orbits starting from different lateral positions along the plasma boundary. We see that a small change in the shape of the plasma boundary can change a well focused set of orbits to an overfocused set of orbits.

Because our knowledge of the true shape of the plasma boundary is still very limited, we restricted most of our early studies to central rays without their surrounding r-p_r phase space.

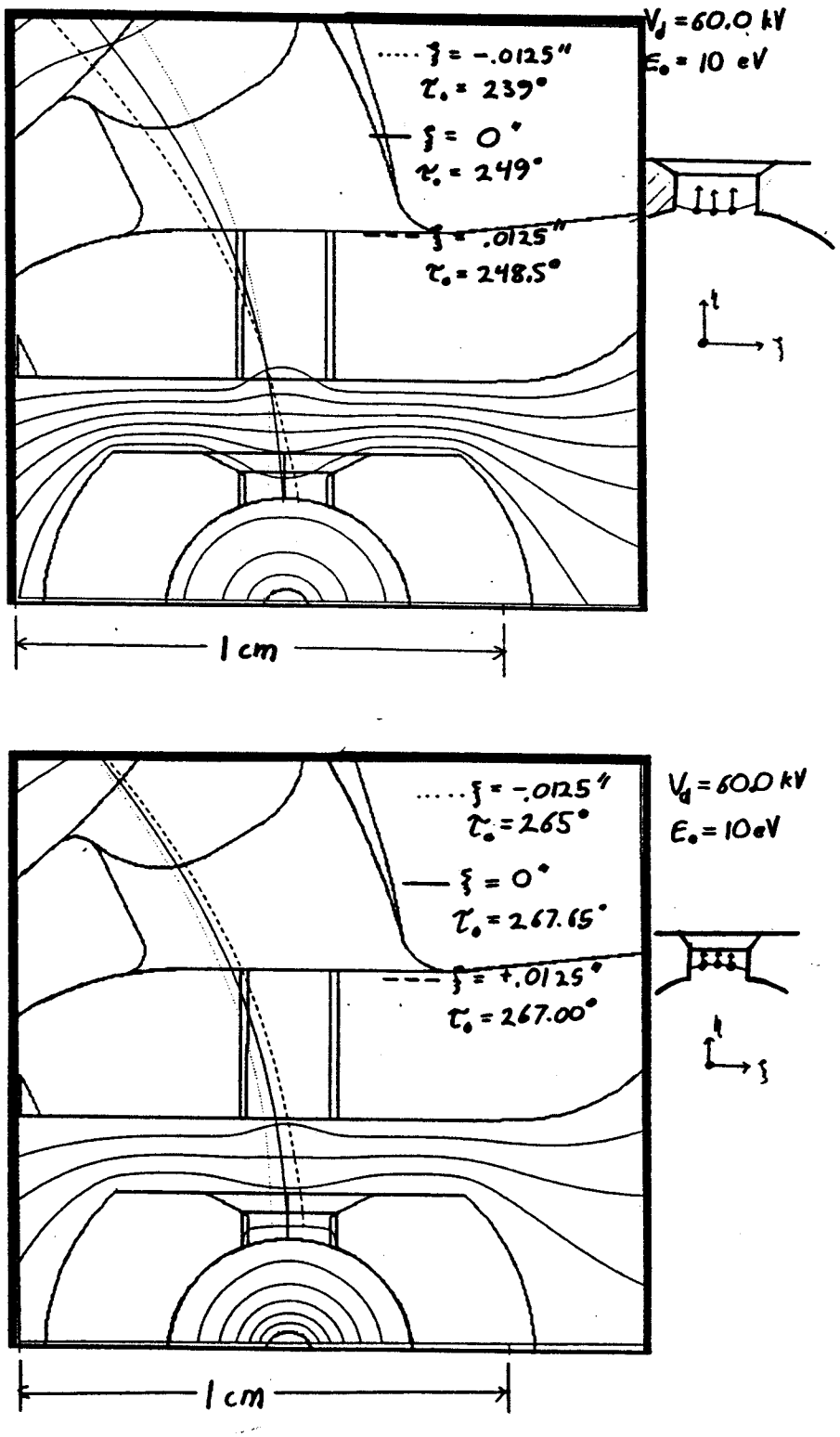

Figure 6.22: Top: lateral overfocusing (from the original source) in the case of a concave plasma boundary. Bottom: better optimized lateral focusing in the case of a convex plasma boundary. (The corner of the puller extension that appears to intersect the orbits is in fact filed away in the actual machine.)

6.7 Recommendations

To further enhance the performance of the cyclotron, and our understanding of its performance, we make the following recommendations.

• Continue to study improved chimney designs.

The results of the modified ion source chimney design have been encouraging, and an even smaller chimney hole is recommended (0.5× 2 mm) since such a hole would still produce more beam than needed and would allow the source to operate in a 'hotter' mode where brightness is likely to be increased. This would then be expected to improve beam transmission through resonances and through the deflector.

• Construct a new magnetic field mapper.

Towards the end of this study discussions began to include the possibility of the construction of a new magnetic field mapper that could operate with all of the RF hardware (and the harmonic coils) installed in the cyclotron. The recent sale of three copies of the Boston cyclotron makes the eventual construction of the new mapper even more attractive. Data from such a mapper would enable us to quantify the accuracy of all of the calculated magnetic field modifications, including the harmonic coil computations, and would take account of the recently added isochronizing shims.

• Gather improved turn pattern data.

Once an indisputable magnetic field map is available, it would be desirable for both academic and practical reasons to repeat both of the experiments described above to obtain a more precise dee voltage calibration. In the case of matching the

turn pattern, two ambiguities remain. One is the choice of whether to associate the first data point with the fourth calculated turn (which is short of the data) or fifth turn (which fell beyond the data.) The ambiguity could be removed if a beam probe were available which could reach into the first turn. Since the existing radial probe has interchangeable heads, this would be only a minor (and if need be, temporary) modification, and one single low radius probe head could be used to study all future copies of the C235.

6.8 Summary

We have modified the measured magnetic field map and produced an electric field map of the central region based on the original design of the C235 and all changes that had been made as of May, 1997. We have performed orbit tracking calculations which indicate good axial and radial focusing properties of the cyclotron, and we have obtained good agreement between computed and measured orbit positions. We have also used orbit computations to aid in the calibration of the cyclotron dee voltage. A modification to the ion source chimney has been tested both experimentally and in orbit simulations and was found to increase the beam current density by a large factor. (After completion of this study important modifications have been made to the cyclotron magnet to improve the isochronism of the magnetic field; to better understand the performance of the modified C235 cyclotron, the calculations presented herein should be repeated when new magnetic field maps are available.)

Bibliography

[1] H.G. Blosser, *et al.*, Advances in superconducting cyclotrons at MSU. In *Proc. of the 11th Intl. Cyclotron Conf.*, pages 157-167, Ionics, Tokyo, (1986).

[2] H. Blosser *et al.*, Compact Superconducting Cyclotron for Neutron Therapy, IEEE Transactions on Nuclear Science, NS-32, No. 5 3287 (1985).

[3] D. May *et al.* Proc. of the 12th Int. Conf. on Cyclotrons, Berlin, 1 (1989).

[4] W. Beeckman, Y.Jongen,A. Laisne, and G. Lannoye, Preliminary design of a reduced cost proton therapy facility using a compact, high field isochronous cyclotron, NIM B56/57 1201-1204 (1991).

[5] W.B. Mann, *The Cyclotron*, John Wiley and Sons, Inc. 1953.

[6] H.A. Bethe and M.E. Rose, The maximum energy obtainable from the cyclotron, Physical Review, 52, 1254 (1937).

[7] L.H. Thomas, The paths of ions in the cyclotron, Physical Review, 54, 580 (1938).

[8] J. R. Richardson, A Short Anecdotal History of the Cyclotron, Proceedings of the Tenth International Conference on Cyclotrons and their Applications, East Lansing, 617 (1984).

[9] M.M. Gordon, Effects of Spiral Electric Gaps in Superconducting Cyclotrons, Nuclear Instruments and Methods 169, 327-336 (1980).

[10] W.I.B. Smith, Nucl. Instr. and Methods **9**(1960) 49.

[11] G.H. Mackenzie, P.W. Schmor, and H.R. Schneider, Cyclotrons, Encyclopedia of Applied Physics, 4, 427 (1992).

[12] J.J. Livingood, *Principles of cyclic particle acceleration*, Van Nostrand, New York, (1961).

[13] H. Wollnik, *Optics of charged particles*, Academic Press, Inc. San Diego, (1987).

[14] R.E. Pollock *et al.*, Performance and characteristics of the IUCF injector cylcotron, IEEE Trans. on Nucl. Sci., NS-22, no 3, 1049 (1975).

[15] H.G. Blosser and D.A. Johnson, Focusing properties for superconducting cyclotron magnets. NIM, 121, 301-306 (1974).

[16] MSU NSCL Accelerator Group, Z3CYCLONE, Instruction Manual, (1992).

[17] H.G. Blosser, Superconducting Cyclotrons for Neutron Therapy, MSUCP-52 (1988).

[18] H. Blosser, J. Vincent and R. Maughan, Performance of the Harper Hospital cyclotron; effect of pulsed radio Frequency, Proc. 13th Int'l Conf. on Cyclotrons and Applications.

[19] I.G. Brown (Ed.), *The Physics and Technology of Ion Sources*, Wiley, New York, (1989).

[20] J. Koch (Ed.), *Electromagnetic Isotope Separators and Applications of Electromagnetically Enriched Isotopes*, Interscience Publishers Inc., New York, (1958).

[21] M. Mallory, PhD thesis, MSU (1966).

[22] M. Mallory and H. Blosser, Phase space density studies on cyclotron ion sources, IEEE NS-13, No. 4, 163 (1966).

[23] W.I.B. Smith, Beam defining slits and focusing grids near the ion source, *Sector Focused Cyclotrons* NAS-NRC publication 656, 183 (1959).

[24] A.H.Morton and W.I.B. Smith, NIM 4, 36 (1959).

[25] S. Snyder and F. Marti, Central region design studies for a proposed 250 MeV proton cyclotron, NIM A355, 618 (1995).

[26] C.J. Kost and F.W. Jones, RELAX3D Users's Guide and Reference Manual, TRIUMF, (1992).

[27] J. Bailey, F. Marti, and H.G. Blosser, Central Region Studies for the Harper Hospital Cyclotron, NSCL Annual Report, 170 (1989).

[28] H. Blosser, Problems and performance in the cyclotron central region, IEEE trans. nucl. sci. NS-13 No.4 1 (1966).

[29] H.B. White, *Cyclotron Ion Starting Times in the Second Harmonic Accelerating Mode*, MS thesis, MSU (1974).

[30] P. Miller and E. Kashy, Absolute calibration of the dee voltage by X-ray endpoint, Proc 7th Int. Conf. on Cyclotrons and their Applications, 171 (1975).

[31] Numerical values for rigidity are from the "Data Sheets" given in Proceedings of the Thirteenth International Conference on Cyclotrons and Their Applications, Vancouver (1992).

[32] P.J. Nolan, F.A. Beck, and D.B. Fossan, Large Arrays of Escape-Suppressed Gamma-ray Detectors, Annu. Rev. Nucl. Part. Sci., 45:561-607 (1994).

[33] J.W. Kim, 8 Tesla Superconducting Magnet for Cyclotron Studies. PhD thesis, Michigan State University, 1994.

[34] M.T. Menzel and H.K. Stokes, Users's Guide for the POISSON/SUPERFISH Group of Codes, LA-UR-87-115, January (1987).

[35] M. Reiser, NIM 18-19, 370, (1962).

[36] H.G. Blosser *et al.*, IEEE Trans. Magn., 25,no 2, 1746 (1989).

[37] F. Marti and A. Gavalya, Proc. of the 11th Int. Conf. on Cyclotrons, Tokyo, 1986.

[38] J.L. Belmont and J.L. Pabot, IEEE Trans. Nucl. Sc., NS-13:191-193, (1966).

[39] D. Johnson and F. Marti, NSCL Annual Report, 125, (1989)

[40] H.G. Blosser, *et al.*, Resonant extraction from three-sector low-spiral cyclotrons, Nucl. Inst. Meth. 18/19, 488, (1962).

[41] C.B. Bigham, NIM 131, 223, (1975).

[42] T. Antaya *et al.*, NSCL Annual Report, 198, (1980-1981).

[43] A.E. Litherland, Ultrasensitive mass spectrometry with accelerators, Ann. Rev. Nucl. Part. Sci. 30, 437(1980).

[44] J.C. Davis, AMS beyond 2000, NIM B92, 1(1994).

[45] D.J. Clark, Cyclotrons as mass spectrometers, 10th Intl. Conf. on Cyclotrons and their Applications, 534, East Lansing (1984).

[46] D.J. Clark *et al.*, A compact permanent magnet cyclotron for accelerator mass spectrometry, Proc. of the 14th Int'l Conf on Cyclotrons and their Applications, Capetown, South africa, 111, (1995).

[47] A.T. Young *et al.*, Development of a compact permanent magnet cyclotron for accelerator mass spectrometry, Proc of the 1993 Particle Accelerator Conference, 1727, (1993).

[48] C.Y. Li, *et al.*, A permanent magnet system for a cyclotron used as a mass spectrometer, Proc of the 13th Int'l Conf on Cyclotrons and their Applications, Vancouver, Canada, 561 (1992).

[49] K.J. Bertsche, *A Small Low Energy Cyclotron for Radioisotope Measurements*, PhD thesis, University of California, Berkeley (1989).

[50] Y. Jongen, European Cyclotron Conference, Groningen, unpublished. (1983).

[51] K. Bertsch *et al.*, Radiocarbon detection with a small low energy cyclotron, NIM A301, 358 (1991).

[52] A.T. Young *et al.*, Design of a compact permanent magnet cyclotron mass spectrometer for the detection and measurement of trace isotopes, Proc. 13th Int'l Conf. on Cyclotrons and their Applications, Vancouver, Canada, 705 (1992).

[53] M.B. Chen *et al.*, The successful SINR mini cyclotron AMS for ^{14}C dating. NIM B92, 213 (1994).

[54] M.B Chen *et al.* A new type of minicyclotron as accelerator mass spectrometer. Proc. of the 14th Int. Conf. on Cyclotrons, Cape Town, South Africa, 107 (1995).

[55] P.G. Friedman *et al.*, Low background-rate detector for 40-keV ions using a conversion dynode and a microchannel-plate electron multiplier to reject low-energy ions, electrons and photons. RSI 59,98(1988).

[56] M.B. Chen *et al.*, Adopting a non-sinusoidal wave dee voltage in minicyclotrons as mass spectrometers for dating, NIM A278, 409(1989).

[57] K. Bertsch *et al.*, Detection of radiocarbon in the cyclotrino, MIM B52, 398 (1990).

[58] D. Johnson, T. Kuo and F. Marti, Calculation of 3D Magnetic Fields with ANSYS, a Finite Element Commercial Code, Proceedings of the European Particle Accelerator Conference, Berlin 1992.

[59] K.J. Bertsche, Ion motion in a small low energy cyclotron, NIM A301 171-181 (1991).

[60] K. Purser, Private communication.

[61] M.B. Chen *et al.*, Determination of the shape of the dee electrodes in the SINR minicyclotron used as AMS for ^{14}C dating, NIM A297, 47-59 (1990).

[62] W. Joho, Application of the phase compression – phase expansion effect for isochronous storage rings, Particle Accelerators, 6,41-52, (1974).

[63] F.J. Lynch *et al.*, Beam buncher for heavy ions, NIM 159, 245-263 (1979).

[64] Ion Beam Applications s.a., Chemin du Cyclotron 2, 1348 Louvain-la-Neuve, Belgium.

[65] Proposal for an IBA-NSCL Collaboration.

[66] During the course of this study, the Boston team performed a series of Smith-Garren style experiments to measure the phase of the actual beam. Results of these experiments disagree with the results of orbit calculations in the fieldmap used herein. This development calls into question the accuracy of the magnetic field used for this study. The studies described here should therefore be repeated when new field measurements are available.

[67] S. Snyder, *Study and Redesign of the NSCL K500 Injection, Central Region, and Phase Selection Systems*, PhD thesis, MSU (1995).

[68] Y. Jongen, private communication.